2012

NOVEL SOFT SURFACES WITH INTERESTING SURFACE AND BULK MORPHOLOGY

Souvik Chakrabarty
Virginia Commonwealth University

NOVEL SOFT SURFACES WITH INTERESTING SURFACE AND BULK MORPHOLOGY.

A dissertation submitted in partial fulfillment of the requirements for the degree of Doctor of Philosophy at Virginia Commonwealth University.

by

Souvik Chakrabarty

B.S. (2007), Jadavpur University, India.

Director: Dr. Kenneth J. Wynne

Professor, Department of Chemical and Life Science Engineering

Virginia Commonwealth University

Richmond, Virginia

June 2012

ACKNOWLEDGEMENT

The author wishes to thank some of the many people whose support and assistance has made this degree possible. Firstly, I would like to express my gratitude and thanks to my Ph.D. mentor, Prof. Kenneth J. Wynne for providing immense support, guidance and enthusiasm throughout the years of my graduate life. It is his constant encouragement that helped me persevere through some of the doldrums of my Ph.D. I would like to thank all members of the Wynne group, Ohman group, Yadavalli group and the Rao group, past and present, for helping me in my endeavor. I would like to thank my committee members for their time and valuable suggestions. I would also like to acknowledge the National Science Foundation (NSF) and the Virginia Commonwealth University for providing financial support for these projects.

I would like to thank my parents for being a constant source of support and encouragement, guiding me through every phase of my life. I would like to thank my grandparents (dinna, borda and mesda) from the bottom of my heart for their unconditional love and support. Finally, I would like to dedicate my thesis to my grandma, dinna, who has taught me the way of life.

TABLE OF CONTENTS

SCHEMES

LIST OF FIGURES

LIST OF TABLES

ABSTRACT

NOVEL SOFT SURFACES WITH INTERESTING SURFACE AND BULK MORPHOLOGY.

By Souvik Chakrabarty

A dissertation submitted in partial fulfillment of the requirement for the degree of Doctor of Philosophy at Virginia Commonwealth University

Major Director: Dr. Kenneth J. Wynne, Professor, Department of Chemical and Life Science Engineering

The goal of this research is to cover a broad set of scientific investigations of elastomeric materials based on polydimethylsiloxane (PDMS) and poly((3,3,3-trifluoroethoxymethyl)methyloxetane), 3F diol. The structures of these polymers are shown as **1** and **2**, respectively. The scope of study covers five areas, well correlated with each other. The first study investigates the near surface morphology of condensation cured PDMS as a function of increasing the amount of siliceous phase. The appearance, disappearance and reappearance of untreated fumed silica nanoparticles at the PDMS near surface and their correlation with the volume fraction of siliceous phase have been studied. This research with PDMS nanocomposites has led to the development of an alternative route for improving mechanical strength of PDMS elastomers, conventionally known to have weak mechanical properties. The second study involves synthesis of a triblock copolymer comprising of four mutually immiscible

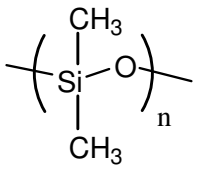

1

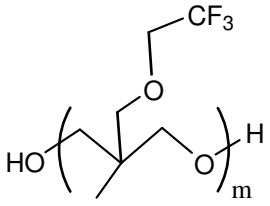

2

phases, namely, soft segments comprising of fluorous and silicone domains, a diisocyanate hard segment and a glassy siliceous phase. Structure-property relationship has been established with an investigation of the interesting surface and bulk morphology. The highly improved mechanical strength of these *soft materials* is noteworthy. The dominance of silicone soft block at the triblock near surface has led to the third study which investigates their potential non-adhesive or abhesive characteristic in both a laboratory scale and in a marine environment. The peak removal stress and the removal energy associated with the detachment of a rigid object from the surface of these triblock copolymers have been measured. Results obtained from laboratory scale experiments have been verified by static immersion tests performed in the marine environment, involving the removal of adhered soft and hard fouling organisms. Gaining insights on the characteristics of an *easy release* surface, namely low surface energy and a low near surface modulus, a new way for controlling the near surface composition for elastomeric coatings have been developed. This technique involves an elastomer end-capped with a siliceous crosslinking agent and a tough, linear polyurethane. The basic concept behind the hybrid compositions is to develop a coating suitable for foul release applications, having a low energy surface, low surface modulus but good bulk mechanical strength. Henceforth, the fourth study deals with synthesis and characterization of the hybrid polymers over a wide range of composition and investigates their foul release characteristic in laborartory scale experiments. In our final study, attempts have been made in generating a silicone coating with antimicrobial property. A quaternary alkylammonium in different weight percents have been incorporated into a conventional, condensation cured polydimethylsiloxane (PDMS) elastomer. Antimicrobial assay has been performed on these modified silicone coatings to assess their biocidal activity against strains of *Escherichia coli*, *Staphylococcus aureus* and *Pseudomonas aeruginosa.*

Surface accessibility of quaternary charges has been quantified by measuring the streaming potential of a modified coating. An effort has been made in improving the mechanical strength of the weak PDMS elastomers by adding treated fumed silica nanoparticles as reinforcements. The effect of adding fillers on the mechanical property (tensile), surface concentration of quaternary charge and on the biocidal activity of a representative sample has been investigated.

CHAPTER 1

General Introduction: Novel Polymer Compositions with Interesting Surface and Bulk Morphology.

1.1. Introduction

Surface modification of polymers is a technique where properties of the '*nanoscale*' surface / '*mesoscale*' near surface are tailored to achieve the desired functionality while still retaining the macroscale bulk characteristic. The first step towards such a design is to identify a polymer with bulk property matching with the requirements of the end application. Material properties include elasticity, strength, degradability and optical clarity. The second step involves optimizing surface functionalization by introducing the desired type and quantity of functional groups. Incorporation of the surface functionalizing moiety can be achieved by either physical blending or chemical reaction with the base polymer.

The areas of research that are investigated in this dissertation involve surface modification of commodity polymers for both academic and practical applications. In a broader perspective, the basic thrust of the research projects elucidated here is in tuning the surface properties of polymers to provide a biological interface for interactions with both microscale and macroscale organisms, namely, bacteria and marine species. The bulk polymers used for the present studies include polydimethylsiloxane and polyurethanes, a brief discussion of which is given in the subsequent sections.

1.1.1. Polydimethylsiloxane (PDMS). Commonly referred to as silicones, they belong to a group of polymeric organosilicon compounds. PDMS is the most widely used silicon based organic

polymer, well known for its rheological property. PDMS is synthesized by polymerization of dimethyldichlorosilane in the presence of water molecules as shown in Eq. 1.1.

$$n\mathrm{Si(CH_3)_2Cl_2} + n\mathrm{H_2O} \longrightarrow \mathrm{Si[(CH_3)_2O]_n} + n\mathrm{HCl} \qquad \text{Eq. 1.1}$$

Polydimethylsiloxanes can be produces in multiple viscosities, ranging from a thin liquid to a thick rubbery semisolid polymer. Some of the chemical properties of PDMS include low thermal and chemical reactivity, low toxicity, hydrophobicity and thermal stability. Due to the above properties, PDMS finds widespread application as lubricants, sealants, adhesives, insulation and also as medical implants and devices.

This study involves the use of two different types of silicones, namely, a silanol terminated PDMS (90 cSt and 1000 cSt) and an aminopropyl terminated PDMS.

1.1.2. Oxetane monomers and Polyoxetanes. Oxetanes, also known as 1,3-propylene oxide is a heterocyclic organic compound having a four membered ring. 3-bromomethyl-3-methyl oxetane (BrOx) is the common starting material for a majority of the oxetane monomers. BrOx is synthesized from 1,1,1-tris(hydroxymethyl) ethane by undergoing a bromination followed by subsequent treatment with NaOH to yield the product as shown in Eq. 1.2 and 1.3. BrOx is then reacted with the respective alcohol by Williamson synthesis to produce the desired oxetane monomer (Eq. 1.4); R stands for a semifluorinated moiety.

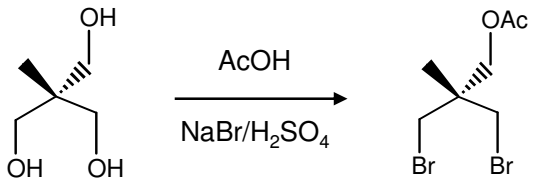

Eq. 1.2

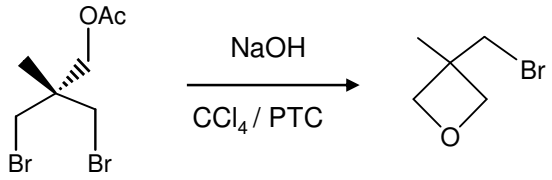

Eq. 1.3

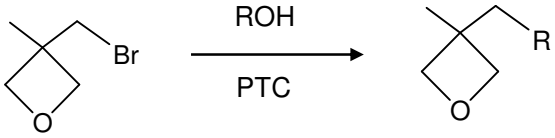

Eq. 1.4

In this study 3-(2,2,2-trifluoroethoxymethyl)-3-methyloxetane also known as 3FOx, is the monomer that undergoes a cationic ring opening polymerization to produce the polyoxetane, P(3FOx) shown in Eq. 1.5.

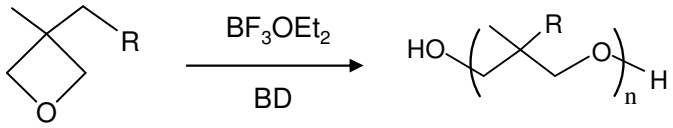

Eq. 1.5

Since, the reaction entails chain termination by incorporating hydroxyl moieties at the chain ends, the P(3FOx) polyoxetane has been referred to as 3F diol in this study.

1.1.3. Polyurethanes. These are polymer chains formed by polyaddition reaction between a polyisocyanate and a polyol in the presence of catalyst and other additives leading to formation

of urethane linkages. Polyurethanes comprise of a hard and a soft segment, interactions among which leads to interesting surface and bulk morphology. Based on the chain extender, whether it is a diol or a diamine, the resulting polymer can be a polyurethane or polyurethane-urea. A significant amount of hydrogen bonding between the urethane and urea moieties leads to close packing of hard segment domains that imparts excellent mechanical properties to these polymers. Polyurethanes can be thermoplastics or thermosets, depending on the nature of chain interactions.

In a typical polyurethane synthesis, a diol monomer is end-capped with a diisocyanate as shown in Scheme 1.1 to produce the polyurethane prepolymer. The prepolymer chains are reacted with a diol / diamine chain extender (Scheme 1.1) to form long chain polyurethanes of the desired molecular weight.

The scope of study in this research revolves around the use of two specialty polyurethanes, one having a fluorous polyoxetane as the soft segment and the other being a triblock urethane-urea crosslinked to form a thermosetting elastomer. A detailed synthetic procedure for these polyurethanes has been elucidated in succeeding chapters.

1.2. Scope of study.

1.2.1. PDMS Nanocomposites. A processing method using high speed mixing was developed for the generation of nanocomposites comprised of α, ω-dihydroxy-polydimethylsiloxane (PDMS) and untreated fumed silica nanoparticles (U-FSN). Conventional condensation cure with poly(diethoxysiloxane) (PDES) was employed to generate PDMS / FSN nanocomposites with increasing weight fractions of the siliceous domain.

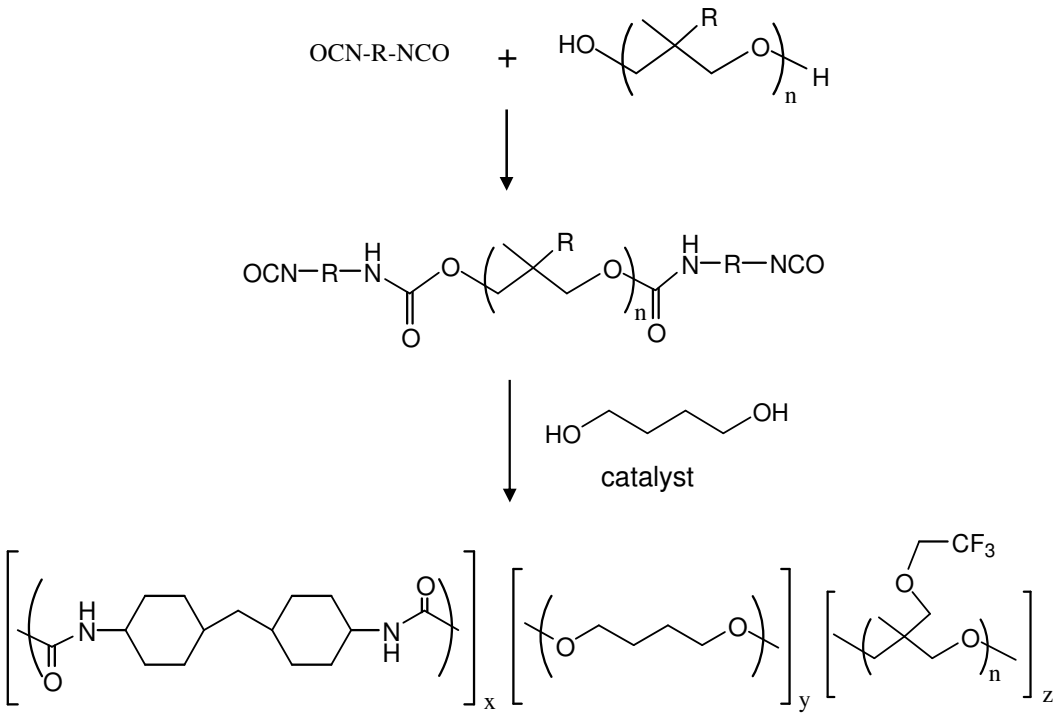

Scheme 1.1. Polyurethane synthesis using a diol chain extender.

This study focused on the changes in surface morphology imaged by non-contact or tapping mode atomic force microscopy (TM-AFM) as a function of increasing the initial concentration of PDES. The ratios (X) of Si-OEt from PDES to Si-OH from PDMS end groups were 4X, 14X, 28X, 35X, 45X and 60X. Compared to prior work, two important differences in the present investigation were (1) the use of a high shear mixer as a processing tool to facilitate nanoparticle dispersion and (2) spin coating instead of dip coating. Common to the present and prior work was the use of TM-AFM for investigating surface morphology as a function of siliceous phase precursor concentration. TM-AFM phase images showed that nanoparticles were "reporters" and reflect effects of composition and processing on surface morphology. Near-surface nanoparticles were clearly imaged up to 35X, "disappear" at 45X, then "reappear" at 60X. These results were different from those previously reported where "disappearance" was noted for 14X compositions. The differing results revealed that processing conditions have an important effect on surface morphology.

1.2.2. Reactive triblock copolymer. Fluorocarbon and polydimethylsiloxane (PDMS) polymers have been the subject of much investigation and study over the past few decades. Immiscibility of fluorocarbon and PDMS polymers is well known and studies have shown fluorous groups to either concentrate at the surface or aggregate into self associated assemblies in order to lower the free energy of the system. This study focuses on the synthesis of a novel block copolymer system comprising of four mutually immiscible domains, namely, a fluorinated polymer, a silicone soft segment, a diisocyanate hard segment and a siliceous domain. These domains were connected to each other by urea and urethane linkages. Four different triblock compositions were synthesized by altering the length of the fluorous polymer chain and by increasing the weight fraction of the glassy siliceous domain. These triblock copolymers showed very interesting surface and bulk

morphologies, which were correlated with TM-AFM, XPS and DMA (tensile and modulus testing). The triblock copolymers demonstrated remarkable mechanical property, attributed to a combined effect of urea/urethane H-bonding, bulk phase separation and the presence of a small fraction of hard block component. An interesting structural, compositional and morphological relationship was observed in this study.

1.2.3. Fouling release triblock copolymers. XPS studies on the triblock copolymers revealed a predominance of silicon soft segment at the near surface of a coated substrate, which reduces the surface free energy. Recent studies have shown that due to low surface energy, silicones provide a weakly adherent substrate for attachment of marine fouling organisms. A recent cause of concern in the marine environment has been fouling of ship hulls, leading to an increased surface roughness and hydrodynamic drag. The present study focuses on assessing the easy release characteristic of the triblock copolymers, described in the previous chapter. Laboratory scale tests were devised to mimic the attachment and subsequent removal of adhered organisms in the marine environment. The force required to detach an aluminum cylinder attached to the coated substrate was measured as the peak removal stress and the corresponding energy required involved in detachment was termed as the removal energy. A typical triblock composition was also tested for settlement and removal of soft and hard fouling organisms. In-field static immersion tests showed that the surface of the triblock coatings could be easily cleaned of both soft and hard settlements. Thus, the new triblock compositions demonstrated immense potential for use as non-toxic, foul release coatings.

1.2.4. Flexible Bottle brush-nanoglass (BB-NG) hybrid polyurethanes. Results from the triblock copolymer compositions led into investigation of the bulk and near-surface properties of a stratified hybrid composition, the architecture of which has been designated as a ‘flexible bottle

brush-nanoglass'. The designation corresponds to two principle components: (a) a soft, amorphous polyoxetane 'bottle brush' with reactive triethoxysilyl end groups and (b) an alkoxysilane that together with bottle brush chain ends comprise precursors to a "nanoglass" phase via hydrolysis and condensation reactions. In this study, the BB-NG system was used for surface modification of a specialty polyurethane, HMDI/BD(30)-(3F-4.5). Interestingly, the BB-NG phase forms a low modulus layer at the surface while the polyurethane is concentrated in the bulk effecting improved mechanical property. The surface morphology of these hybrid compositions was dependant on the weight percent of the BB-NG phase, with a higher weight percent of the BB-NG phase contributing to a low modulus surface. Due to the low surface energy and near surface modulus, the BB-NG modified compositions offer promise as foul and ice release coatings.

1.2.5. Antimicrobial silicones. This study focused on functionalizing polydimethylsiloxane surfaces with cationic charge bearing quaternary ammonium salts. The study involved synthesizing a surface modifying additive, which when added in minute weight percents to PDMS, would render biocidal activity to the surface. The surface modifying additive was synthesized by following a substitution reaction between 3-chloropropylmethyl dimethoxysilane and N,N – dodecyldimethylamine. Varying weight percentages, namely, 0.5%, 1% and 2% of the modifier were added to silanol terminated PDMS followed by condensation cure to obtain the elastomeric network. Microscope slides coated with the quaternary charge bearing PDMS were tested for biocidal activity against bacterial strains of *Escherichia coli*, *Staphylococcus aureus* and *Pseudomonas aeruginosa*. Preliminary tests have suggested that 1% (by weight) of the modifier when added to PDMS produces optimum biocidal activity. A kill kinetic study was performed on the 1 wt% modified PDMS coating (t = 15, 30 and 45 min) for different time

intervals. An effort was made at improving the mechanical property of the coatings by incorporating 10 wt% treated fumed silica nanoparticles by still retaining their biocidal effectiveness. The reinforced samples showed an increase in their mechanical strength with an allowable strain at break of ~250% as compared to 45% (unfilled sample) but a diminution in biocidal activity was observed. A model has been proposed correlating the compositional paradigm to the observed results.

CHAPTER 2

Processing dependence of surface morphology in condensation cured polydimethylsiloxane nanocomposites.

2.1. Introduction

Research in hybrid nanocomposites seeks optimization of performance by combining synergistically organic and inorganic materials.[1-9] Nanoparticle interfacial modification is an essential part of engineering optimal compositions. This is demonstrated by the discovery of dramatic improvements in mechanical properties for clay polymer nanocomposites,[10] which resulted in a new materials research field that is still of great interest.[11,12] Expanding studies in nanocomposites seek to improve performance in diverse areas such as dielectrics[13] and hybrid photovoltaics.[14]

Silicone elastomers have weak mechanical properties[15-17] and require fillers to provide reinforcement.[18] As a result, one of the most common hybrid nanocomposites, which has been known for decades[19] is comprised of a polydimethylsiloxane matrix combined with fumed silica nanoparticles (FSN).[20-23] In addition to fumed silica nanoparticles, zeolite,[24] ceramic,[25] and silica nanoparticles[26,27] have been utilized.

Polydimethylsiloxane elastomers have very low glass transition temperatures (T_g ~ -120 ºC) and high thermal stability (~ 250 ºC).[28] Hydrophobicity, easy fabrication and biocompatibility[29,30], have led to a wide range of applications including caulks, adhesives and coatings,[31] biomaterials,[32] and even in tissue engineering.[33]

Past studies have explored the surface science associated with several sol-gel cured PDMS systems. To improve oleophobicity, hydroxyl terminated polydimethysiloxane, $PDMS(OH)_2$, was crosslinked with (tridecafluoro-1,1,2, 2-tetrahydrooctyl)triethoxysilane (FTEOS). The surface morphology depended strongly on the PDMS / crosslinker ratio.[34] For example, at a ratio of 6X (X = SiOEt / SiOH), micron scale, fluorous siliceous domains were observed surrounded by siloxane rich domains.[34] In contrast, at a ratio of 12X, a uniform surface layer of the fluorous siliceous phase was formed, which was confirmed by XPS and high advancing contact angles. Although the goal of oleophobicity was attained, the fluorous siliceous domain is brittle, limiting applications.[35]

PDES is poly(diethoxysiloxane), with the approximate empirical formula $[SiO(CH_3CH_2O)_2]_n$ or $[SiO(OEt)_2]_n$. While tetraethylorthosilicate (TEOS) volatilizes during hydrolysis and condensation cure of $PDMS(OH)_2$, low volatility and relatively low condensate (ethanol) generation makes PDES very useful alternative.[36,37] A time dependent surface morphology and stability was found for PDMS / PDES coatings.[34]

PDES and related condensation cure agents are typically used at ~5 wt% or less. Such low sol-gel curing agent content minimizes shrinkage and generation of volatiles from condensation cure. To explore the impact of increasing siliceous domain content, the surface and bulk morphology of elastomeric coatings comprised of $PDMS(OH)_2$, fumed silica nanoparticles and increasing PDES content (Scheme 2.1) was investigated by tapping mode atomic force microscopy (TM-AFM).[38,39] It is important to note that mixing was performed manually at ambient temperature; herein, this process is designated very low speed (VLS) mixing. For U-FSN (14 wt%) and complete cure at 100 °C, the bulk nanoparticle / PDMS matrix morphology was conventional. Unexpectedly, near-surface nanoparticles acted as morphological “reporters”,

revealing a surface morphology dependent on the mole ratio of OEt_{PDES} / OH_{PDMS} designated by "X": (1) 5X, nanoparticles imaged, "expected"; (2) 14X, nanoparticles "disappear"; (3) 28X, nanoparticles "reappear".

Water is both a reactant (-Si-O-Et hydrolysis) and product (Si-OH condensation) in alkoxysiloxane cure using $[SiO(OEt)_2]_n$. Therefore, in addition to crosslinking $PDMS(OH)_2$, a glassy siliceous domain is formed. The "appearing" and "disappearing" nanoparticle phenomenon noted above was explained by a model that related the AFM tip interaction with the increasing near-surface siliceous domain content and nanoparticle surface chemistry. With very low speed (VLS) processing conditions used previously, increasing PDES content to 14X resulted in a near-surface siliceous layer that isolated the AFM tip from near-surface untreated fumed silica nanoparticles (U-FSN, disappearing, figure 2.7B). Increasing the siliceous content further (28X) resulted in a near-surface siliceous volume fraction high enough to encompass the near-surface nanoparticles and facilitate mechanical detection by the tip (reappearing). The analogy that was employed to explain this unexpected phenomenon was as follows: when blindfolded, it is easy to detect a slightly submerged rock under water; however, it is not possible to detect the rock if a thin layer of ice intervenes. If the ice becomes thick enough to contact the rock, it is possible to locate the rock due to a lower sound when tapping.

VLS mixing employed in the above study is tedious and the extent of nanoparticle dispersion is "operator dependent". On a large scale, mixing viscous silicone macromonomers with fillers is done via extruders or other mechanical devices so as to obtain uniform filler dispersion. To mimic such processes a small scale device for high speed (HS) mechanical mixing was used for the nanocomposite processing reported herein. Processing the same PDMS nanocomposite compositions via HS mixing provides near-surface morphologies that are

surprisingly different compared to VLS mixing. While the same morphological sequence (appearing, disappearing, reappearing) is "reported" by near-surface nanoparticles, different compositions for these events are observed and the changes imaged by TM-AFM are more subtle. In view of the importance of understanding nanocomposite morphology and nanoparticle interfaces and their relationships to the synergistic development of hybrid materials properties, these results are presented herein.

2.2. Materials

Silanol terminated polydimethylsiloxane (DMS-S31, 1000 cSt, 26 kDa) was obtained from Gelest Inc. Unmodified fumed silica nanoparticles (U-FSN, Aerosil 300 fumed silica unmodified) having a diameter of 50 nm and a surface area of 300 ±30 sqm/g was obtained from Aerosil. Modified fumed silica nanoparticles (T-FSN, Cab-o-sil TS530 HMDZ treated fumed silica) having a BET surface area of 200 m^2/g was generously provided by Quantum Silicones, Midlothian, VA. Polydiethoxysiloxane (PDES) containing 40-42 % SiO_2 equivalent (ES40) was obtained from Gelest; dibutyltin dilaurate (DBTDA) was obtained from Aldrich.

2.3. FSN-PDMS nanocomposite preparation and processing.

Fumed silica / PDMS nanocomposite coatings were prepared in two steps. Initial nanoparticle dispersion was followed by further dispersion of the nanocomposites and catalyst / PDES mixing.

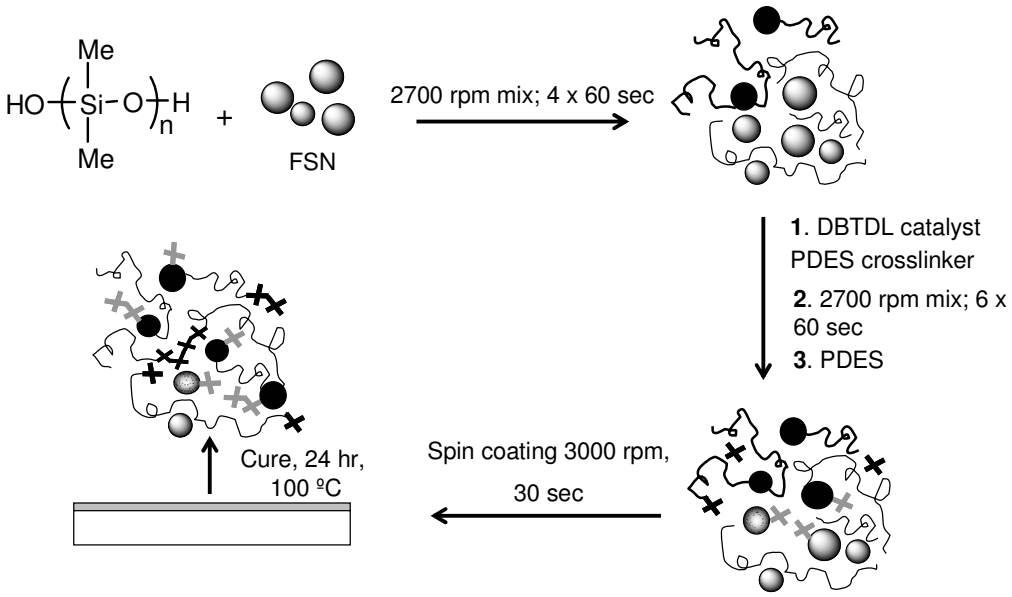

Scheme 2.1. Processing sequence for PDMS-FSN nanocomposites. The filled circles represent nanoparticles to which –SiOH chain ends are bound. A grey x indicates covalent bonding of $–Si(-O-)_3$ to FSN.

2.3.1. Nanoparticle dispersion. Hydroxy-terminated polydimethylsiloxane (5 g), unmodified fumed silica nanoparticles (U-FSN, 0.71 g, 14 wt%) were placed in a 50 g capacity Flacktek containers having a screw top. The container was placed in a Speed Mixer-DAC 150FV (Flacktek Inc., Landrum SC). The protocol entails the use of a 'High-Speed' (HS) mixing technique which involves mixing the ingredients in a cycle of 2700 rpm for 60 seconds. This HS mixing process was repeated 4 times to obtain a highly viscous, whitish nanoparticle / PDMS dispersion. The rotary motion and shear combined to increase the temperature of the nanoparticle / PDMS dispersion from ambient (25 °C) to 30 °C.

2.3.2. Catalyst / PDES mixing. The metric for defining quantities of PDES crosslinker / siliceous domain precursor is the ratio (X) of Si-O-Et groups from PDES to Si-OH groups [$PDMS(OH)_2$]. To explore a wide range of siliceous domain content, 4, 14, 28, 35, 45, and 60X compositions were obtained. Calculated amounts (Table 2.1) of PDES and 0.5 wt% DBTDA catalyst were added to the nanoparticle PDMS dispersion obtained as described above in step (a). The mixture was processed at 2700 rpm for 60 sec, which is the maximum processing time for the machine. After a 10 sec interval, this process was repeated 5 times to ensure homogeneity. The temperature of the resin mixture at this point was 40 °C. After a total of six mixing cycles the viscosity of the whitish resin was noticeably diminished by a combination of temperature and shear thinning. This decreased viscosity facilitated spin coating slides for surface analysis. Samples were spun coated on glass slides for 30 seconds at 3000 rpm, and cured for 72 hours at 100 °C. Previous work had established that these conditions would effect complete cure.[39] Although the nanoparticle / resin mixture was whitish-translucent, spin coating resulted in the formation of thin (ca. 30 μm), homogenous, optically transparent films.

2.3.3. Preparation of fracture surfaces. The processed PDMS resin containing U-FSN was poured into petri dishes and was allowed to cure for 72 hours at 100 °C. The resulting U-FSN/PDMS nanocomposite was dipped in liquid nitrogen and fractured to obtain a smooth surface.

2.4. Instrumentation / Characterization

2.4.1. AFM imaging. PDMS nanocomposite morphologies were investigated using TM-AFM instruments from Asylum Research, Santa Barbara, CA (MFP-3D) and Veeco Instruments, Plainview NY (DI-3100). For the MFP-3D, Olympus AC 240 TS cantilevers were used with a nominal spring constant in the range of 0.7 N/m-3.8 N/m. For the DI 3100 a Veeco Nanoscope V controller was utilized with Veeco RTESPW cantilevers (part: MPP-11100-W) having nominal spring constants in the range of 20 N/m-80 N/m. A scan rate of 1 Hz was used for all imaging. For comparisons, AFM images are normalized to the same phase scale (z, deg) as indicated in figure legends. The phase scale is chosen to optimize image quality and consistency with topographical images.

Phase images provide contrast between near-surface regions of higher and lower modulus.[40] With the nanoscope instrument, the default is light for regions of higher modulus and dark for softer regions. For example, an evolution of clearly defined surface domains was observed for condensation cured PDMS modified with a fluorous triethoxysilane.[41]

Similarly, for polyurethanes, near-surface hard block domains appear light while soft block domains are dark.[42-45] Inspection of images previously reported for PDMS nanocomposites[38,39] shows that near-surface nanoparticles appear dark while the “soft” silicone matrix is light. This representation is opposite to the earlier work noted above.[41]

Garcia first modeled a phase inversion phenomenon that recognized attractive and repulsive operational modes in TM-AFM.[46] In one mode, a net attractive force dominates the amplitude reduction while in the other a net repulsive force controls cantilever dynamics. Garcia's analysis showed that stiff samples give rise to large repulsive forces (a net positive force), while compliant materials give an opposite result. Changing the drive frequency, which controls tip-sample interactions can access both regimes so that the phase image representation for the same sample can be reversed.[46-48]

Garcia's analysis explains why the glassy, microscale surface features formed by the fluorous modifier were light/high modulus –dark/low modulus[41] while more compliant PDMS nanocomposites have reversed appearances. In the present paper, phase images are compared that often have opposite phase image representations for the same sample, but the underlying morphological structure is, of course, identical. The contrasting images are noted as "phase image reversal" or PIR in the appropriate points in the discussion.

2.4.2. Wetting Behavior. Static contact angles were obtained using a Rame-Hart goniometer equipped with an LCD camera. Deionized water (~18.2 MΩ) was used as the probe liquid. A water drop was placed on the coated surface and the image was taken immediately. Captured images were analyzed and contact angles were obtained using Dropview image software version 1.4.11. Average values were obtained for 10 observations (2 drop sites, 5 readings each).

Table 2.1. Composition of filled U-FSN nanocomposites.

PDES, g (mmoles OEt)[a] (wt%)	*Siliceous domain[c] (wt%)*	*Ratio "X"[b]*	*U-FSN, g (wt %)*	*Shrinkage (vol %)*
0.104 (0.77) (2.1)	0.87	4	0.72 (14.2)	1.03
0.363 (2.68) (7.3)	3.1	14	0.75 (14.5)	3.44
0.72 (5.33) (14.5)	6.1	28	0.8 (15)	6.51
0.91 (6.74) (18.2)	7.6	35	0.83 (15.4)	7.9
1.17 (8.67) (23.4)	9.7	45	0.87 (15.8)	9.7
1.56 (11.55) (31.2)	13	60	0.92 (16)	12.3

a. DBTDA catalyst (0.025 g) and mass of PDMS (5.0 g) were held constant.

b. X = Si(OEt) /Si(OH)

c. Calculated SiO_2 weight % (from PDES) in the nanocomposite.

2.5. Results

The combination of hydroxyl-terminated PDMS, untreated fumed silica nanoparticles (U-FSN) and increasing amounts of polydiethoxysiloxane (PDES), that is, increased siliceous domain content, led to the unexpected surface phenomenon of "appearing" and "disappearing" nanoparticles.[39] This was followed by "reappearing" nanoparticles at even higher PDES concentrations.[38] These results attest to the sensitivity of TM-AFM to subtle changes in nanoscale surface morphology for condensation cured PDMS. The work reported herein emerged from an effort to simplify and improve reproducibility of mixing viscous PDMS resin / nanoparticle combinations. Considering the straightforward formulation and nominally similar processing the TM-AFM results were surprising.

2.5.1. Compositions. Dihydroxy-terminated PDMS (26 kDa) and FSN (14 wt%) were used to generate a series of nanocomposites. By increasing the PDES crosslinker / siliceous phase precursor, compositions with increasing siliceous domain (SD) were prepared (Table 2.1). In an earlier investigation, a "Very Low-Speed" (VLS) mixing technique was employed involving mixing the ingredients in a cycle of 100 rpm for 60 seconds. In contrast to the earlier study, compositions were processed with a high speed (HS) mixing technique described earlier to obtain finely dispersed nanoparticles.

Scheme 2.1 illustrates the processing sequence, which is critical to the development of surface morphologies described in the next section. First, four HS mixing cycles accomplish initial homogenization. Second, PDES and catalyst are added followed by six HS mixing cycles. During this sequence a noticeable decrease in viscosity occurred, but the bulk resin mixture remained whitish-opaque. After spin coating and cure at 100 °C, optically transparent 30 µm films were obtained.

2.5.2. PDMS/U-FSN Surface Morphology. TM-AFM phase images (20 x 20 µm, Asylum MFP-3D) are shown in figure 2.1 for U-FSN nanocomposites with increasing siliceous content ("X") but similar U-FSN weight percents. As the weight fraction of siliceous content increases (4X to 28X) near surface nanoparticles are imaged with increasing clarity. At 35X nanoparticle imaging is subdued while nanoparticles "disappear" at 45X. At 60X, nanoparticles "reappear" at a modest resolution.

The results in figure 2.1 confirm previous results that U-FSN act as "reporters" for near-surface morphological changes.[38,39] However, the sequence of observed morphologies is completely different from those previously reported.[38,39] To confirm the unexpected results, a new set of samples were processed (Scheme 2.1) and imaged with a Veeco Nanoscope V system (Figure 2.1).

The sequence of phase images in figure 2.1 is essentially the same as those in figure S2.1, although the contrasting imaging colors are opposite due to phase image reversal (PIR) described in the experimental section. Thus, convinced that the nanoparticles are "reporting" an important effect for the new processing sequence, we set about interpreting the "message".

To focus more clearly on nanoscale surface morphology, figure 2.2 shows 2 x 2 µm phase images for the same composition range imaged in figure 2.1 at 20 x 20 µm. A parallel set of phase images (5 x 5 µm, Asylum MFP-3D, PIR contrast) is shown in figure S2.2. Considering the 14-16 wt% FSN nanoparticles, comparable near-surface morphologies might be expected but are not observed. From the phase images in figures 2.1, 2.2 and S2.1, and S2.2, a range of near-surface morphologies is observed with increasing siliceous domain content. When PDES content is low, the near-surface concentration of U-FSN appears low. The surface morphology for the 4X composition is dominated by the amorphous PDMS volume fraction. Near-surface U-FSN is

imaged as light features. With increased weight fraction of siliceous domain from 4X to 28X, the apparent concentration of near-surface nanoparticles increases. These higher resolution images confirm that increasing the siliceous phase content to 35X results in an apparent diminution of near-surface nanoparticle concentration. At 45X near-surface nanoparticles are not imaged or "disappear".

At 60X, the near-surface nanoparticles "reappear" with larger apparent size, moderate contrast, and high near-surface concentration. An enlarged phase image (20 x 20 μm) for U-FSN-60X is shown in figure S2.3. The high density of near-surface nanoparticles and more clearly defined appearance are noteworthy.

2.5.3. PDMS/U-FSN Surface Topology. AFM height images (2D, 3D, 20 x 20 μm) for U-FSN nanocomposites are shown in figure 2.3. The RMS roughness, R_q, is shown as a function of composition in figure 2.4. RMS roughness increases from 28 nm to a maximum of 62 nm at 28X followed by a steep decline to 8 nm at 45X; a slight increase to 13 nm is found for 60X. As is usually found, RMS roughness depends on the scan size. The noteworthy coincidence of the minimum in R_q and the "disappearance" of near-surface U-FSN (Figures 2.1, 2.2, S2.1, S2.2) was an important consideration in the development of the proposed model for near-surface morphology.

2.5.4. PDMS/T-FSN Surface Morphology and Topology. Coatings were prepared by the process described in Scheme 2.1 using *trimethylsilylated* fumed silica nanoparticles (T-FSN). Figure S2.5 shows TM-AFM 2D height, phase and 3D height images (20 x 20 μm) for 4-, 28- and 60X T-FSN nanocomposites; from figure S2.5, R_q is 7.5, 7.1, and 7.7 nm, respectively. In the case of T-FSN, the near-surface morphology and topology for the processing method described in Scheme 2.1 is identical to that observed previously for hand mixing.

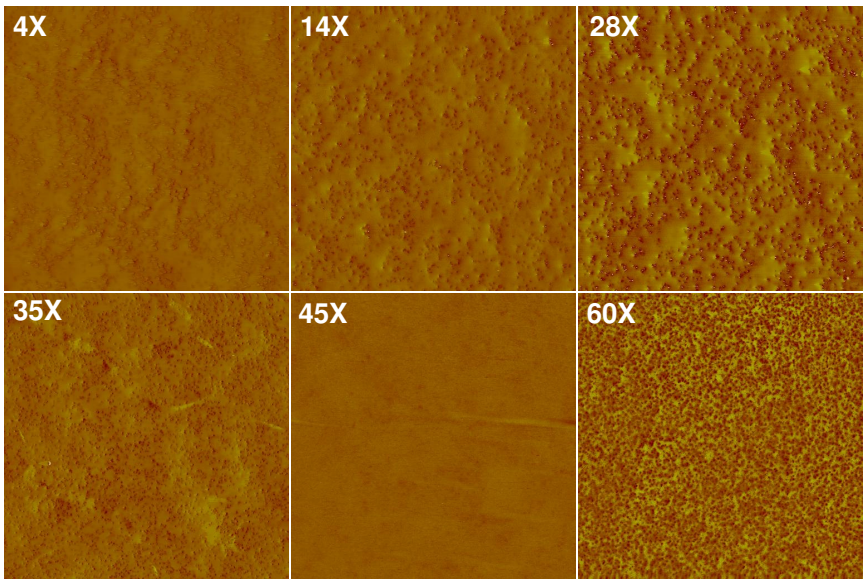

Figure 2.1. 20 x 20 µm Phase images (r_{sp} = 0.8, z = 40°) for U-FSN-PDMS samples cured at 100°C for 72 hours (VEECO Nanoscope V).

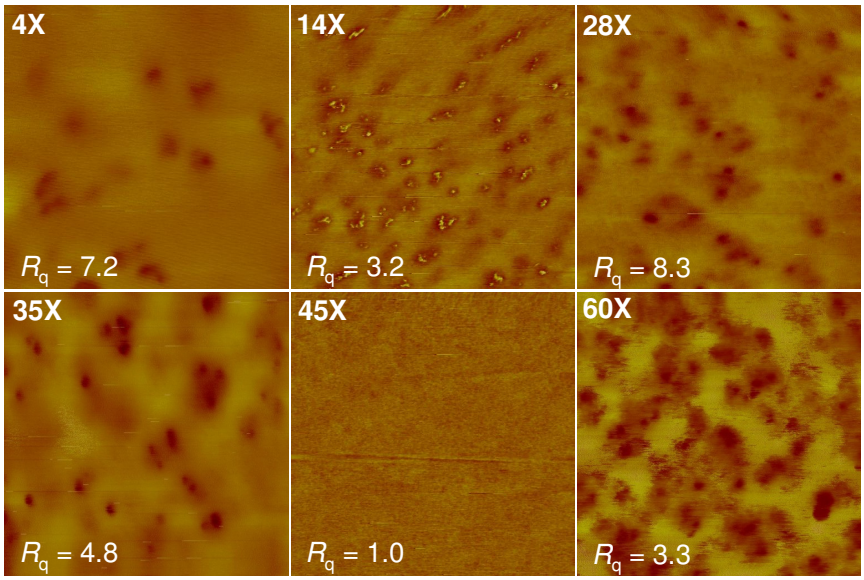

Figure 2.2. 2 x 2 µm Phase images (r_{sp} = 0.8, z = 40°) for U-FSN nanocomposites. *R*q values are in nm.

That is, the images are virtually devoid of near-surface features, nanoparticles are not detected / imaged or appear very faintly, and surfaces have very low RMS roughness. Thus, the processing dependence of morphology and topology for U-FSN nanocomposites on the siliceous domain content must stem from chemical interactions of PDMS, PDES, and U-FSN.

2.5.5. PDMS/FSN Fracture Surface Morphology and Topology. TM-AFM images for all U-FSN fracture surfaces are shown in figures 2.6 and S2.7. Height (2D, 3D) and phase images have a similar appearance for all compositions, but there is a noticeable trend to somewhat higher content of areas imaged as "hard". This is expected based on increase of siliceous domain content from < 1 to ~13 wt% (Table 2.1).

A representative set of images for a 45X fracture surface is shown in figure 2.5. The clear nanoparticle imaging in figures 2.5 contrasts with the "disappearance" of nanoparticles for this composition shown in figures 2.1, 2.2, S2.1, and S2.2. Like all fracture surfaces shown in figures S2.6 and S2.7, R_q for 45X is high, whereas R_q for the 45X coating surface is less than 10 nm.

2.5.6. Surface Wetting Characteristic. When possible, we have reported dynamic contact angle (DCA) data for silicones and related coatings.[49,50] However, the PDMS / nanocomposite resins were too viscous for two-sided dip coated samples. Only static contact angle measurements could be obtained for the spin coated films. Static contact angles are shown as a function of PDES(OEt) / $PDMS(OH)_2$ ratio (X) in figure 2.6. A regular decrease in contact angles occurs with increasing siliceous phase content. The highest contact angle is for 4X (115°) while the lowest (100°) is for 60X.

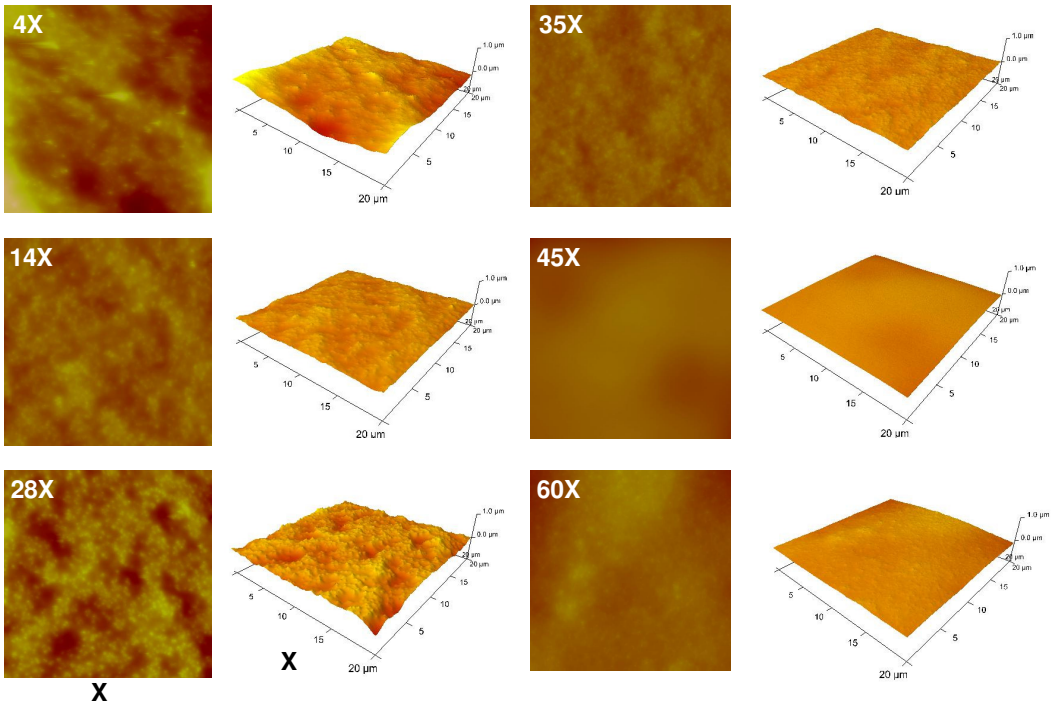

Figure 2.3. TM-AFM 2D (left) and the 3D (right) height images (20 x 20 µm) for U-FSN nanocomposites; Rq values are in figure 2.4 (Nanoscope V).

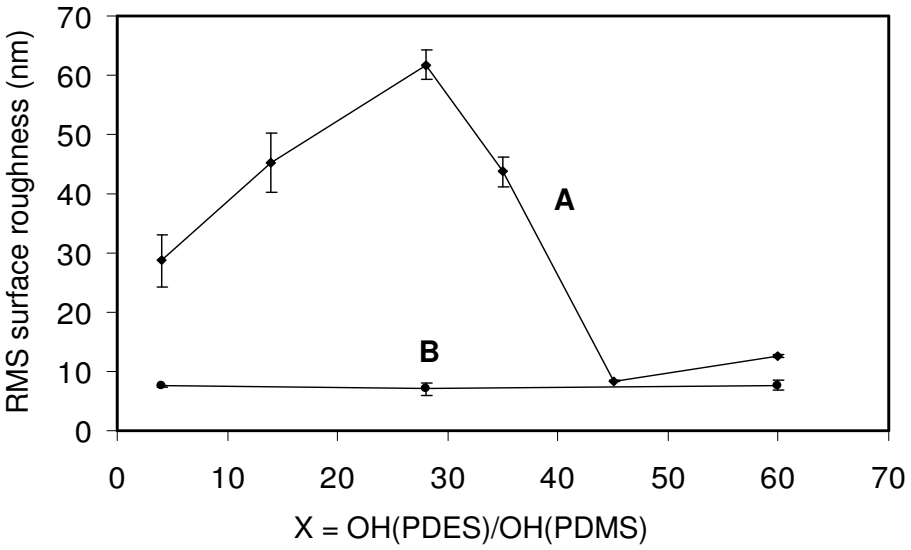

Figure 2.4. Variation in the RMS surface roughness (*R*q) for 20 x 20 µm 2D height images: **A**, U-FSN; **B**, T-FSN nanocomposites.

2.6. Discussion.

The intent of changing processing conditions for the PDMS nanocomposites was simply to achieve more homogeneous nanoparticle dispersion. Surprisingly, the near-surface nanoparticles "report" that high speed mixing changes AFM imaged near-surface morphology (Figures 2.1, 2.2, S2.1, S2.2).

The interpretation of the "message" reported by near-surface nanoparticles must take into account:

i. T-FSN nanocomposites

a. Images are virtually devoid of near-surface features; that is, nanoparticles are not detected / imaged or appear very faintly (Figure S2.5); T-FSN nanoparticles do not "report" as the trimethylsilylated are chemically inert.

b. Surfaces have uniformly low RMS roughness

c. Near-surface morphology and topology for the processing method described in Scheme 1 is identical to that observed previously for hand mixing.

ii. U-FSN nanocomposites

d. Roughness (R_q) is strongly dependent on siliceous domain wt% (Figure 2.4).

e. Compared to hand mixing where nanoparticles "disappeared" at 14X, the same phenomenon occurred at 45X when high speed mixing was employed

iii. Considerations common to T-FSN and U-FSN

f. Due to condensation cure a steady increase in shrinkage occurs with increased initial PDES content (Table 2.1); shrinkage reaches 12.3 vol% for 60X

g. AFM bulk fracture surface images for T-FSN and U-FSN are virtually indistinguishable.

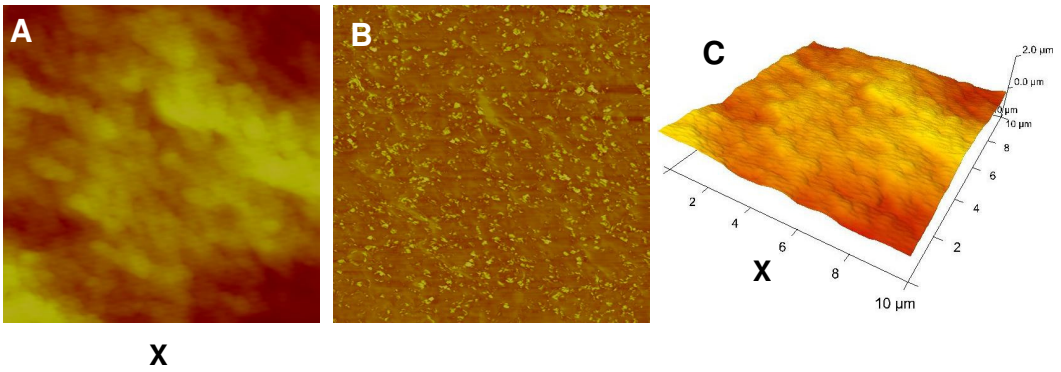

Figure 2.5. Representative 20 x 20 µm AFM fracture surface images for U-PDMS-45X: **A**, 2D height; **B**, phase; and **C**, 3D height. The orientation of the x axis in the 3D height image is shown.

The model proposed in figure 2.7 is an integration of prior results for VLS mixing technique (Figure 2.7A), new results for HS mixing (Figure 2.7B) and T-FSN PDMS nanocomposites (Figure 2.7C). The model for "disappearing" and reappearing nanoparticles described earlier is unchanged (Figure 2.7A). That is, at 14X, the surface siliceous domain blocks detection of the U-FSN. At higher siliceous domain volume fractions, the ready reaction of PDES ethoxy and hydroxy groups (Si-OEt_{PDES}, Si-OH_{PDES}) with U-FSN surface Si-OH (Si-OH_{nano}) effects a mechanical connection of the AFM tip with the nanoparticles, which are easily imaged. T-FSNs are inert and are not detected or provide very faint images (Figure 7C).

The model for U-FSN PDMS nanocomposites generated by HS mixing (Figure 2.7B) is based on competition of reactive PDMS end groups (Si-OH_{PDMS}) and PDES ethoxy and hydroxy groups (Si-OEt_{PDES}, Si-OH_{PDES}) for U-FSN surface Si-OH (Si-OH_{nano}).

2.6.1. Stage 1. With reference to Scheme 2.1, initial HS mixing of PDMS and U-FSN (2700 rpm; 4 x 60 sec) results in PDMS chain ends bound to U-FSN nanoparticles. At this stage, the interaction may be through H-bonding (chemisorption) or covalent bonding (condensation to Si-O-Si). Scheme 2.1 (upper right) represents bonded chains with bold lines and nanoparticles to which these chains are bound as filled circles. Figure 2.7B depicts four PDMS chains as small circles attached to nanoparticles. The depiction ignores the broad molecular weight distribution of PDMS chains and the disparity between the size of U-FSN (~ 50 nm) and 26 kDa PDMS chains. For the latter, the RMS end-to-end distance is ~7.5 nm using the valence angle model.[51]

2.6.2. Stage 2. After addition of PDES, competition for reaction of Si-OH_{PDMS}, Si-OEt_{PDES}, and Si-OH_{PDES} with Si-OH_{nano} occurs. A myriad of condensation reactions are simultaneously underway as network formation that parallels sol-gel chemistry is initiated.

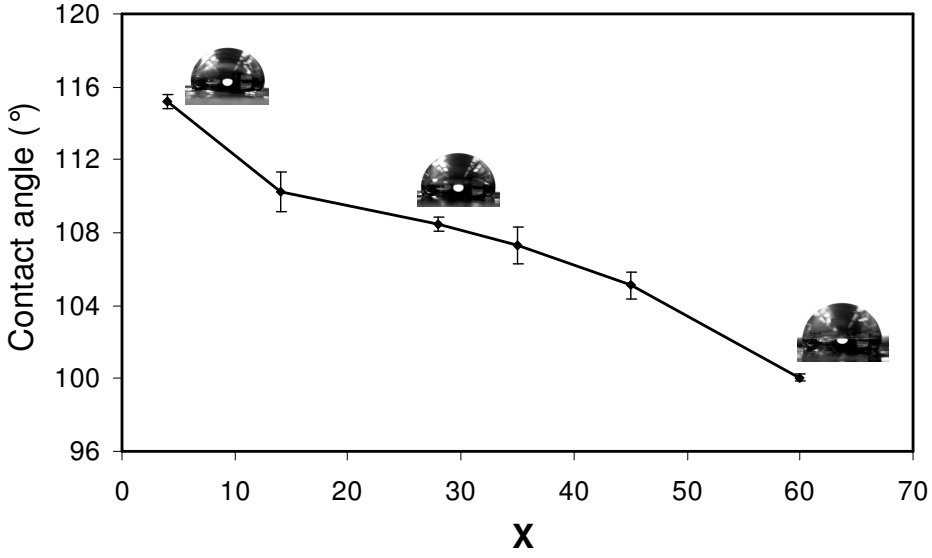

Figure 2.6. Static contact angles of the coated slides with variation in the siliceous phase concentration (X).

PDES is comprised of multiple species including dimers, trimers, tetramers, and oligomeric species,[36] all of which can undergo condensation reactions with PDMS chain ends, other PDES species, and Si-OH_{nano}. However, the presence of adsorbed or chemisorbed PDMS chains on U-FSN blocks reaction of PDES species with Si-OH_{nano}.

The model in figure 2.7B is based on the notion that nanoparticle-bound PDMS chains form a kinetic barrier to reaction of PDES species with Si-OH_{nano}. A corollary to this proposed scheme is that nanoparticles with bound PDMS chains tend to have higher near-surface concentrations compared to U-FSN. Such nanoparticles with bound PDMS chains may be designated "S-FSN". The suggestion that S-FSN tend to have higher near-surface concentrations compared to U-FSN follows their lower surface free energy and better compatibility with the PDMS matrix. It follows from the model proposed in figure 2.7B that the near-surface concentration of S-FSN shifts the "disappearance" of nanoparticles to higher siliceous domain concentration (45X) compared to compositions prepared by very low speed (VLS) processing conditions where U-FSN are the dominant nanoparticle species (Figure 2.7A). "Disappearance" is a gradual process as AFM phase images of 35X show the beginning (Figure 2.1, 2.2, S2.1, S2.2). The "reappearance" of nanoparticles at 60X results from a higher concentration of PDES overcoming the blocking effect of surface concentrated PDMS chains. That is, increased PDES results in increased concentration of numerous molecular intermediates containing –SiOH that compete for the formation of –Si-O-Si- bonds on the nanoparticle surfaces. In turn, this results in enhanced mechanical connectivity to the AFM probe by virtue of the increased near-surface volume fraction of rigid siliceous phase depicted in the last frame of figure 2.7B.

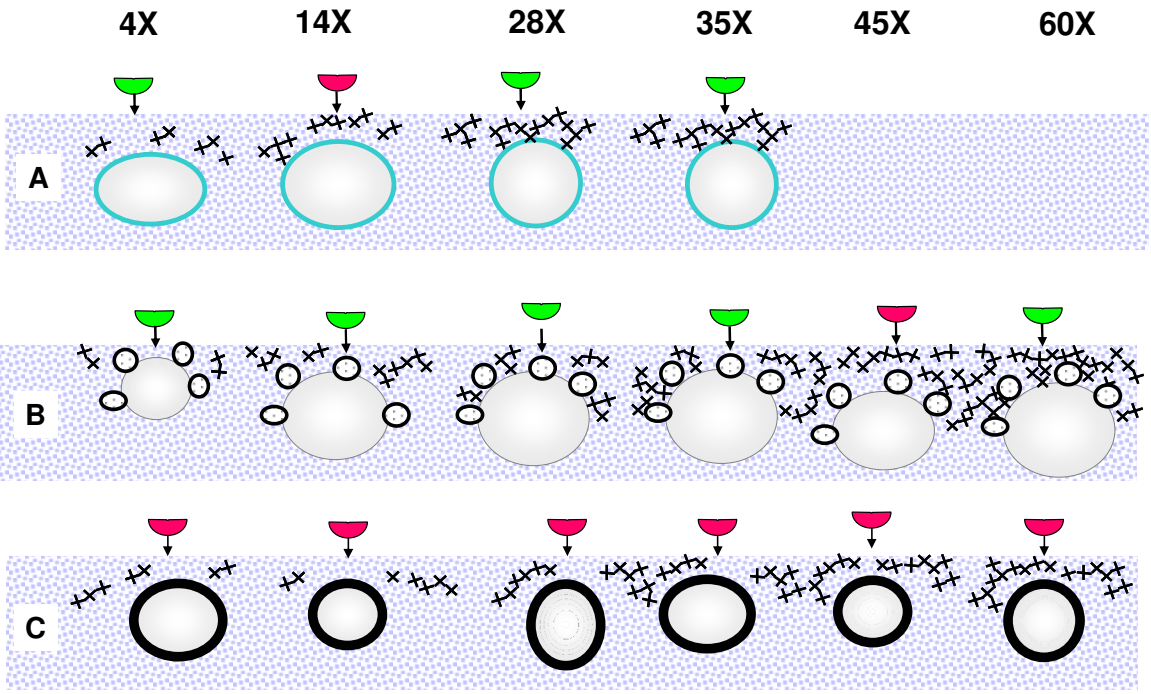

Figure 2.7. Model for surface morphology of U-FSN/PDMS nanocomposites as a function of siliceous domain content: **A**, hand mixed; **B**, high speed mixing; **C**, T-FSN nanocomposite. AFM tip indicates nanoparticle imaged (green) or not (red); "**x**" represents siliceous domain $Si(-O-)_4$ tetrahedron; background pattern is PDMS matrix.

The proposed emergence of the siliceous domain at high PDES concentration (45X) seems counter-thermodynamic. Based on self-condensation alone, the PDES-derived siliceous domain should be polar and glass-like precluding surface concentration. Nevertheless, contact angles decrease regularly (decreasing hydrophobicity) from the lowest (5X, 114°) to highest (60X, 100°) siliceous content (Figure 2.6). From wetting behavior, we conclude that the siliceous domain has a gradually increasing, water accessible area fraction, decreasing the water contact angle by 14º at 60X. This emergence is likely facilitated by increased volumetric shrinkage at higher siliceous domain content, as this phase is relatively rigid and less mobile compared to the PDMS-rich domain.

The combined reaction of PDMS and PDES with the nanoparticles apparently results in nanoparticle aggregates due to PDMS chain / siliceous domain bridging. Aggregates result in increased roughness (R_q, Figure 2.4) that is synergistic with increased shrinkage until the 45X composition, where the formation of a continuous near-surface siliceous domain results in a precipitous drop in R_q and nanoparticle "disappearance". The "reappearance" at 60X must result from the connection of the smooth, surface siliceous-rich domain with near-surface nanoparticles via bridging. Such bridges are rigid and afford a mechanical connection of the tip to the near-surface nanoparticles.

2.7. Conclusion

U-FSN/PDMS nanocomposites prepared using high speed (HS) mixing has a compositional dependent surface morphology (Figures 2.1, 2.2) which is different from that obtained previously for identical compositions using a VLS mixing technique. A surface morphological model (Figure 2.7B) is proposed based on a competition for U-FSN surface Si-

OH (Si-OH_{nano}) by PDMS -SiOH end groups (Si-OH_{PDMS}) and PDES ethoxy and hydroxy groups (Si-OEt_{PDES}, Si-OH_{PDES}). At low PDES concentrations (4X-35X), nanoparticle-bound PDMS (S-FSN) inhibits reaction of PDES species with Si-OH_{nano}. In addition, nanoparticle-bound PDMS chains facilitate matrix compatibility and near-surface concentration as well as surface roughness accompanying shrinkage. At 45X, the growing concentration of siliceous domain results in a continuous near-surface siliceous-rich domain and nanoparticle "disappearance" (Figures 2.1, S2.1, and 2.7B, 45X). A noteworthy reduction in coating roughness accompanies the formation of this continuous surface layer (Figure 2.4). This is the same phenomenon proposed previously for the 14X composition processed by VLS mixing (Figure 2.7A 14X).[38,39] However, the mild processing conditions utilized previously must not have facilitated the "mechano-chemistry" that occurs under HS mixing, viz., the reaction of PDMS –OH chain ends with $SiOH_{nano}$. Under mild VLS "hand mixing" used previously, PDES competed more favorably for Si-OH_{nano} resulting in nanoparticle "disappearance" at a lower siliceous domain content (14X).

At the 60X composition, nanoparticles "reappear". This detection is attributed to a mechanical connection through the near-surface siliceous domain that enables tip-nanoparticle interactions (Figures 2.1, S2.1, and 2.7, 60X). The reduced contrast of the nanoparticles in the 60X phase image (Figure S2.3B) is attributed to reduced tip-nanoparticle interactions due to the intervening siliceous domain.

While the emergence of a polar siliceous domain surface area fraction seems counter-thermodynamic for coatings generated in air, water contact angles decrease by 14º from 4X to 60X compositions; that is, the PDMS nanocomposites become more less hydrophobic at high siliceous domain content (Figure 2.6). Volumetric shrinkage (loss of ethanol) accompanies higher initial polydiethoxysiloxane weight fractions, which may result in increased surface

exposure of siliceous domain. The presence of PDMS chains bound to the near-surface siliceous domain presumably acts to buffer against an even steeper decline in water contact angles.

The results reported herein are guiding additional studies aimed at understanding the complex interplay of composition and processing that affect the morphology for systems containing PDMS, nanoparticles, and a siliceous domain from condensation cure. The goal is to obtain additional insights that will facilitate systematic tuning of properties for these important materials, which are used widely in applications ranging from caulks, sealants, and foul-release marine coatings to sophisticated biomaterials.

2.8. Supporting Information.

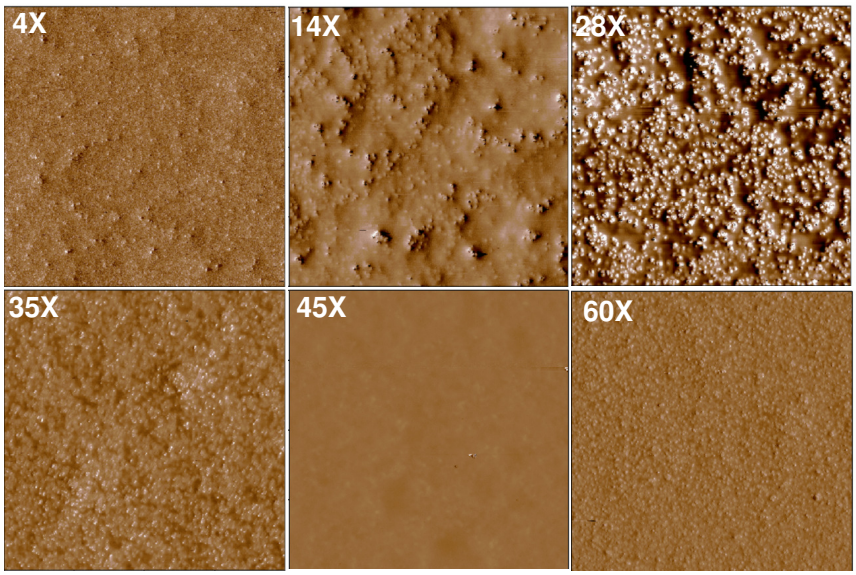

Figure S2.1. Phase images (20 x 20 µm, z = 30°) for U-FSN-PDMS samples cured at 100 °C for 72 hours (Asylum MFP-3D).

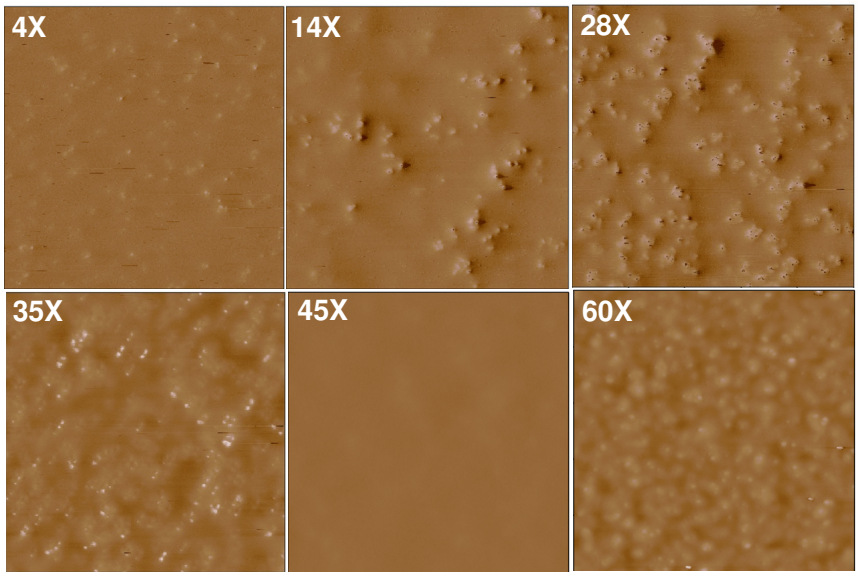

Figure S2.2. Phase images (5 x 5 µm, z = 40°) for U-FSN nanocomposites. (Asylum MFP-3D).

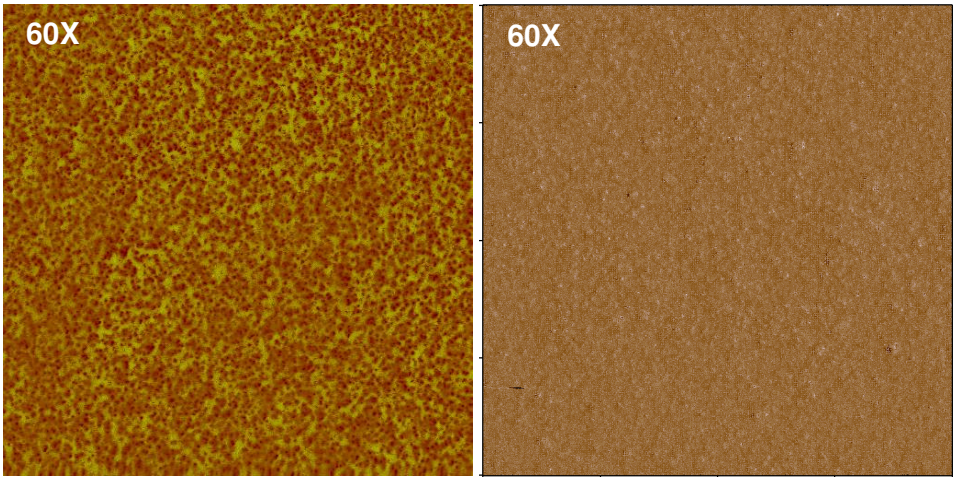

Figure S2.3. Enlarged 20 x 20 µm phase image (z = 40°) for U-FSN-60X. Left, Nanoscope V from Figure 2.1; right, Asylum MFP-3D, from figure S2.1.

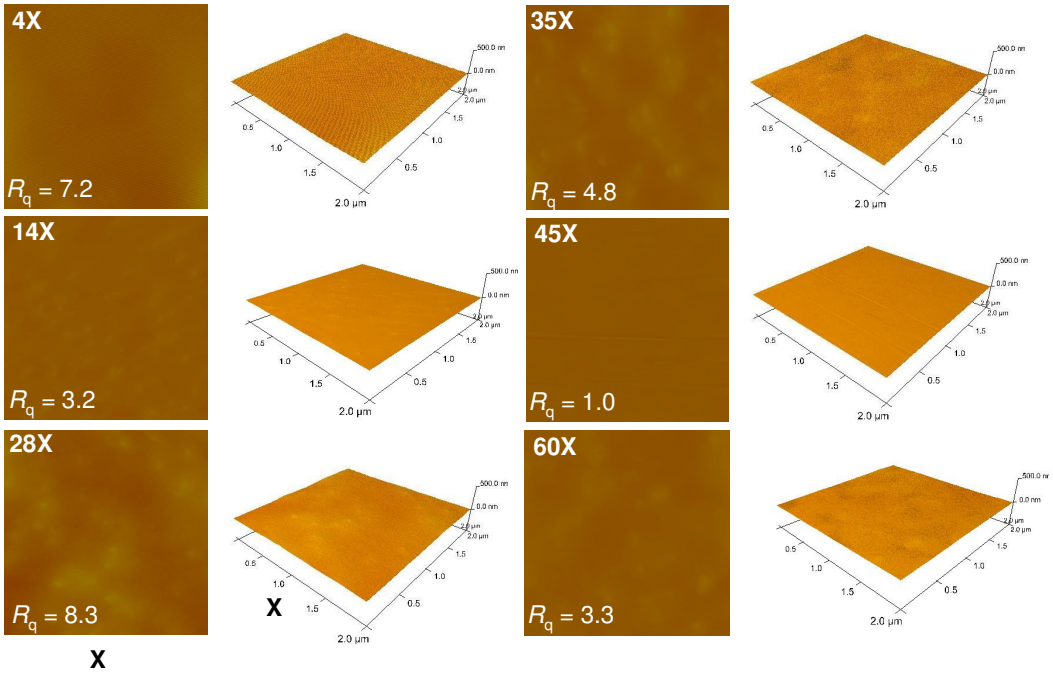

Figure S2.4. TM-AFM 2D (left) and the 3D (right) height images (r_{sp} = 0.8, 2 x 2 μm) for U-FSN- nanocomposites.

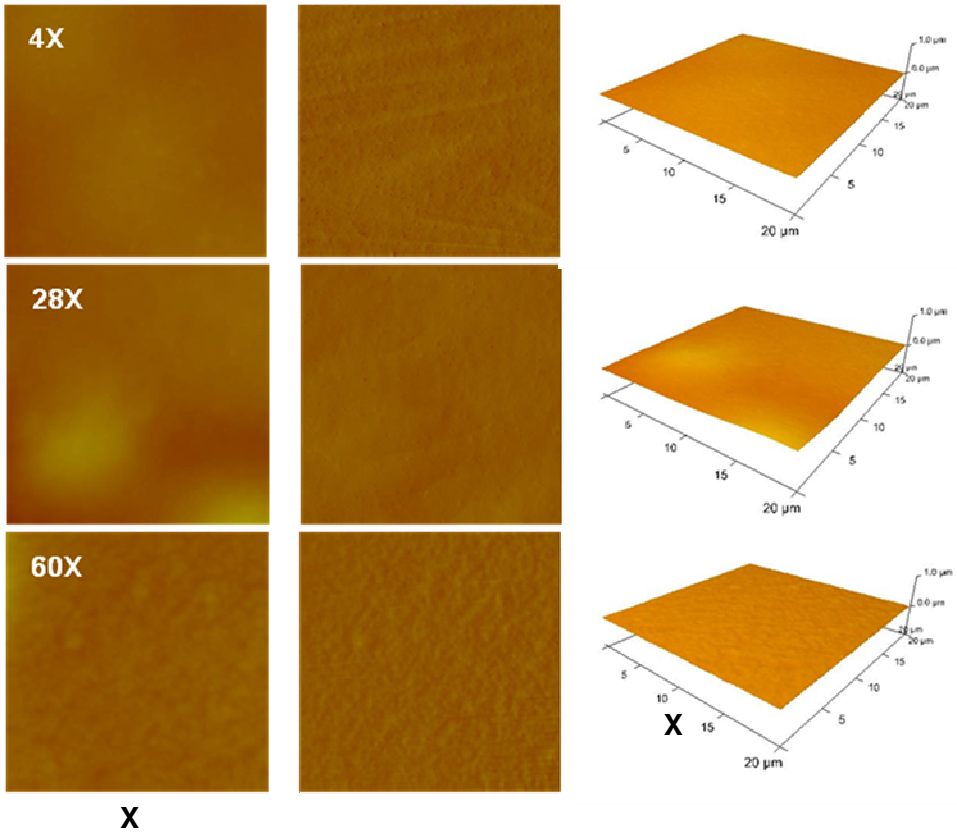

Figure S2.5. TM-AFM 2D height, phase and 3D height images (20 x 20 µm) for 4X, 28X and 60X T-FSN nanocomposites. *R*q (nm) = 7.5, 7.1, and 7.7 respectively.

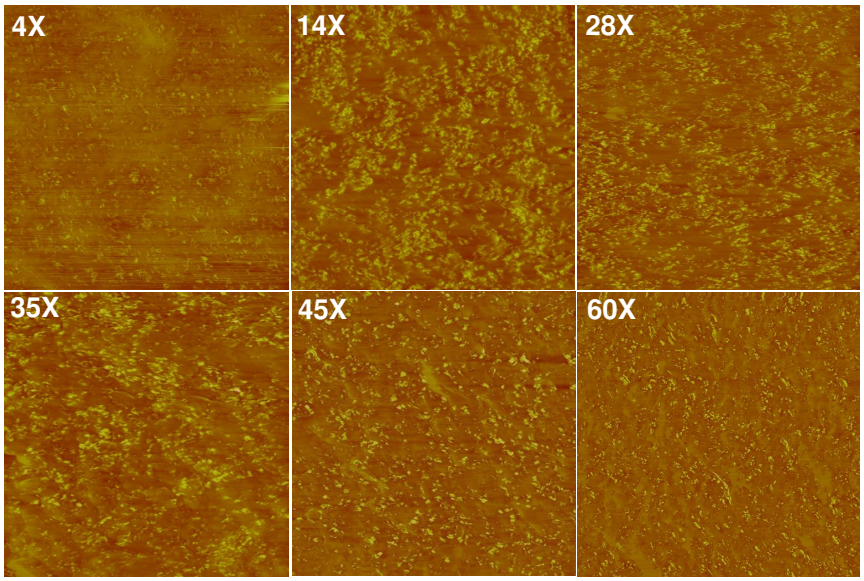

Figure S2.6. 10 x 10 µm, fracture surface phase images (r_{sp} = 0.85, z = 75°) for U-FSN nanocomposites.

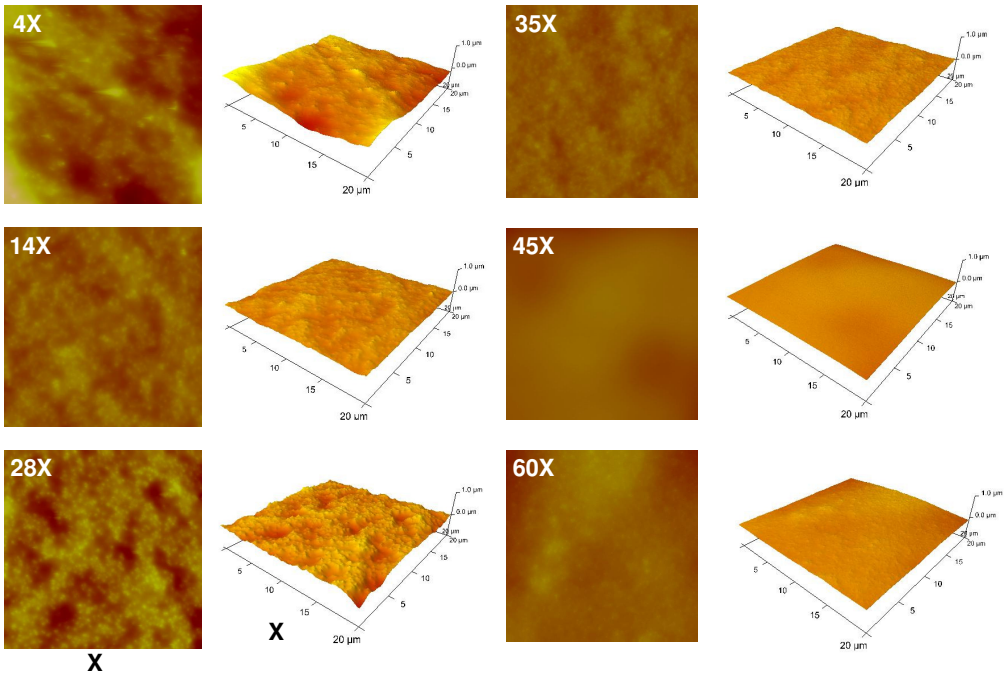

Figure S2.7. TM-AFM 2D (left) and the 3D (right) height images for fracture surfaces (10 x 10 μm) of U-FSN nanocomposites.

CHAPTER 3

Polydimethylsiloxane - Fluorous Polyoxetane Triblock Urethane Urea Copolymers.

3.1. Introduction

Silicone elastomers have importance due to low dielectric constant and high dielectric breakdown strength,[52] low surface tension[53] and good thermal stability (~ 250 ºC).[28] In addition to a very low glass transition temperature, (T_g ~ -120 ºC) hydrophobicity and ease of fabrication have led to common use as caulks, adhesives, and coatings.[31] Good biocompatibility[29,30] has resulted in applications as biomaterials.[32,54]

Condensation or hydrosilylation cured elastomers have weak mechanical properties.[15-17] Routes to improving strength include reinforcement with nanoparticles such as fumed silica,[20-23] and ceramics,[25] zeolites[24] Alternatively, polyurethanes and polyureas with PDMS soft blocks have excellent mechanical properties, even at relatively low hard block weight percents.[55-57] A combination of urea linkages with fumed silica nanoparticles has been explored to improve mechanicals further.[58]

Polydimethylsiloxane-based elastomers (δ = 7.3 $(cal/cm^3)^{1/2}$) are swollen in organic solvents such as hexane due to similar solubility parameters.[50] Several approaches have been explored to lower silicone surface tension by introducing C_nF fluorinated groups (n = perfluoro C atoms). It is well known that the trifluoropropyl side chain confers oleophobicity.[59-61] Polysiloxanes with higher fluorinated content are also oleophobic, but the advantages for introduction of higher fluorine content must be weighed against higher cost.[59,62] Alternatives continue to be explored including the introduction of highly oleophobic perfluoropolyether

moieties for increased resistance of silicones to organics in applications such as microfluidics.[53,63]

At low wt%, fluorous surface modifiers can introduce oleophobicity Simply blocking diffusion of cyclics and other low molar mass components is important to micro- and nanomolding[64] and biomedical applications.[54] At < 0.4 wt% copolyacrylates having C_8F semifluorinated and silicone side chains improved PDMS oleophobicity, but higher concentrations oleophobicity was reduced due to phase separation of the surface modifier.[50,65] A $C_{10}F$ semifluorinated trialkoxysilane was used for imparting oleophobicity to condensation cured PDMS,[34] but the surface was mechanically fragile.[35] While surface modifiers with C_8F and $C_{10}F$ side chains confer resistance to oil, these moieties can degrade to perfluorooctanoic acid (PFOA) which is bioaccumulative.[66] Thus, the surface modifier approach has an extra challenge of surface modification with short fluorocarbon side chains.[67]

The present study describes incorporation of a C_1F fluorous polyoxetane block into a reactive PDMS-3F-PDMS (ABA) triblock that undergoes condensation cure (Scheme 3.1). The results indicate an unusual combination of properties including compositionally dependent microscale / nanoscale phase separation. Despite low urea / urethane content, the triblock elastomers have tough mechanical properties. XPS and dynamic contact angle measurements reveal a PDMS-like surface for these optically transparent elastomers (Figure S3.1).

3.2. Experimental

3.2.1. Materials. PolyFOx diols PF 636 and PF 6320 was generously provided by OMNOVA Solutions, Inc. Aminopropyl terminated PDMS (DMS-A21, 90-120 cSt, manufacturer's M_w, 4.5 kDa) and 3-isocyanatopropyltriethoxysilane (SII 6455) were purchased from Gelest, Inc.

Methylene bis-(4-cyclohexylisocyanate) (HMDI) and dibutyltin diacetate were purchased from Aldrich. Bis(triethoxysilyl)ethane (SIB 1817, BTESE) was obtained from Gelest, Inc. Tetrahydrofuran, 99.6%, (for analysis ACS, stabilized with BHT) was obtained from Acros.

Fluorinated polyoxetanes diols are purified by liquid-liquid extraction as previously described in detail.[68] In brief, as received 3F diols (Scheme 3.1) are extracted ~10 times with hexane to yield 3F-1.1 and 3F-4.5, where M_n is indicated in kDa; polydispersities are 1.15 and 1.26 respectively.

3.2.2. Coating Preparation. With reference to Scheme 3.1, a three step reaction was carried out in a single vessel. (1) 3F diol end capping with HMDI **2** to gave **I**; (2) Reaction with aminopropyl terminated PDMS **3**, gives **II**; (3) End-capping the triblock with 3-isocyanatopropyltriethoxysilane, **4** provides the reactive triblock **III**. Subsequently, hydrolysis / condensation (moisture cure) generates crosslinked elastomers. Elastomers prepared with 3F-1.1 and 3F-4.5 are designated as A-1.1 and A-4.5, respectively. The weight percent siliceous component was increased for two other compositions by addition of 10 wt% BTESE (Scheme 3.1) to give B-1.1 and B-4.5. A detailed composition of the triblock elastomers are provided in Table 3.1.

In a typical reaction, 5 g (1.11 mmol) 3F-4.5, 0.58 ml (2.22 mmol) **2** and dibutyltin diacetate (DBTDA, 0.5 wt%) in THF (10 g) were stirred continuously for 4 hr at 60 °C under a dry nitrogen purge. The reaction was monitored by FTIR to confirm formation of the urethane linkage. Disappearance of the OH absorption was followed by appearance of NCO and NH absorptions indicating completion of step (1).

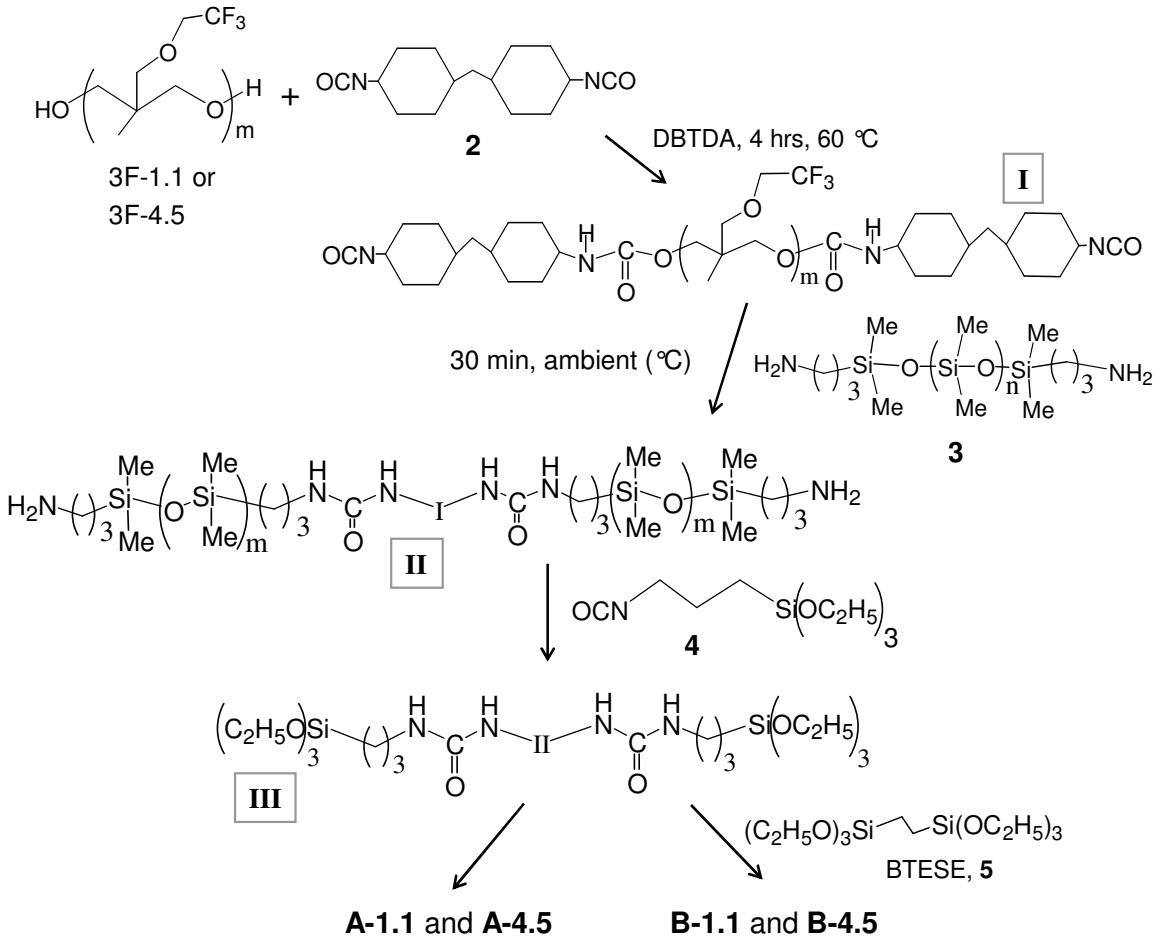

Scheme 3.1. Three step synthesis of reactive triblock copolymer intermediate **III** (See text for composition).

For step (2) heating was terminated and 11.1 g (2.22 mmol) **3** was added. After 30 min the NCO peak (2200 cm^{-1}) disappeared, signaling complete reaction of isocyanate end groups. (3) End-capping with 0.55 ml (2.22 mmol) 3-isocyanatopropyl triethoxysilane **4** gave **III**. Subsequently, viscosity built up in 15 min as hydrolysis / condensation cure is catalyzed by residual DBTDA catalyst. Microscope slides were drip coated (AFM, ATR-IR); glass cover slips were dip coated (DCA); plaques were formed by pouring the remaining **III** into a PTFE dish. Cure was overnight at ambient temperature followed by 100 °C for 24 hr.

3.3. Instrumentation / Characterization.

3.3.1. Thermogravimetric Analysis. TGA was done with a TA-Q 5000 Series™ instrument (TA Instruments) from 20 to 1000 °C. Samples were placed in platinum pans and heated in a nitrogen atmosphere at a flow rate of 20 ml/min. Mass loss and derivative mass loss was monitored. Table 3.2 lists the 5% weight loss temperature ($T_{5\%}$) and the maximum rate loss temperature (T_{max}).

3.3.2. Modulated Differential Scanning Calorimetry. M-DSC was done with a TA-Q 1000 Series™ instrument (TA Instruments) with modulation amplitude of ± 0.5 °C and modulation period of 20 s. The sample (5-15 mg) was equilibrated at -90 °C followed by a heating ramp of 15 °C/min to 225 °C. Zinc, tin and lead standards were used for energy and temperature calibration.

3.3.3. Mechanical testing. Dynamical mechanical and tensile mechanical properties of the coatings/films were measured using a TA instruments RSA III dynamic mechanical analyzer (DMA). For DMA, sample temperature was ramped from -120 to 200 ^{o}C at 5 ^{o}C/min (1Hz) with maximum strain set to 0.05%. Maximum autotension was set to 2 mm with a maximum autotension rate of 0.01 mm/s.

Table 3.1. Composition for the triblock copolymers.

Designation	Elastomer Composition	Wt. % feed/ Wt. % elastomer/ mol % elastomer				
		3F[a]	HMDI[b]	PDMS[c]	$OCN(CH_2)_3Si(O)_{1.5}$[d]	$Si_2(CH_2)_2(O)_3$[e]
A-1.1	(3F-1.1)H/(Si-4.5)	9.1/9.2/14.3	4.3/4.4/28.6	82.5/84.1/28.6	4.1/2.3/28.6	--
A-4.5	(3F-4.5)H/(Si-4.5)	24.6/25/14.3	3.4/3.4/28.6	68.6/69.6/28.6	3.4/1.9/28.6	--
B-1.1	(3F-1.1)H/(Si-4.5)(BTSE-10)	8.2/8.9/9.3	3.9/4.2/18.5	74.3/80.6/18.5	3.6/2.2/18.5	10/4.1/35.3
B-4.5	(3F-4.5)H/(Si-4.5)(BTSE-10)	22.2/24/8.6	3/3.3/17.2	61.9/66.8/17.2	3/1.8/17.2	10/4.1/39.8

a. 3F diol feed.
b. Diisocyanate **2** feed.
c. Diamine **3** feed.
d. End capper $OCN(CH_2)_3Si(OC_2H_5)_3$ **4** feed.
e. BTSE feed.

For tensile testing, samples were stamped out of cast plaques, which were measured for thickness, width and gauge prior to mounting in the RSA III tensile clamps. Data acquisition rate was 1 Hz while the initial sample elongation rate was 10 mm/min. Modulus, ultimate strength and elongation at break was determined.

3.3.4. Tapping Mode Atomic Force Microscopy (TM-AFM). A Dimension Nanoscope V (Veeco, CA) atomic force microscope in tapping mode with silicon crystal cantilevers (40 N/m) was used for morphological analysis. Imaging was performed at a setpoint ratio r_{sp} or A_{exp}/A_o of 0.9 (soft tapping), where A_o is free oscillation amplitude and A_{exp} is the experimental oscillation amplitude.

3.3.5. X-ray photoelectron spectrometry (XPS). Measurements were carried out on a Thermo Fisher Scientific ESCALAB 250 instrument. Analysis utilized monochromatic Al Kα X-rays and with an X-ray spot size of 500 mm and a TOA of 90°. Pass energy for survey spectra was 150 eV. Pressure in the analytical chamber during spectral acquisition was maintained at 2×10^{-8} Torr while an argon electrostatic flood source affected charge neutralization. Cured triblock samples were cut and attached to the surface of a silicon wafer using carbon tape. Data were analyzed with the Thermo Avantage software (v4.40).

3.3.6. Attenuated total reflectance infrared (ATR-IR) spectroscopy. ATR-IR spectra were obtained by using a Nicolet 400 FT-IR with Thunderdome attachment. Coated microscope slides were secured on a diamond crystal that interrogates to a depth of 1.65 μm.

3.3.7. Wetting Behavior. Dynamic contact angles (Wilhelmy plate method)[69,70] were obtained using a Cahn model 312 instrument. Deionised water or isopropanol were used as probe liquids with an immersion/withdrawal rate of 100 μm/s. Reported contact angles (± 1–2°) are averages of several force-distance cycles.

3.3.8. Refractive index. Refractive indexes of 3-aminopropyl polydimethylsiloxane, 3F diol-1.1 and 3F diol-4.5 were measured by the r^2mini refractometer, Reichert Analytical Instruments. A drop (~ 0.2 ml) of the sample was placed on the measuring well and allowed to equilibrate to the temperature of the instrument. Refractive index of the sample was read and an average value of three readings has been reported here.

3.4. Results and Discussion

3.4.1. Triblock preparation and coating. PDMS-3F-PDMS triblock copolymers are prepared from commercially available constituents according to Scheme 3.1. The central 3F block is poly(3-(2,2,2-trifluoroethoxymethyl)-3-methyloxetane), **1**. Of note is liquid-liquid extraction used to remove cyclics and low molar mass (LMM) species from 3F-1.1 and 3F-4.5 diols. The resulting 3F-1.1 and 3F-4.5 diols **1** have low polydispersity (< 1.2).[68] The reaction of 3F diols with HMDI **2**, methylene bis-(4-cyclohexylisocyanate), occurs under conditions often used for urethane formation with aliphatic diols (DBTDA catalysis, 60 °C / 4 hr, N_2).[71,72] FTIR spectroscopy confirmed the completion of step 1 (Figure 3.1). The 3F-4.5 diol spectrum has a broad peak at 3500 cm^{-1} characteristic of chain end -OH.

After end capping to form **I**, the –OH peak disappears while an absorption at 2200 cm^{-1}, characteristic for chain end isocyanate groups appear. Absorption at ~ 3300 cm^{-1} is typical for NH in urethane. PDMS diamine **3** reacts exothermically with **I** to give diamine terminated **II**. This reaction is complete in ~ 30 min. In Figure 3.1 the spectrum of **II** confirms end capping by the presence of an NH peak at ~ 3300 cm^{-1} and the absence of NCO absorption at 2200 cm^{-1}. The third step is end capping **II** with $OCN(CH_2)_3Si(OEt)_3$ **4** to give reactive triblock **III**.

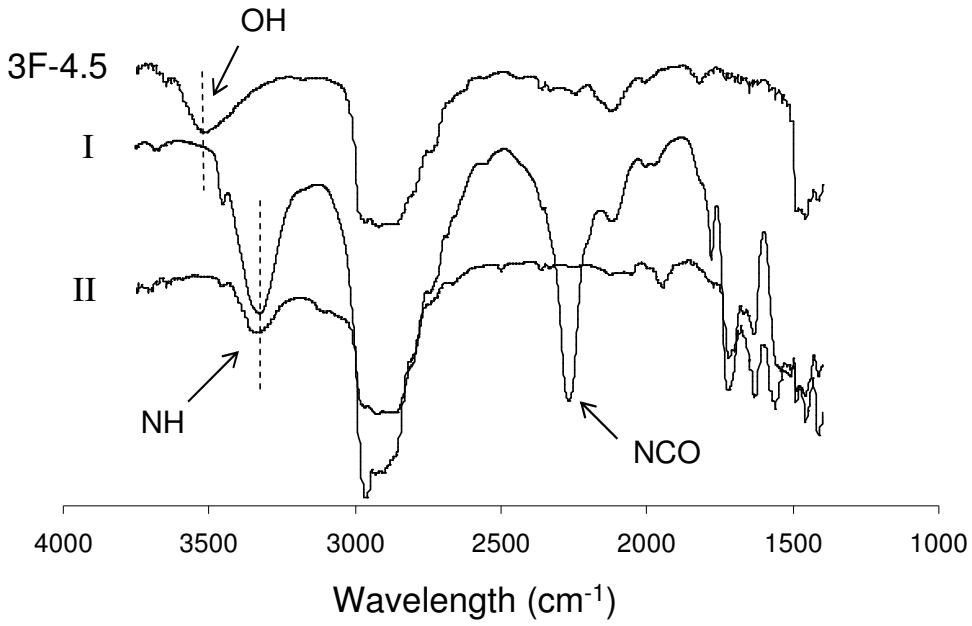

Figure 3.1. FTIR spectra of intermediates, monitoring different stages of the triblock reaction.

This step, which also involves an amine-isocyanate reaction, occurs spontaneously at ambient temperature (~30 min). Once **III** is generated, condensation cure commences since DBTDA catalyst is present from step 1. Network formation through hydrolysis / condensation cure gives optically transparent coatings and plaques. The resulting compositions are designated A-1.1 and A-4.5, respectively (Table 3.1) and differ by the M_n of the 3F block.

The siliceous content for A-1.1 and B-1.1 is ~2 wt%. To explore the consequences of an increased siliceous component, 10 wt% BTESE, **5** was added for two other compositions (Scheme 3.1) to give B-1.1 and B-4.5. BTESE has been used in the preparation of porous oxycarbosilane spin-on low dielectric thin films.[73-75] Hydrolysis / condensation cure of **III** alkoxy end groups and BTESE gives an oxycarbosiliceous domain. For BTESE, $Si_2(CH_2)_2O_3$ is the nominal composition after hydrolysis / condensation (Eq 3.1). For brevity, the hydrolysis / condensation cure product is designated "siliceous".

$$Si_2(CH_2)_2(OEt)_6 + 3H_2O \rightarrow Si_2(CH_2)_2(OH)_6 + 6\ C_2H_5OH \rightarrow Si_2(CH_2)_2O_3 \qquad \text{Eq 3.1.}$$

BTESE has not been used as a precursor for hybrids polymeric materials, that is, those containing inorganic and organic domains. Pioneering work by Saegusa and Chujo employed tetraethoxysilane, TEOS, as the precursor to a siliceous domain under water-rich conditions.[76,77] However, under water-sparse hydrolysis / condensation, TEOS and methyltriethoxysilane (MTEOS) are volatile resulting in a safety hazard in the laboratory and uncertain hybrid compositions.[37] Polydiethoxysiloxane (ES-40, PDES) attenuates mass loss due to alkoxysilane volatilization, but still contains about 10% TEOS. Also, some unreacted PDES constituents result in "blooming" of complex topological features over time.[78] In the present work, interest in

increasing the weight fraction of siliceous domain led to the choice of BTESE, which undergoes negligible volatilization during cure (b.p. 119 °C) and has good hydrolysis / condensation reactivity. No sign of time dependent surface features has been found for the hybrid compositions.

Assuming the stoichiometry shown by Eq. 3.1, the weight percent $Si_2(CH_2)_2O_3$ in hybrid triblocks B-1.1 and B-4.5 is shown in Table 3.1. A-1.1 and A-4.5 have ~2 wt% siliceous content while adding 10 % BTESE to the coating feed results in an increase to ~6 wt%. Dip or drip coating was used. Interestingly, triblock coatings were optically transparent (Figure S3.1). This observation prompted a refractive index (RI) determination for 3F-1.1 (1.405) and 3F-4.5 (1.401). The RI for the PDMS diamine was also determined and found in agreement with the literature value (1.406).[79] The virtually identical refractive indexes for PDMS and 3F blocks, which are majority components, (Table 3.1), account for optical transparency.

Two controls were prepared (Scheme 3.2). A PDMS control (C1) was obtained from the reaction of PDMS diamine **3** and 3-isocyanatopropyl triethoxysilane **4** followed by hydrolysis / condensation cure. This control has no HMDI and no 3F diol, but 2.3 wt% urea, which is comparable to the hybrid triblocks (Table 3.3). Secondly, a 3F-4.5 urethane-urea control (C2-4.5) was prepared by end capping **I** with 3-aminopropyltriethoxysilane followed by hydrolysis / condensation cure. C2-4.5 has 10 wt% hard block as conventionally determined based on HMDI. This composition has 1.5 wt% urethane and 2.1 wt% urea (Table 3.3).

3.4.2. Thermogravimetric Analysis. Thermal analysis was used to test the limits of thermal stability. Mass loss and derivative mass loss were determined from 20 to 1000 °C. A typical result is shown for A-4.5 in Figure 3.2. The 5% mass loss temperature ($T_{5\%}$) is 355 °C while the maximum mass loss rate (T_{max}) from the derivative peak is at 420 °C.

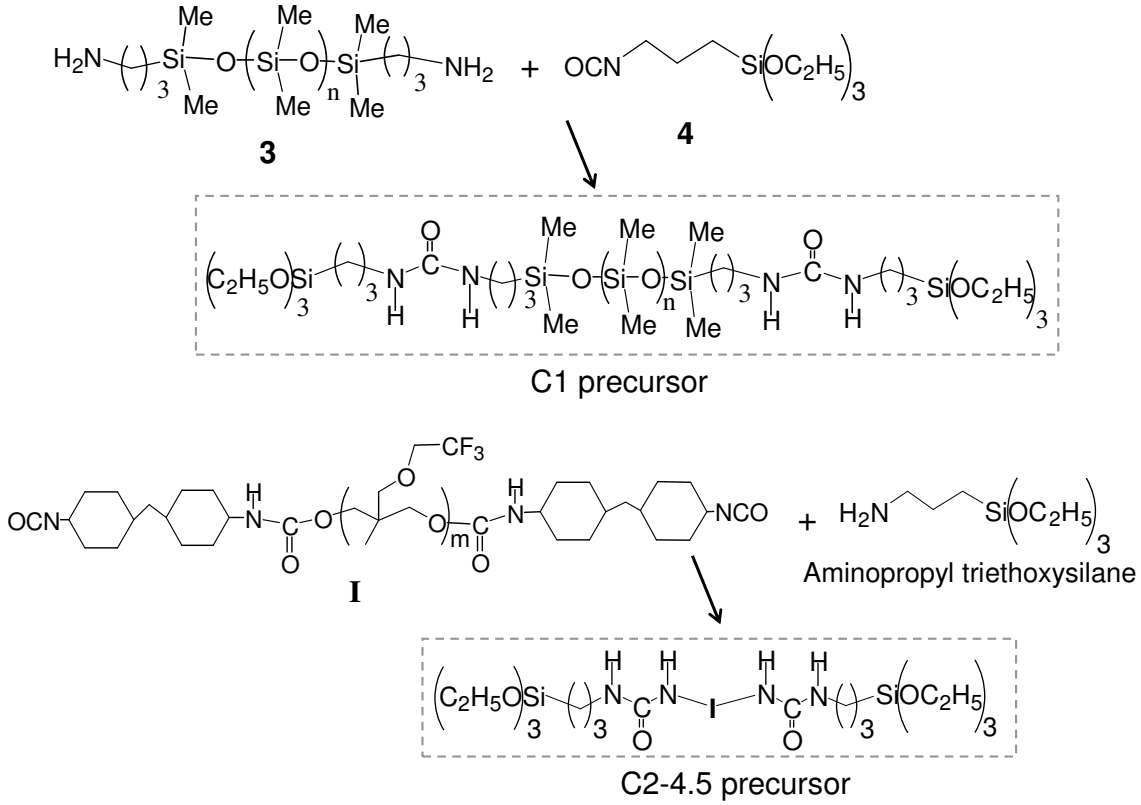

Scheme 3.2. Synthetic steps depicting the preparation of C1 and C2-4.5 (See text for compositions).

Table 3.2. Characterization data for the triblock copolymers.

Designation [Example]	TGA		Dynamic Mechanical Analysis (DMA)					Tensile test		Contact angles (°)	
	$T_{5\%}$ (ºC)	T_{max} (ºC)	PDMS T_g, (ºC)	3F T_g, (ºC)	Storage modulus (MPa)			Tensile modulus (MPa)	Strain at break (%)	θ_{adv}	θ_{rec}
					-90 °C	0 ºC	150 ºC				
A-1.1	331	433	-117	-30	200	3.5	1.7	2.1	328	114	77
A-4.5	355	441	-111	-29	210	3.8	2	2.3	492	118	72
B-1.1	320	445	-113	--	8	5.4	1.4	2	315	109	73
B-4.5	329	438	-114	-32	90	3.4	2.3	2.1	260	115	71
C1	--	--	-108	--	--	--	--	0.9	45	115	75
C2-4.5	230	437	--	-30	1910	4.7	2	2.2	580	108	51

At 900 °C, 0.6% mass remained, which is likely due to a silicon containing ceramic residue. The range for $T_{5\%}$ shown in Table 3.2 (320 - 355 °C) indicates good thermal stability for the hybrid triblocks. By this measure, A-4.5 has the greatest thermal stability ($T_{5\%}$ 355 °C). T_{max} for all PDMS-3F-PDMS hybrid elastomers is well over 400 °C (Table 3.2).

3.4.3. IR Spectroscopy. For ATR-IR spectroscopy with a diamond crystal the depth of penetration of the evanescent wave (~1.65 μm)[80] is ~1000 times that of XPS, TM-AFM, and DCA. Thus, ATR-IR spectra reveal primarily bulk intermolecular interactions and are considered before interpretation of mechanical and morphological determinations. The spectrum for B-4.5 is provided in Figure 3.3 (3500 – 500 cm^{-1}). A prominent peak at ~ 1200 cm^{-1} is assigned to C-F stretch (CF_3, 3F side chains).[81] A sharp C-H peak (~ 2900 cm^{-1}) and a broad N-H peak (~ 3350 cm^{-1}) are observed (Figure 3.3 inserts). Other absorptions are characteristic of PDMS.[82]

For polyurethanes and polyureas, two carbonyl stretching peaks usually occur from 1500 - 2000 cm^{-1}. The lower frequency peak is assigned to H-bonded carbonyls while the higher frequency peak is due to "free" carbonyls.[55, 58, 83-86] A depiction of hard segment-hard segment H-bonding shown in Figure 3.4A.

ATR-IR spectra for the triblock elastomers and controls (1500 - 2000 cm^{-1}) are shown in Figure 3.5. Control C2-4.5, with 10 wt% hard block has strong low frequency (H-bonded) and strong high frequency (disordered, "free") carbonyl absorptions typical of polyurethane ureas noted above.[55, 58, 83-86] Low frequency (H-bonded) carbonyl peaks at 1630 cm^{-1} are seen for all hybrid triblock compositions and are assigned to urethane/urea H-bonded C=O (Figure 3.4A).[58] However, the low frequency carbonyl absorption for hybrid triblocks is considerably weaker than that for control C2-4.5 (Scheme 3.2). Table 3.3 shows the higher urethane and urea content of C-2-4.5 (3.6 wt%) compared to A-1.1 (2.6 wt%) and A-4.5 (1.8 wt%).

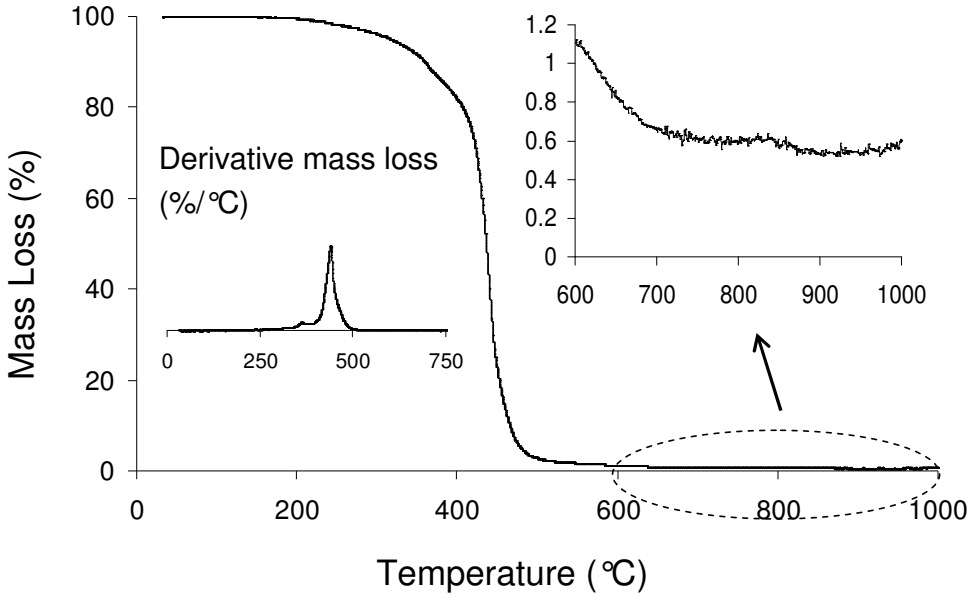

Figure 3.2. Thermogravimetric analysis on triblock A-4.5.

Table 3.3. Weight percent siliceous phases, urethane, urea and hard block.

Designation	$SiO_{1.5}$ (end capping)	$SiO_{1.5}$ (BTESE)	Total $SiO_{1.5}$	Urethane[a] NHC(O)	Urea[a] NHC(O)NH	Hard Block[b]
A-1.1	2.2	--	2.2	0.7	1.9	4.5
A-4.5	1.8	--	1.8	0.5	1.3	3.1
B-1.1	2	3.8	5.8	0.6	1.7	4.2
B-4.5	1.7	3.7	5.4	0.4	1.1	2.6
C1	4.8	3.5	8.3	--	2.3	--
C2-4.5	4.2	3.3	7.5	1.5	2.1	10

a. Urethane and urea wt% from elements shown.
b. With reference to Scheme 3.1, hybrid hard block wt% is the sum of HMDI, OH (3F), and NH_2 (**2** and **3**).

Control C2-4.5 contains 10 wt% hard segment by the usual convention of including HMDI. Allowing for the higher urethane and urea content of the control, the position and relative intensity of the 1630 cm^{-1} carbony peak for A-1.1 and A-4.5 are in good agreement.

The surprisingly weak, broad absorptions for the hybrid elastomers at ~ 1710 cm^{-1} nominally correspond to "free" urethane / urea C=O.[86] By this measure, the concentration of "free" C=O is low. Siliceous weight percents based on $-SiO_{1.5}$ are listed in Table 3.3. The siliceous domain formed by hydrolysis / condensation cure for all hybrids is likely fringed with -Si-OH. The absence or weakness of the high frequency absorption at 1710 cm^{-1} is attributed to carbonyl hydrogen bonding to Si-OH depicted in Figure 3.4B. This notion is supported by the virtual absence of the 1710 cm^{-1} absorption for B-1.1 and B-4.5, which have higher siliceous content.

Control C1 does not contain HMDI. Hence the synergistic hydrogen bonding of urea / urethane groups held in close proximity (Figure 3.4A) is not possible. As a consequence, the low frequency absorption for C1 is weak (Figure 3.5). There is a significant shift in this absorption to higher frequency (1640 cm^{-1}) which is another indicator of weak H-bonding. Finally, there is no clear indication of a discrete absorption for carbonyl hydrogen bonded to Si-OH in C1 or any of the hybrids. Apparently, a broad absorption envelop exists likely due to a variety of carbonyl interactions.

3.4.4. Atomic Force Microscopy. Plaques of the hybrid compositions were cast, cured, and fractured after immersion in liquid nitrogen. TM-AFM phase and 2D height images (10 x 10 μm) for the fracture surfaces are shown in Figure 3.6. Using light tapping (r_{sp}, 0.95) introduces fewer artifacts (such as scan lines) when surfaces are relatively uneven.

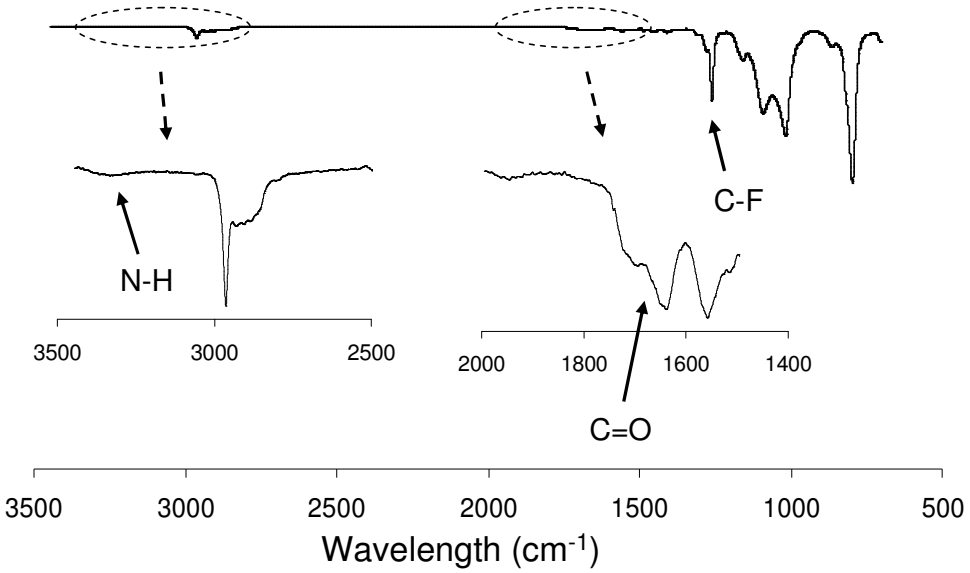

Figure 3.3. ATR-IR full spectrum for composition B-4.5 (See text for inserts).

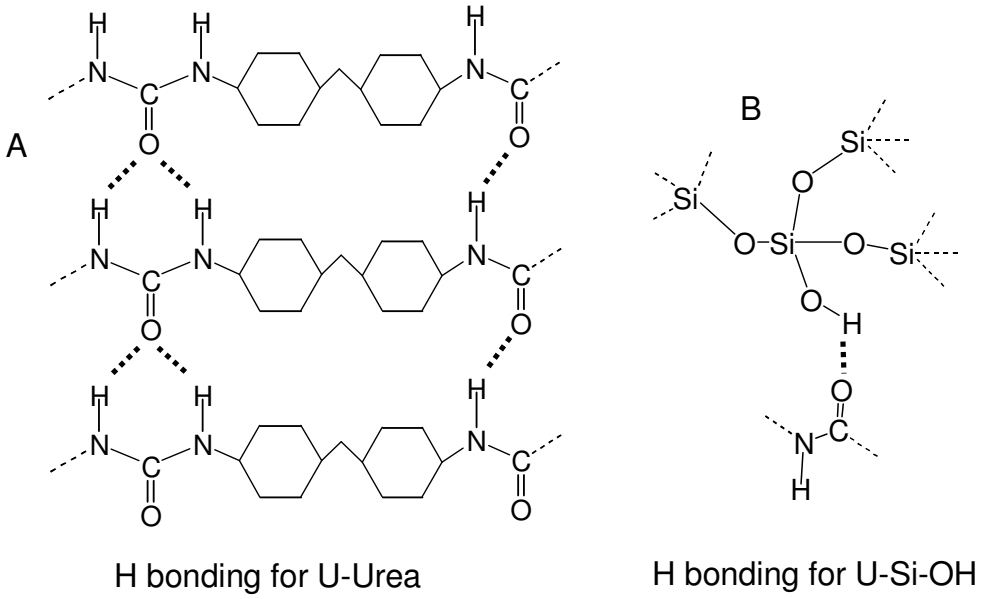

Figure 3.4. A schematic representation of H-bonding between, A – urethane and urea groups of different triblock chains and B – urethane and the siliceous phase. The H-bonds are represented as dotted lines in the scheme.

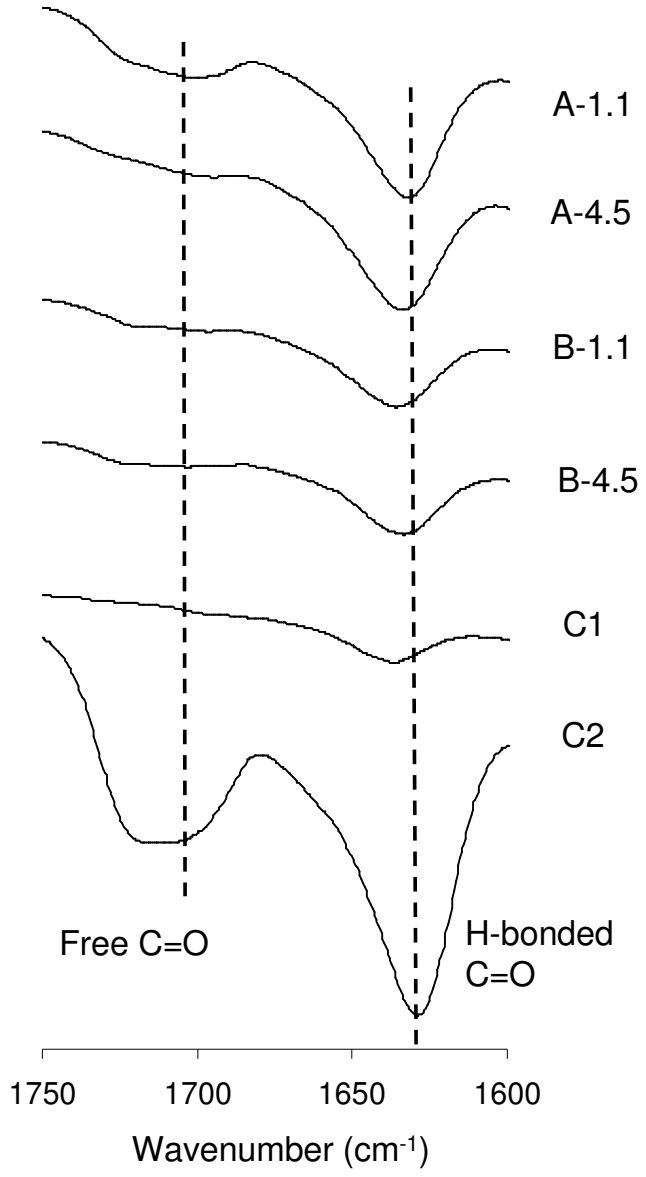

Figure 3.5. H-bonded and free carbonyl peaks by ATR-IR.

Root mean square roughness is lower for hybrids with augmented siliceous domains (10 wt% BTESE) suggesting a cleaner fracture.

For the A-4.5 fracture surface, prominent ovaloid domains and to a lesser extent irregular micron scale domains are seen in Figure 3.6. The ovaloid features have a dark appearance signaling an overall lower modulus.[40] In between the ovaloid domains is a lighter (higher modulus) matrix that is continuous. The degree to which micron scale ovaloid domains are prominent is in the order A-4.5 > A-1.1 > B-4.5. B-1.1 has a morphology that is devoid of micron scale features. At the micron scale, we propose that the dark color of the ovaloid domains reflects the lower modulus of a largely physically phase separated domain, whereas the lighter color of the surrounding domain is associated with higher siliceous content associated with the chemical crosslinking via hydrolysis / condensation cure.

The ovaloids on the fracture surface logically arise from the fracture of three dimensional microscale domains. An idealized model is shown in Figure 3.7 based on the notion that PDMS / 3F / hard block phase separation forms a physical network during solvent evaporation. The physical network is formed via hydrogen bonding and is favored for A-4.5 due to relatively high 3F molecular weight and low concentration of $–Si(OEt)_3$ chain ends.

An enlarged version of the phase image for A-4.5 is provided as Figure S3.2. Nanoscale morphological features can be discerned in the ovaloid domains. Some are comprised of parallel light and dark nanolayers attributed to formation of associated PDMS and 3F blocks forming ABA domains depicted in Figure 3.7. The roughly parallel arrays of ABA constituents are proposed based on the mutual immiscibility of PDMS, 3F, and the hard block.

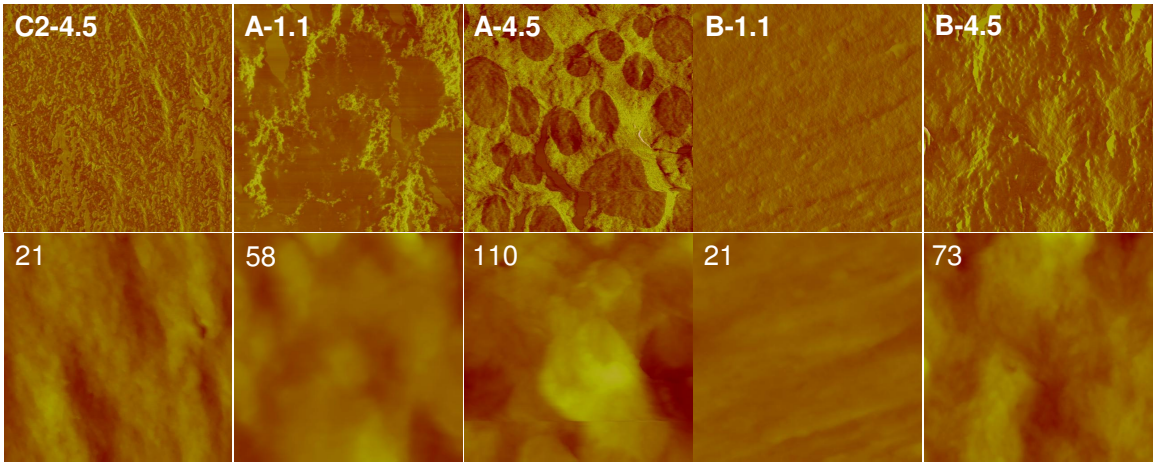

Figure 3.6. TM-AFM phase images of fracture surfaces at r_{sp} = 0.95, scan size = 10 µm and 2 µm , z = 60º.

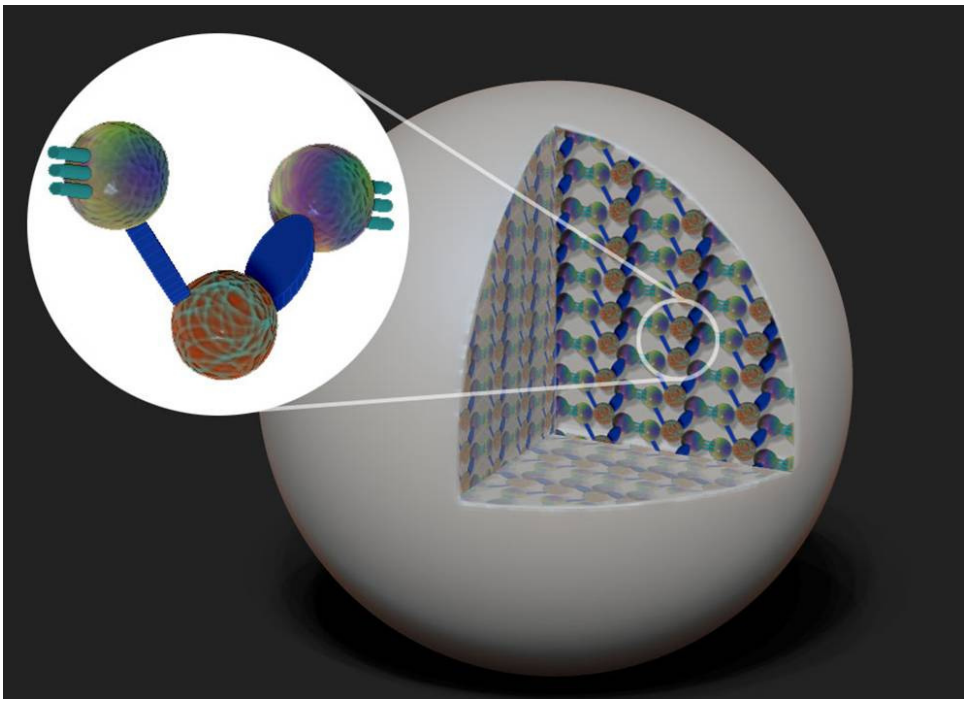

Figure 3.7. A model depicting a phase separated A-4.5 microdomain (Ovaloid feature).

This mutual immiscibility is known from prior studies of PDMS polyurethane ureas[55,87,88] and from studies of fluorous / PDMS systems.[50,65] After initial physical phase separation, chemical crosslinking within the ovaloids leads to siliceous-rich layers and accounts for the light (harder) nanoscale features within the overall darker (softer) micron scale phase image.

Ovaloid micron scale domains become less distinguishable in phase images with increasing wt% $SiO_{1.5}$ (Table 3.3), namely A-4.5 (1.8) > A-1.1 (2.2) > B-4.5 (5.4) >> B-1.1 (5.8). This correlation is consistent with slower chemical network formation via hydrolysis / condensation of -$Si(OEt)_3$ moieties, which depends on -$Si(OEt)_3$ concentration, compared to faster physical phase separation via hydrogen bonding. Following this reasoning, morphological images suggest Si-O-Si network formation interferes with triblock physical phase separation that forms ovaloid and related structures. Neither micron nor nanoscale features are resolvable for the B-1.1 fracture surface (Figure 3.6). In contrast to A-1.1, B-1.1 morphology is attributed to relatively high -$Si(OEt)_3$ concentration.

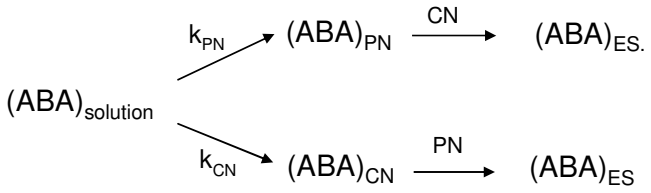

Scheme 3.3. Kinetics of physical vs. chemical network formation during the coating process. Notation: PN = physical network via hard block hydrogen bonding; CN = covalently bonded network formed by Si-O-Si bonds;and ES = elastomeric solid.

The competition between physical network formation (PN) and covalent network formation by hydrolysis / condensation cure is represented in Scheme 3.3. If the rate for PN formation, k_{PN}, is greater than k_{CN} for hydrolysis / condensation, physical network formation will occur first during coating development (Figure 3.6, A-4.5).

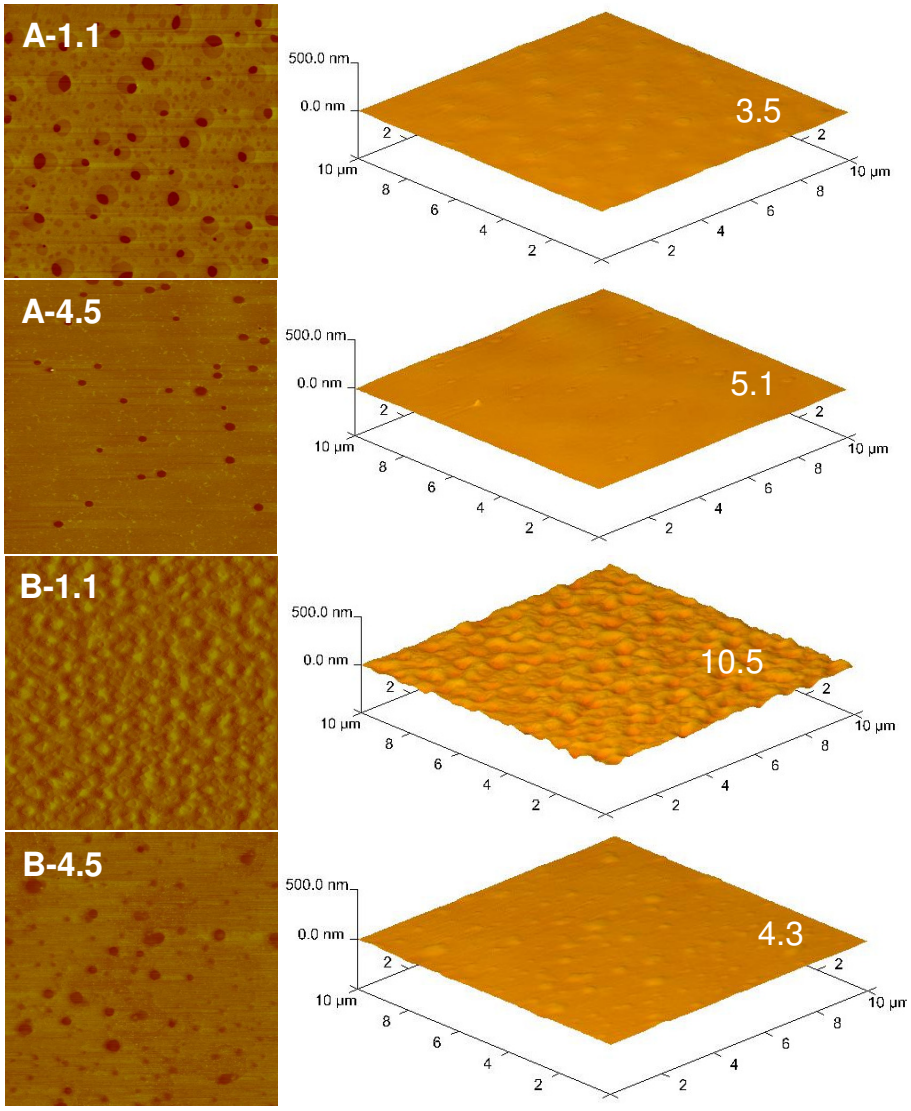

Figure 3.8. Phase and 3D height images for the different triblock compositions by TM-AFM at r_{sp} = 0.9, scan size = 10 µm x 10 µm, z (phase) = 60°, z (height) = 500 nm. The Rq values (nm) are shown in 3D height images.

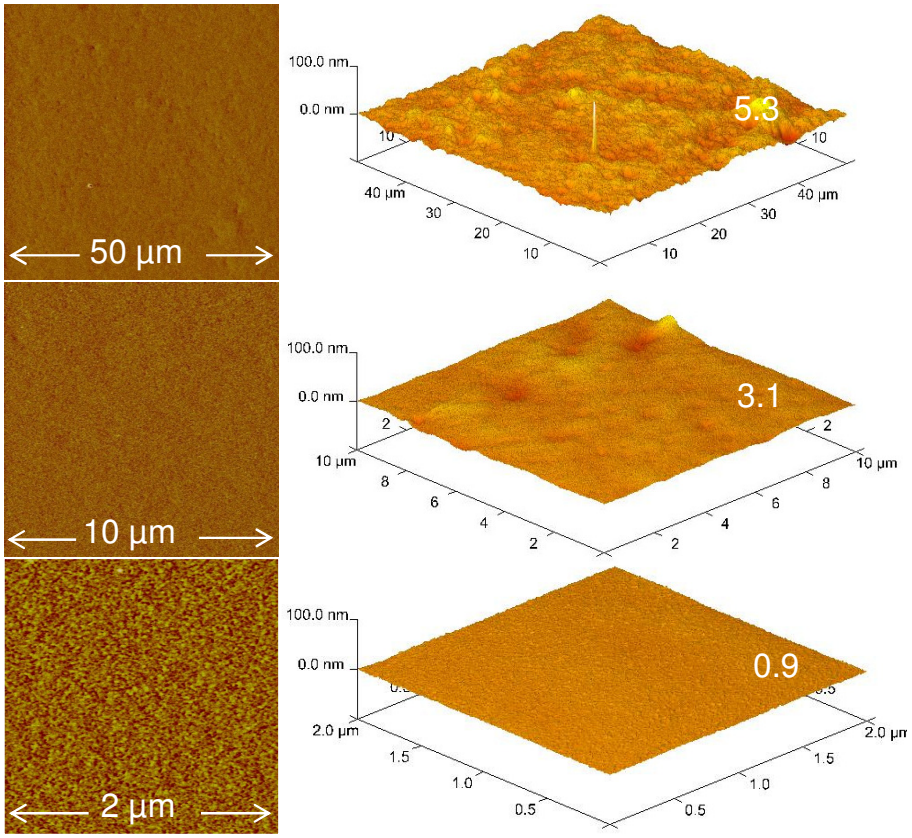

Figure 3.9. TM-AFM phase and 3D Height images for C2-4.5 at rsp = 0.8, z (height) = 250 nm, z (phase) = 60°, for different scan sizes. The Rq values (nm) are reported in the right hand corner of the 3D height images.

Conversely, if k_{CN} is rapid due to high -$Si(OEt)_3$ concentration and low 3F molecular weight morphological features are not apparent by TM-AFM (Figure 3.6, B-1.1).

For control C1 at $r_{sp} = 0.9$, the phase images are featureless at scan sizes of 10 μm and 2 μm (Figure S3.3). The lack of nanoscale features correlates with the absence of HMDI urethane / urea hard block and minimal physical crosslinking due to the small (2.3 wt%) urea content. Surface morphological features observed for the triblock compositions (Figures 3.8 and S3.4) can be mostly attributed to solvent evaporation and shrinkage occurring from condensation reactions. Consistent with previous studies,[38] there is no TM-AFM evidence for siliceous domain content at 8.3 wt% $SiO_{1.5}$ (Table 3.3).

C2-4.5 is comprised of a 3F soft block and an HMDI urea-urethane hard block (10 wt%) terminated with $–Si(OC_2H_5)_3$. For C2-4.5, the complex phase image is comprised of light (higher modulus) micron-scale features interspersed with the higher modulus domains are dark colored (lower modulus) regions. While the origin of this complex solid state morphology is obscure, there are no ovaloid structures characteristics of A-1.1, A-4.5, and B-4.5 hybrid triblocks.

Also, while the C2-4.5 fracture surface has curvilinear morphological features than span micron- to nano-scale, the phase image for the as-cast surface is virtually featureless at the same imaging conditions (*vide infra*, Figure S3.5.). Imaging the surface at a lower setpoint ratio discussed below (Figure 3.9) reveals a plethora of nanoscale features.

3.4.5. Tensile Properties. Stress strain characteristics for PDMS-3F-PDMS hybrid elastomers and controls are shown in Figure 3.10. Table 3.2 lists modulus and strain at break. Low moduli reflect high soft block content and low glass transition temperatures for PDMS and 3F soft blocks. The initial stress-strain curves from which tensile moduli are determined are similar for A-1.1, B-1.1, B-4.5, and C2-4.5 (2.1-2.2 MPa, Figure 3.10 and Table 3.2).

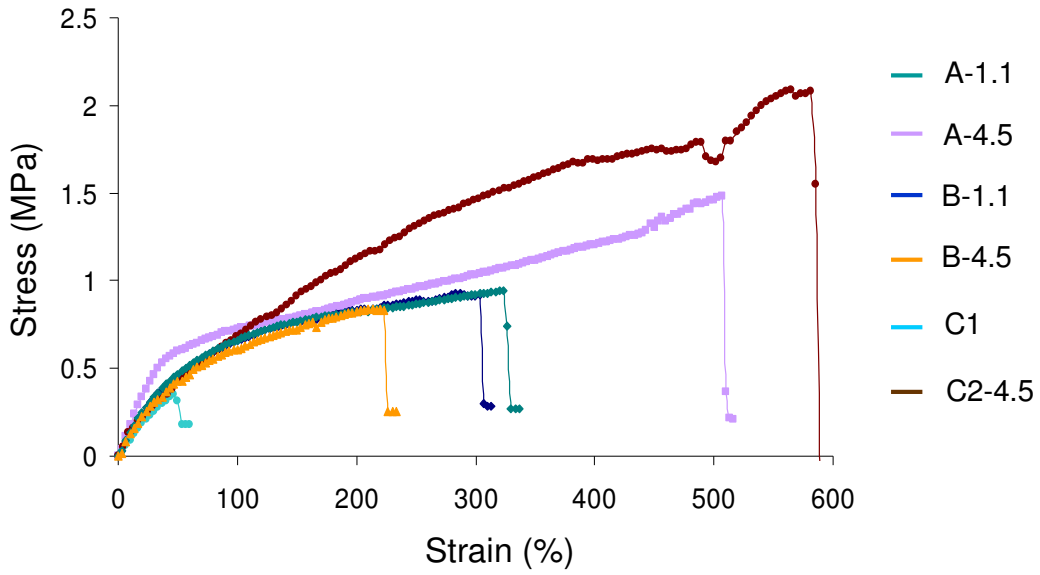

Figure 3.10. Stress-strain curves for the triblock elastomers, controls C1 and C2-4.5.

The unique stress-strain curve for A-4.5 reflects a higher initial modulus (2.3 MPa). The higher initial modulus for A-4.5 is attributed to good microscale phase separation discussed above (TM-AFM, Figure 3.6).

Figure 3.11 provides a correlation of hard block wt% with strain at break. The order of strain to break (%) is A-4.5 (492) > A-1.1 (328) ≈ B-1.1 (315) > B-4.5 (26). With a lower hard block weight percent (3.1) than A-1.1 (4.5), A-4.5 has a significantly higher strain at break 492% (Figures 3.10 and 3.11). The strain at break for A-4.5 is exceeded only by control C2-4.5 (580%), which has 3.6 wt% urethane/urea but 10 wt% hard block (Table 3.3). The better strain at break for A-4.5 is again attributed to superior phase separation (TM-AFM), strong hydrogen bonding (Figure 3.4A), higher extensibility facilitated by the higher 3F-4.5 molecular weight and minimized siliceous content.

For a comparison of mechanical properties one can consider HMDI/ED-PDMS polyurethane ureas (ED = ethylene diamine).[87] These polyurethanes had relatively high hard segment weight percents (25 to 30 wt%). Maximum strain at break was ~400%. The relatively high wt% hard block accounts for the much higher modulus compared to the hybrid triblocks. Increased siliceous domain content with BTESE decreases strain at break from 492% for A-4.5 to 260% for B-4.5. This observation is correlated with the weaker and broader H-bonded carbonyl absorption for B-4.5 compared to A-4.5. The low frequency C=O absorption for A-4.5 indicates strong hydrogen bonding (similar to control C2-4.5), while the weak and broadened peak for B-4.5 reflects weaker C=O hydrogen bonding to Si-OH (Figure 3.4B) and concomitant disruption of strong urea/urethane hydrogen bonding. The lower strain at break and weaker hydrogen bonding for B-4.5 is attributed to disruption of hard block phase separation (decreased k_{PN}; increased k_{CN}) and network constrained phase separation.

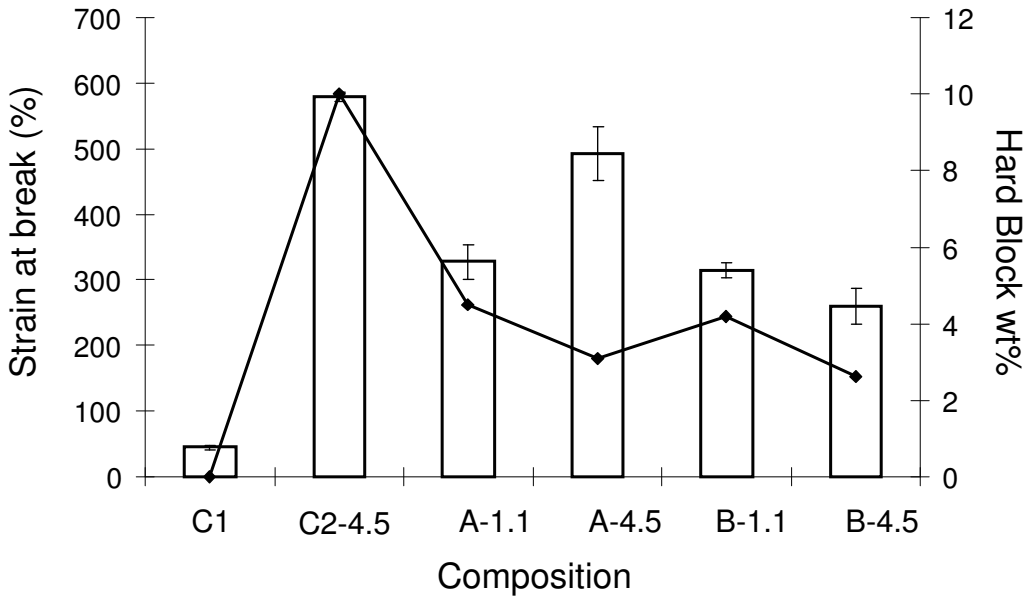

Figure 3.11. Abscissa: control and hybrid designations; Left ordinate, average strain to break; right ordinate, wt% urea/urethane (C1) or hard block.

Without HMDI, control C1 has weak mechanicals with a very low modulus (0.9 MPa) and strain to break of 40%. Qualitatively, this observation correlates with negligible low frequency H-bonded carbonyl absorption (Figure 3.5).

Yilgor, McGrath and Wilkes have shown that enhanced urea H-bonding results in good mechanicals and phase separation for polyurethanes and polyurethane-ureas.[56,58,87] TDI(MDI)/H_2O/PTMO polyurethane-urea elastomers with a hard segment (HS) ranging from 20-35 %, were studied for surface and bulk morphology.[56]

It was observed that these elastomers have superior tensile properties with a maximum strain at break ranging from 500 to 1200 % (26 - 33 % HS). Observed results illustrate enhanced mechanical strength from hydrogen bonding of the hard block segments (C=O and N-H moieties). The A-4.5, having only 3 % HS demonstrates excellent tensile property, which can thus be attributed to phase separation favored hydrogen bonding of the hard block domains.

3.4.6. Phase transitions and morphology. Dynamic mechanical testing is often the method of choice for determining phase transition temperatures for elastomers. Compared to DSC, amplified sensitivity is usually obtained for the change from the glassy to rubbery state at T_g.[89,90]

Tan δ versus temperature for PDMS-3F-PDMS elastomers is shown in Figure 3.12. Compositions A-1.1, A-4.5 and B-4.5 have similar thermomechanical behavior, with a loss peak at -115 °C due to PDMS T_g and one centered at -35 °C for the 3F block T_g. The clear separation of loss peaks for A-1.1, A-4.5, and B-4.5 is typical for phase separated soft blocks.[91,92] A DMA study on PDMS-PTMO polyurethanes having 33 to 37 wt% MDI-BD hard segments had separate T_gs for PDMS (-111 to -120 °C) and PTMO (-40 °C).[93]

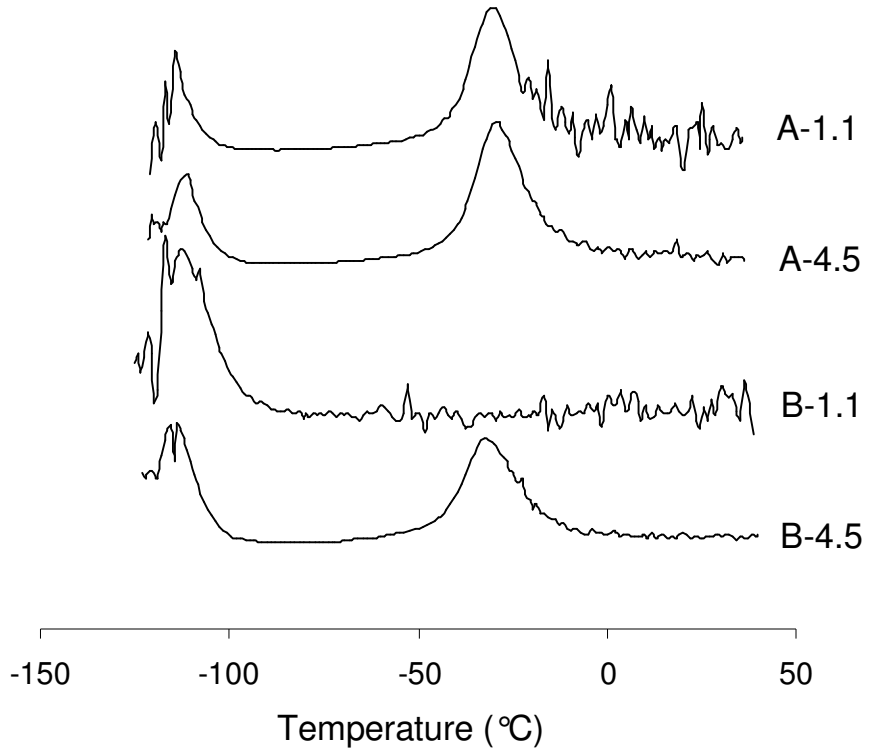

Figure 3.12. Dynamic mechanical analysis: tan delta for triblocks vs. temperature.

Storage modulus (E') versus temperature for hybrid triblocks is shown in Figure 3.13. For A-1.1 and A-4.5 a one hundred fold drop in storage modulus occurs from just above PDMS T_g (-90 ºC, E', 200-210 MPa) to 0 ºC (E', 1.7-2 MPa), which is above the 3F T_g. Although the phase image for A-1.1 microscale phase separation is less distinct compared to A-4.5, at the small deformations used in DMA (~ 0.05 %) the physical network resulting from hard block phase separation gives rise to a clear drop in storage modulus for A-1.1 at 3F T_g. For B-4.5 intermediate behavior is observed. That is, the storage modulus at -90 °C is 90 MPa, about half that for A-4.5. However, storage moduli that are similar to A-4.5 are found at 0 and 150 °C. Thus, network constrained phase separation, resulting in barely discernable micron-scale ovaloids in TM-AFM (Figure 3.6), has decreased low temperature modulus. However, the smaller scale of hard block phase separation has not much affected higher temperature performance.

In contrast to A-1.1, A-4.5 and B-4.5, a 3F T_g is not detected for B-1.1 by DMA (Figures 3.12 and 3.13). However, a PDMS T_g is observed at -115 °C. Above the PDMS T_g little change is seen in tan δ while a gradual decrease in the storage modulus (8 to 1.4 MPa) occurs from -90 to 150 °C. The retention of change in modulus E' and loss peak for PDMS with the absence of corresponding peaks for the 3F soft block domain was unexpected so that relevant prior work is briefly considered to place this observation in perspective.

Conventionally, copolymers comprised of immiscible blocks form amorphous domains with separate T_gs.[91, 92, 94] However, when the scale of phase separation is reduced to a few tens of nanometers, separate T_gs may not be observed.

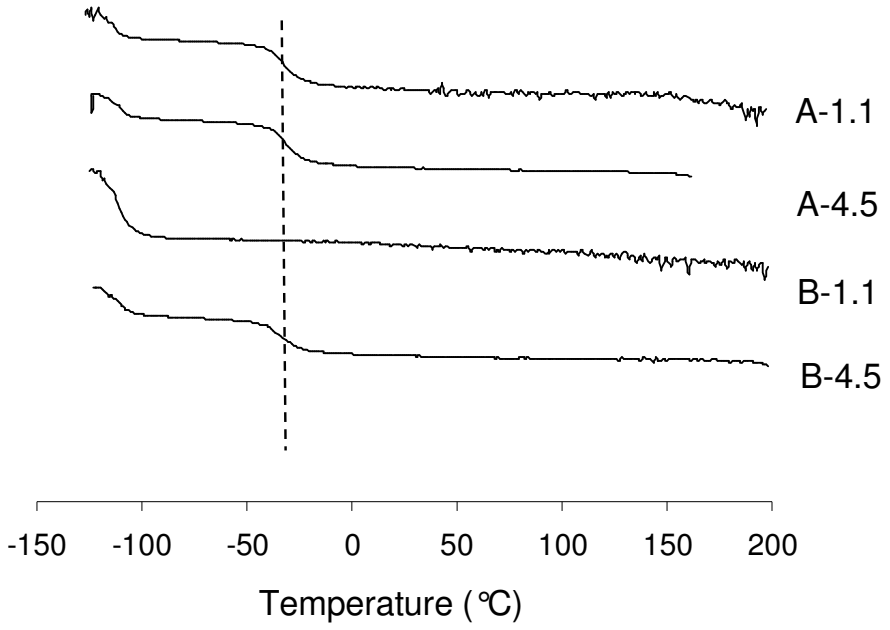

Figure 3.13. DMA: storage modulus (E') versus temperature for triblock elastomers. Dashed line is for guiding the eye.

Baer reported layer-multiplied co-extrusion of high MW polycarbonate (PC, 62 kDa) and poly(methyl methacrylate) (PMMA, 132 kDa) sheets.[95,96] When the interfacial separation of PC and PMMA layers was ~10 nm (discernable by AFM) only one broad change in slope (T_g) was observed via DSC. When sheets of semicrystalline polyethylene oxide (PEO, 200 kDa) and polystyrene (PS) were subjected to "forced assembly" by multiple co-extrusions, the DMA β-relaxation peak (T_g) for PEO was greatly reduced in intensity, reaching a minimum at a PEO layer thickness of 120 nm.[97]

Better known or at least more intuitive is the effect of increasing molecular weight on glass transition temperatures for low molecular weight fluorous / aliphatic systems. For perfluoropolyether (PFPE) and PEG blocks with very low molecular weights, photo-generated networks had microscale miscibility (optical transparency) but nanoscale phase separation (AFM).[98] Separate T_g's were not observed in DSC for combinations of low molecular weight PFPE and lowest weight fraction PEG but two T_g's and optical opacity were observed for other compositions and for networks derived from higher molecular weight components.

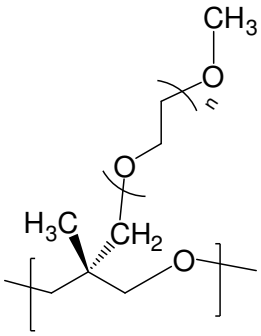

We have recently reported a mixed soft block polyurethane comprised of P(3F) and P(ME3Ox) soft blocks.[99] Separate T_g's were observed by DSC at -47 °C (ME3) and -34 °C (3F). Only one broad T_g at -38 °C was observed for a polyurethane with a block 3F-*b*-ME3n soft block (3F-*b*-ME3n-U). Nanoscale phase separation (25 - 100 nm domains) was seen by TM-AFM for a base polyurethane modified with 2 wt% 3F-*b*-ME3n-U. For the random soft block polyurethane analog, 3F-*r*-MEn-U one T_g was also found by DSC. Nanoscale phase separation could not be discerned by TM-AFM imaging for 2wt% 3F-*r*-ME3n-U.

From the above, it is apparent that fluorous / aliphatic polymer blends and low molecular weight networks, even with relatively low molecular weights, can be phase separated at the nanoscale without observation of separate T_g's for the respective domains. Thus, the absence of discernable nanoscale phase separation for B-1 (Figure 3.6) provides another example where reducing phase separation to a few tens of nanometers results in the absence of a detectable T_g. The compositional contributors to this unique observation for B-1.1 include network constrained phase separation ($k_{CN} > k_{PN}$) driven by BTESE as well as low 3F molecular weight.

The absence of a detectable T_g for one soft block domain (3F) with the retention of the phase transition for a second domain (PDMS) may be understood considering the low 8.9 wt% 3F in B-1.1 (Table 3.1) while the PDMS wt% is 80.6. Thus, 3F is apparently incorporated in an "interphase".[95,96]

Network constrained phase separation ($k_{CN} > k_{PN}$) results in B-1.1 having a low storage modulus at -90 °C (8 MPa). The absence of a separate T_g for 3F results in a gradual decrease in storage modulus (8 to 1.4 MPa) from -90 to 150 °C. Considering the 4.2 wt% hard block, the relatively flat storage modulus from -90 to 200 °C is noteworthy (Figure 3.13). The constraint of hard block physical crosslinking is tempered by higher hard block wt% for B-1.1 (4.2) compared to B-4.5 (2.6). The result is a higher strain to break for B-1.1 (Figures 3.10 and 3.11).

Thermal transitions were determined by MDSC (-70 to 200 °C) at a heating rate of 10 °C /min (Figure S3.6). The T_g for 3F diol is -51 °C.[100] The change in heat capacity for the PDMS-3F-PDMS elastomers at the 3F T_g was small (~ 0.0009 W g^{-1} $°C^{-1}$) and broad resulting in poor accuracy for T_g determination. The presence of a higher temperature thermal transition (~ 120-150 °C) may be due to the hard block T_g. The low wt% hard block with concomitant small changes in heat capacity make assignments tentative.

3.4.7. X-ray Photoelectron Spectroscopy. Atom percentages of F, O, C, N and Si were obtained from XPS at a 90° take off angle listed in Table 3.4. All compositions have a high at% Si atom at the surface which comes mostly from PDMS. The atom % Si ranges from 23.5% for B-1.1 to 27.2% for composition A-1.1.

These triblocks also show a relatively high concentration of N at the surface with coating B-1.1 having a highest of 2.4%. Coatings B-1.1 and B-4.5 have shown trace amounts of F at the surface from XPS whereas for A-1.1 and A-4.5 no trace of F is observed. This phenomenon can be attributed to the fact that the presence of a molecular crosslinking agent increases the rate of condensation cure, preventing the fluorous moieties from phase separating and aggregating in the bulk. From the observed XPS results, it can be postulated that the 3F diol **1** remains in the bulk of the hybrid matrix.

The atom% Si in PDMS is calculated to be 25%. From table 3.4, it can be observed that the atom% Si ranges from 23.5% to 27.2%, which suggests that the PDMS segment of the hybrid network concentrates at the surface of the films. The calculated Si/O ratio equals '1' in the PDMS chain and the observed ratio ranges from 1.04 to 1.19 which reconfirms the surface concentration of PDMS chains in the triblock system.

3.4.8. Dynamic Contact Angle. DCA measurements were done to analyze the surface wetting characteristics of the crosslinked polymeric coatings. To determine hydrophobicity of the coated surfaces, water was used as the probe liquid. Surface tension of water was tested with a flamed glass slide before and after running each sample. Completely overlapping force-distance curves demonstrated the fact that there were no leachable components from the coating and the surface tension of water remained unaltered after running a coated slide (no water contamination).

Table 3.4. XPS showing the atom percents for different triblock compositions.

Designation	Observed (Atom %)					
	N	C	O	Si	F	Si/O
A-1.1	1.3	48.9	22.6	27.2	-	1.19
A-4.5	1.3	49.8	22.5	26.4	-	1.17
B-1.1	2.4	50.1	22.4	23.5	1.6	1.04
B-4.5	1.5	50.3	22.6	24.6	0.95	1.09

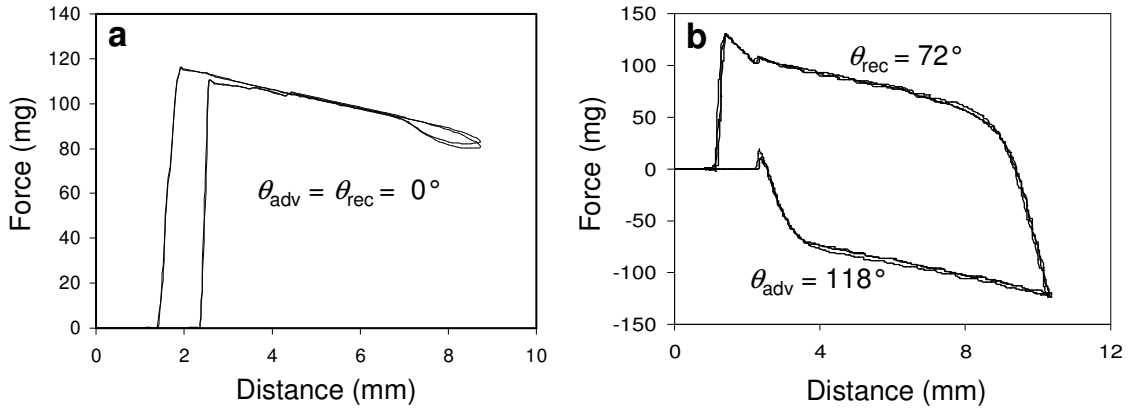

Figure 3.14. DCA force distance curves (two cycles) for A-4.5: (a) isopropanol; (b) water.

A conventional condensation cured PDMS coating gives an advancing contact angle of 115 and a receding contact angle of 75 with water. For all triblock compositions, advancing contact angles between 109° to 118° and receding contact angles between 72° to 77° are observed with water (Figure S3.8).

These advancing and receding contact angles are typical for a PDMS dominated surface and suggests that these compositions have a surface that is predominantly concentrated with PDMS. Such high contact angles are also obtained for a fluorinated surface and hence further investigation with a probe liquid was required that would be able to differentiate between a fluorinated and a PDMS-like surface.

From a prior study done on block copolymers having dimethylsiloxane and semifluorinated styrene blocks[65] has shown that isopropanol perfectly wets a PDMS surface whereas it gives a contact angle hysteresis for a surface dominated by fluorine. Wetting behavior of these coatings was studied with isopropanol as the probe liquid. It was observed that for all of these compositions, isopropanol perfectly wets the surface, i.e., it gives a zero advancing and receding contact angle (Figure 3.14). Hence, wetting behavior reiterates the fact that the silicone domain concentrates at the surface of these triblock copolymers.

3.5. Conclusion

The reaction scheme for this class of copolyoxetane offers a wide scope for preparation of triblock copolymers since many macrodiols are candidates. Considering the low hard block content (3-4 wt%), the hybrid elastomers have very good mechanical strength. This result is attributed to immiscible soft block domains driving urea-urea and urea-urethane H-bonding between hard block domains. The hybrid elastomers retain rubbery behavior over a wide

temperature range (-20 to 150 °C). The B-1.1 composition has a particularly wide plateau modulus from -90 to 150 °C. Hybrid triblock urethane-urea elastomeric coatings having fluorinated and silicone moieties provide interesting opportunities for exploring applications such as biocompatible materials and anti-adhesive or foul release materials.

3.6. Supporting Information.

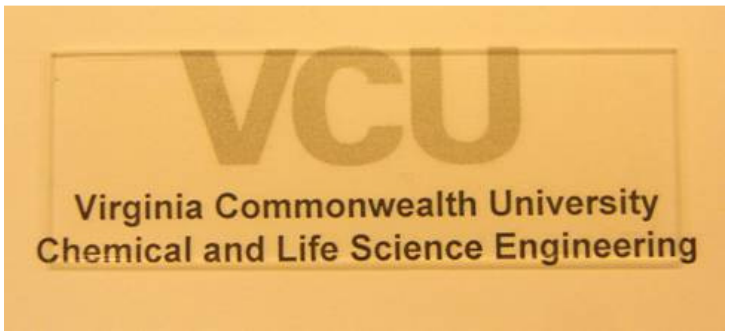

Figure S3.1. A-4.5 coating image demonstrating optical transparency.

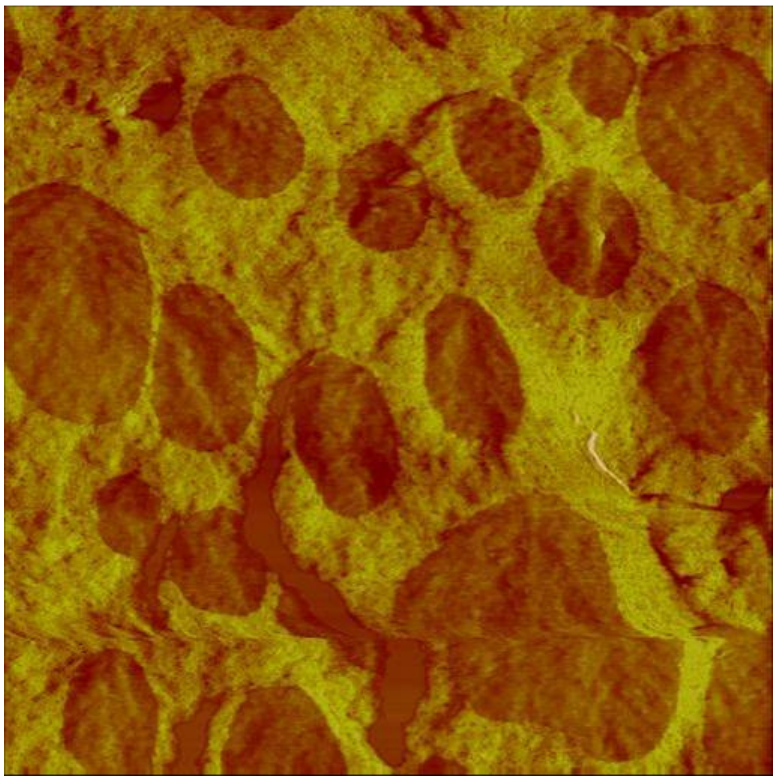

Figure S3.2. A magnified phase image of A-4.5 showing different phase separated ovaloid features.

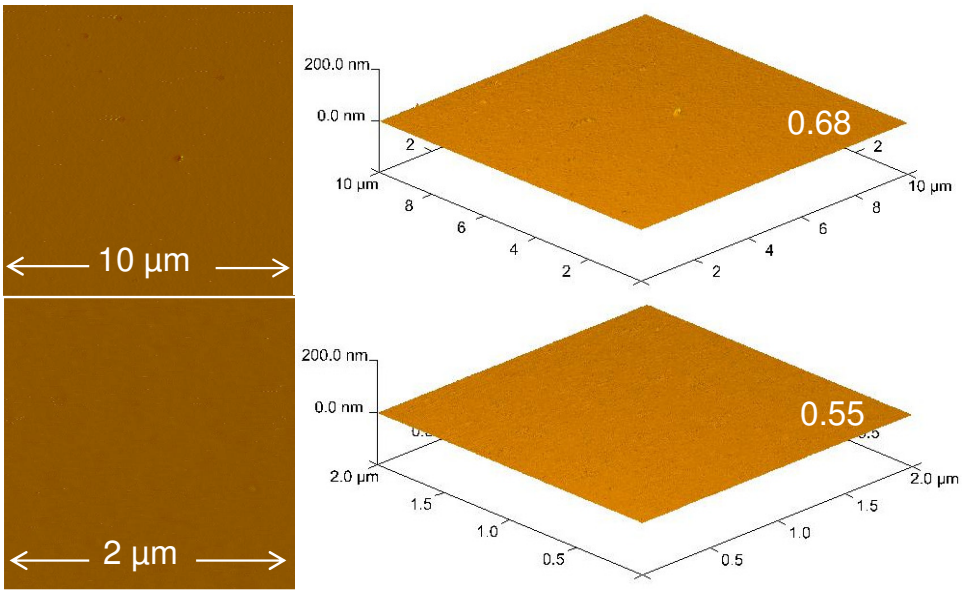

Figure S3.3. 3D Height and phase images of control C1 by TM-AFM at rsp = 0.9, z (height) = 200 nm, z (phase) = 60°, for different scan sizes. The Rq values (nm) are reported in the right hand corner of the 3D height images.

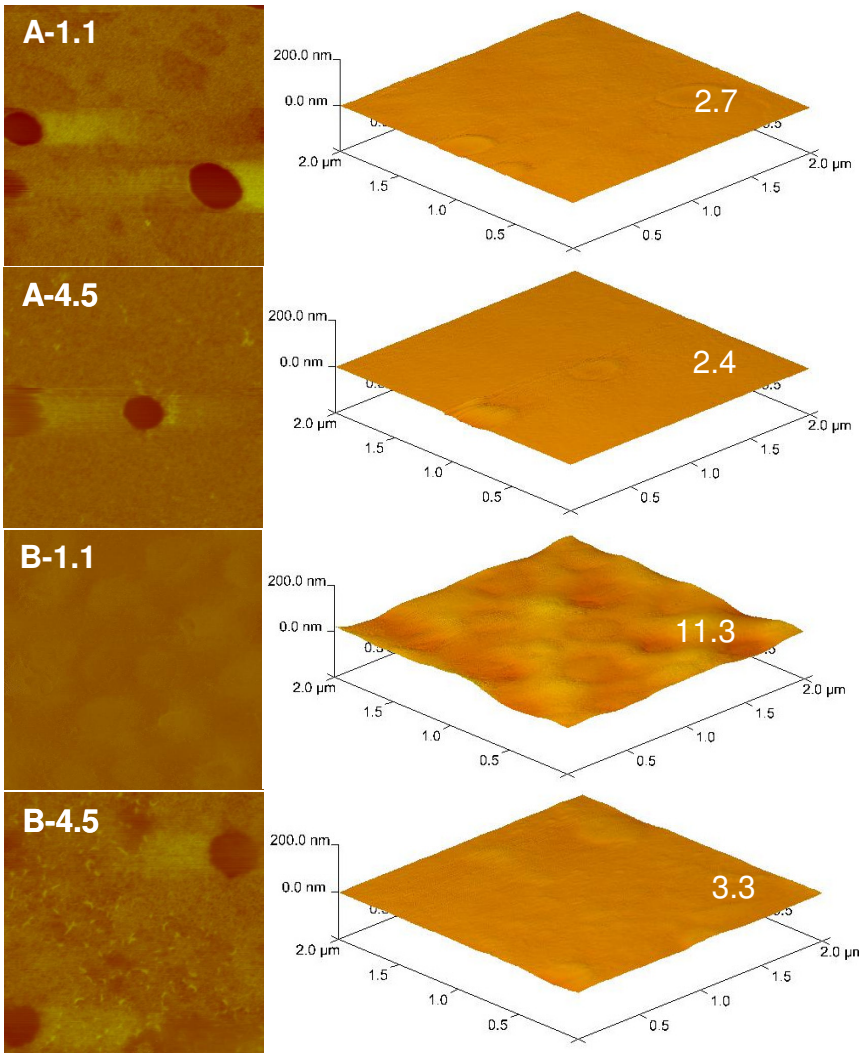

Figure S3.4. Phase and 3D height images for the different triblock compositions by TM-AFM at r*sp* = 0.9, scan size = 2 µm x 2 µm, z (phase) = 60°, z (height) = 200 nm. The Rq values (nm) are reported in the right hand corner of the 3D height images.

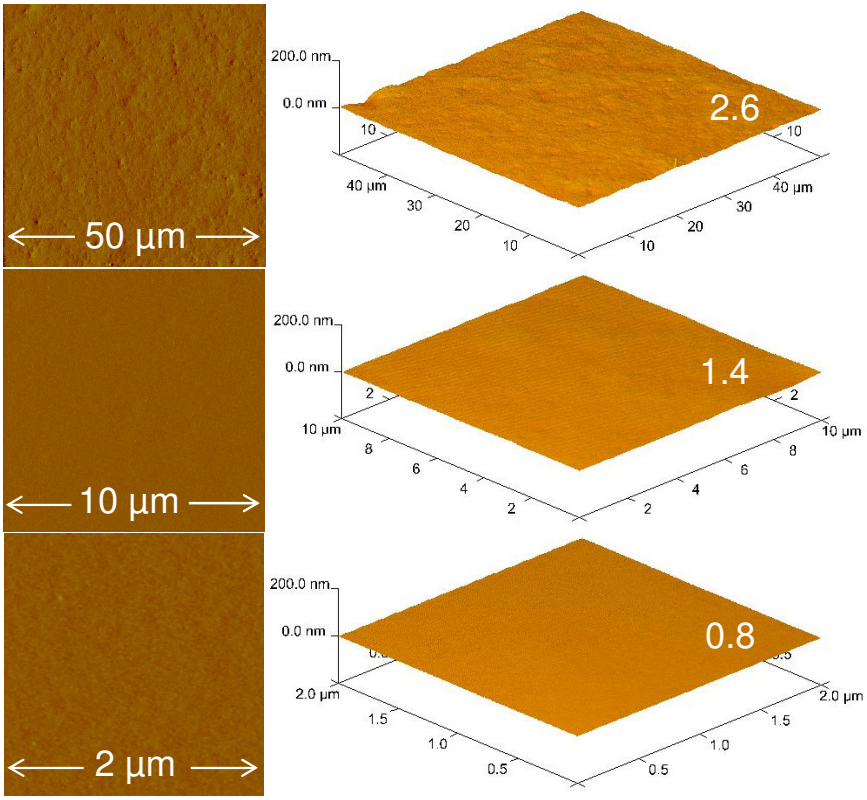

Figure S3.5. Phase and 3D height images of control C2-4.5 by TM-AFM at rsp = 0.9, z (height) = 200 nm, z (phase) = 60°, for different scan sizes. The Rq values (nm) are reported in the right hand corner of the 3D height images.

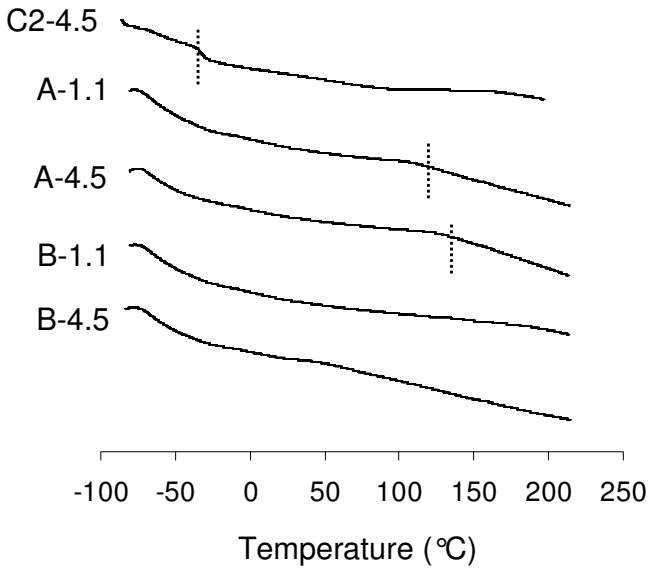

Figure S3.6. MDSC for the triblock elastomers and the control, C2-4.5

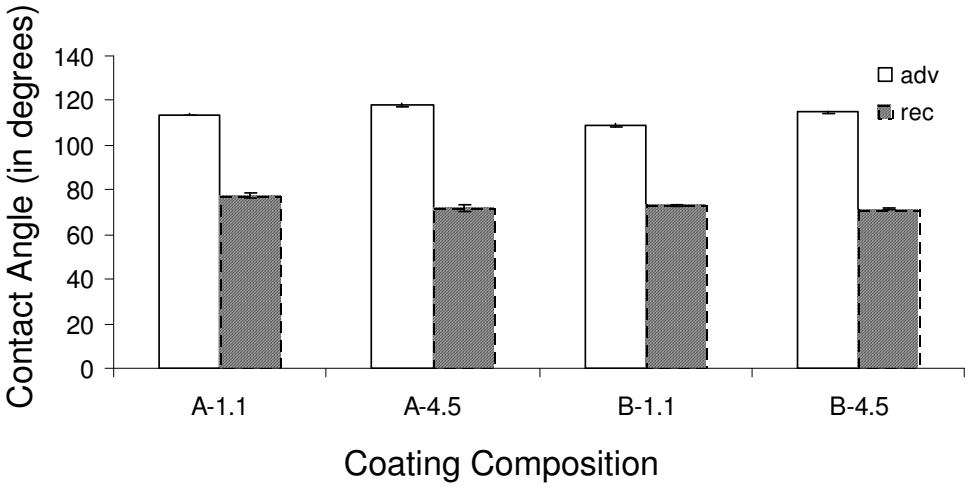

Figure S3.7. Advancing and receding contact angles by DCA with water.

CHAPTER 4

Urethane-Urea triblock copolymers as effective *foul-release* coatings.

4.1. Introduction.

Marine biological fouling or *biofouling* is defined as the accumulation of undesired microorganisms, plants and animals on an artificial surface immersed in sea water.[101] Biofouling is inevitable in marine environments.[102,103] Temperature, salinity and presence of micronutrients in the aquatic environment affect the nature and number of adhering fouling organisms,[104] varying from soft fouling organisms like tunicates, algae, slimes, diatoms and hydroides to hard fouling species including barnacles, bryozoans, cyprids and mussels. These fouling organisms employ compositionally different adhesives for attachment to any given substrate. One of the most common biofouling species are barnacles, attaching to a given substrate with the help of hydrophobic proteins via cysteine linkages.[104]

The most common phenomenon of fouling in the marine environment is biological settlement on ship hulls leading to adverse consequences. Past studies have shown that biofouling of marine vessels lead to an enhanced surface roughness, resulting in increased frictional resistance and hydrodynamic drag.[102,103] The generated surface roughness has a negative impact on the speed and power of a ship, increasing fuel consumption which ultimately translates to an unfavorable economic impact.[105] Intuitively, heavily fouled surfaces entail frequent cleaning, resulting in a waste of time and resources and also generating large amounts of toxic by-products.[106] Biofouling leads to coating deterioration, causing corrosion,

discoloration and an alteration in the electrical conductivity of the material.[107] Biological fouling truly is one of the menacing challenges faced by marine vessels in the present day.[108]

In the past, marine fouling was prevented by the release of toxins from metal containing paints applied on ship hulls.[109] Several efforts have been made over the past few decades to develop materials with reduced toxicity which when applied as coatings on the surface of marine vessels would minimize the problem of biofouling.[102,110] One of the most promising antifouling coating has been paints containing metals like copper, mercury, arsenic and cadmium.[101,104] Studies revealed these metal based coatings to be highly toxic towards fouling organisms but above a certain concentration (> 2 µg/l), they are even harmful towards non-fouling organisms.[111] Due to this lack of selectivity, metal based paints containing mercury, arsenic and cadmium have become obsolete.[104]

Tributyltin (TBT) containing paints have been quite successful as an antifouling coating, preventing the attachment of barnacles and slimes on marine vessels. As coatings, the TBT based paints have found application in over 70% of the present world fleet.[101,112] On the contrary, studies have shown TBT containing compounds to be immunotoxicant towards mammals. These compounds affect the phagocytic activity of marine invertebrates, reducing their resistance towards pathogenic microorganisms. Hence, the accumulation of TBT containing compounds is undesirable in marine organisms which would also affect other species in the food chain.[113]

Another antifouling coating that has being used recently is a copper based paint containing cuprous oxide and a leachable biocide. These paints achieve antifouling activity by a gradual leaching of biocides to the surrounding the marine environment. The lack of specificity towards target organisms and inconsistent results with copper based paints led to a continued interest for non-ablative, non-toxic fouling resistant coatings.[111, 113]

30 years ago, the pioneering patent of Milne introduced a non-toxic, foul release coating such as Intersleek.[114] This approach focused on generating fouling resistant coatings that precluded any chances of water contamination by leachable toxicants. For non-toxic coatings, fouling release might depend on certain factors like surface energy,[115,116] coating modulus,[117,118] frictional slippage[119] and coating thickness.[120] The basic idea behind these fouling release surfaces is to produce a coating that would lead to a very weak adherence / easy release of fouling organisms. It has been postulated that a flexible polymer backbone with side chains having negligible intermolecular interactions is the best candidate for fouling release applications.[121] From previous studies it has been observed that silicone based polymers and those containing fluorinated moieties are better candidates as fouling release coatings due to their low modulus, low surface tension and low surface energy.[122] Based on the above properties, silicones generate very weak adhesive forces of interaction between the substrate and the marine organism, outperforming fluoropolymers in this aspect.[117] Several non-toxic silicones have been developed as fouling release coatings which have the capability of self cleanin.[121] Weak mechanical strength of silicones still remain an intriguing problem and a combination of low surface energy with strong mechanical property would be ideal for an efficient fouling release coating.

As mentioned in the previous chapter, a prior study has focused on the synthesis and characterization of a segmented triblock copolymer system comprising of three mutually immiscible components, namely, a fluoropolymer **1**, a diisocyanate hard domain **2** and a silicone soft block **3**. These triblock copolymers were generated by condensation cure, leading to the formation of a siliceous phase in the system. The effect of having an additional siliceous phase in

the copolymer was investigated by adding a calculated amount of siliceous crosslinking agent **4**. The structure of the reactants has been shown in figure 4.1.

The coatings described in this present study are referred to as A-1.1, A-4.5, B-1.1 and B-4.5, where the acronyms represent the respective compositions, elucidated in the previous chapter. A typical acronym A represents (3F-1.1)H/(Si-4.5)(BTSE-0), where, '3F' refers to the 3F diol **1**, having a trifluorinated moiety in the side chain and '1.1' stands for its molecular weight from GPC, i.e., 1.1 kDa. 'H' denotes the diisocyanate **2**, i.e. HMDI which has been used in this study. 'Si-4.5' refers to a 4.5 kDa PDMS **3**. Bis(triethoxysilyl)ethane (BTESE) refers to the crosslinking agent and 'x' referring to the wt% of crosslinking agent used in the compositions. For A-1.1, x has a value of 0. Two controls, namely C1 and C2-4.5 have also been used in the previous study for comparison with the triblock copolymers. C1 has been prepared by a condensation reaction between **3** and 3-isocyanatopropyl triethoxysilane, thus generating a PDMS based control. C2-4.5 has been prepared by reacting **1** and **2** via a urethane reaction, followed by end capping with 3-aminopropyl triethoxysilane and condensation cure. Control C2-4.5 mimics typical crosslinked polyurethanes. Prior study has shown that these triblock copolymers having ~ 96 % soft block domains, demonstrate remarkable mechanical strength.

It is observed from XPS and wetting behavior studies that these triblock copolymers have a surface dominated by PDMS, generating a copolymer with a low surface energy and a low near surface modulus. The interesting surface and bulk morphology has led to this present study which investigates the non-adhesive characteristic of these triblock compositions for their potential application as marine fouling release coatings. A detailed synthesis and characterization of these triblock copolymers has been described in the previous chapter.

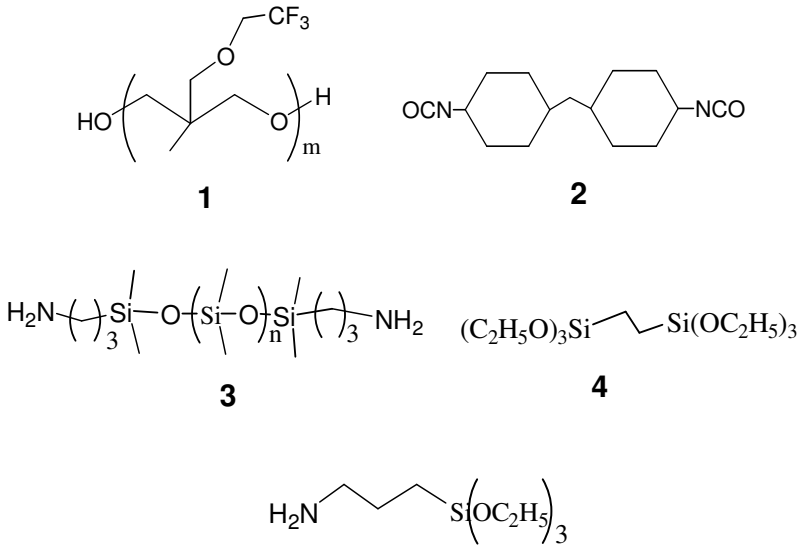

Figure 4.1 Individual reactants taking part in the synthesis of the triblock copolymers.

4.2. Experimental.

4.2.1. Release study (Laboratory scale). An experiment was designed in the laboratory to investigate the adhesive property of the triblock coated surfaces. This experiment was performed using a Dynamic Mechanical Analyser-RSA3 (TA instruments). In the test, an aluminum cylinder was used to mimic a barnacle, a marine organism that contributes to hard fouling. Microscope slides coated with a representative triblock composition were used as test substrates. The procedure involves attaching aluminum cylinders to these coated microscope slides using an epoxy mixture (Loctite Epoxy, marine, white, Henke Corporation, Rocky Hill, CT, USA). Epoxy, also known as polyepoxide, is formed by the reaction of an epoxide resin with a polyamine. The coatings were kept at ambient temperature for 24 hours to allow a firm attachment of the aluminum cylinders on the coated surface. The coated slides were fixed on a clamp in the DMA and a force probe at 0.05 mm/sec was used to remove the attached aluminum cylinders from the surface. The removal stress was measured as a function of distance the probe enhances during the process of release. The maximum stress at which the aluminum cylinder gets detached from the coated surface was measured as the *peak removal stress*. Figure 4.2 illustrates the experimental setup for the release study along with a representative removal stress vs distance plot. The total amount of energy employed in removing an attached object completely from the surface of the coated microscope slide was termed as the *removal energy* and was obtained by integrating the area under the plot shown in figure 4.2.

4.2.2. Static Immersion Test. The close proximity of peak removal stress results obtained from the laboratory scale release study, a representative triblock coating A-4.5 was chosen for the in-field, static immersion test. Marine grade aluminum panels (10.2 cm x 20.3 cm) were chosen for the test with an approximate coating thickness of 300-400 µm. Panels were cleaned thoroughly

and then coated with triblock A-4.5. A layer of primer was not applied prior to coating the panels which demonstrates good adhesion of the elastomer to the aluminum surface. The static immersion tests were carried out at the Florida Institute of Technology test site near Sebastian. All panels were caged to protect them from aquatic animals other than fouling organisms. Four replicates of the representative composition were placed back to back with two replicates facing north and two towards south. The panels were tested for removal of soft and hard fouling agents by the waterjet method. Once cleaned of soft fouling, these panels were replaced in sea water to enable settlement of hard fouling organisms.

The waterjet method involves an apparatus consisting of a SCUBA tank containing compressed air, a regulator to adjust the pressure between 0 - 1.65 MPa (0 - 240 psi), a SCUBA tank containing water, and a blow gun with a 1.6 mm (1/16 inch) diameter nozzle to apply the water jet. A representative area of biofilm, 50 x 50 mm (2x2 inches), was selected for testing. The regulator was set to 20 psi. A water jet was applied to the test area until the maximum amount of fouling that can be removed at that setting was achieved. Biofouling in the test area was reassessed. Pressure was increased by 20 psi and the entire procedure was repeated. This continued until all the fouling was removed or the maximum pressure setting was reached (240 psi).

4.3. Results and Discussion.

4.3.1. Kendall Equation - Release parameters. Over the years a lot of research has been done investigating the underlying mechanism for removal of rigid objects from a substrate.[123-128]

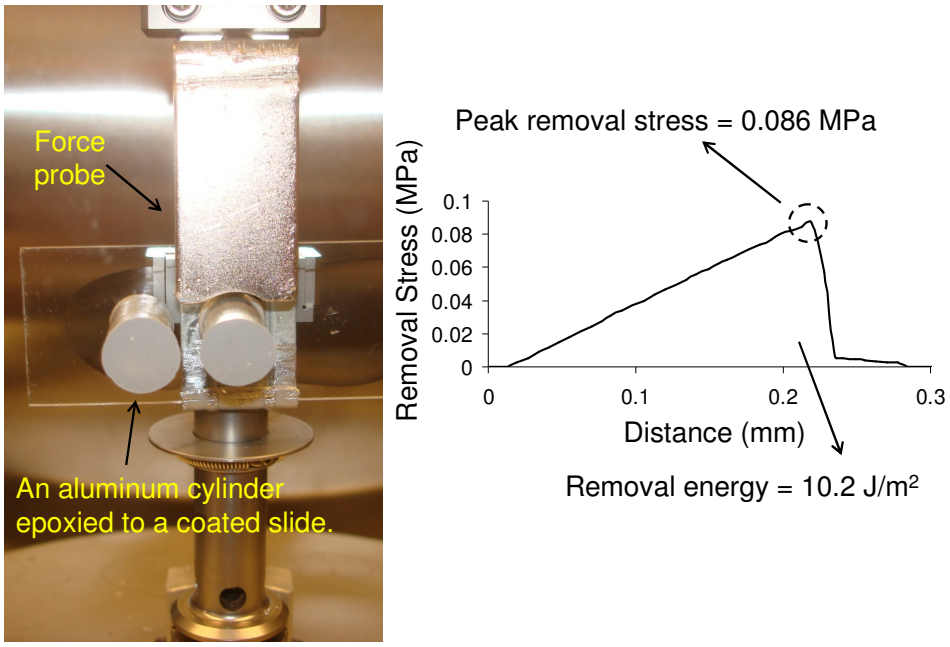

Figure 4.2. Left - abhesion test set-up, Right – removal stress vs distance curve for a sample abhesion test run.

Over 30 years ago Kendall had developed an equation (Eq 4.1) relating the bulk modulus, coating thickness and work of adhesion to the removal stress.[123] In this equation, σ denotes the critical removal stress, w_a stands for the work of adhesion, 'K' denotes the bulk tensile modulus and 't', stands for the thickness of the elastomeric coating. Studies have shown that due to low cohesive stress and elastic instability at the interface, the pull off stress is not a function of the size of the rigid object.[124,129,130] Eq 4.1 states that the pull off stress decreases with an increase in film thickness and is directly proportional to the bulk modulus and work of adhesion.[131] Previous studies have shown that the above Eq 4.1 is valid when no frictional force prevails at the film-support and the film-stud interface.[126,131]

$$\sigma \sim \left(\frac{w_a K}{t}\right)^{0.5}$$

Eq. 4.1

A qualitative idea of the dependency of each of the variables as shown in the above equation can be obtained by simple correlations. Considering the thickness of the elastomeric film and the work of adhesion to be constant, it is observed that increasing the magnitude of the bulk modulus by a factor of 2 would increase the critical pull off stress by 1.4 (Eq 4.1).[132] The term bulk modulus can be misleading at times, since in this equation the substrate is considered to be perfectly homogenous having a uniform modulus throughout all strata. Experimentally, it was observed that $CaCO_3$ filled silicones have better release characteristic as compared to their silica filled analogs,[132] where, $CaCO_3$ filled coatings have a lower surface modulus than the silica filled ones due to depletion of the filler from the near surface. Similarly, increasing the coating thickness by a factor of 2 would decrease the pull off stress by 0.7 (Eq 4.1). A comparative study done by our group between RTV11 (ethoxysiloxane cured PDMS elastomer) and a

hydrosilylation cured PDMS has shown that the critical pull of stress closely conforms to the Kendall's equation.[132]

4.3.2. Release study (laboratory scale). As mentioned earlier in the experimental section, abhesive property of the coated surfaces was tested with aluminum cylinders (10 mm in diameter) using the Dynamic Mechanical Analyser. Aluminum cylinders were epoxied to the surface of coated microscope slides, allowed to cure for 24 hrs before performing the release study. Shear force and the subsequent removal energy required for removal of the attached aluminum cylinders was measured for different triblock compositions. The PDMS control C1 and the polyurethane control C2-4.5 was also tested for their non-adhesive or abhesive surface property. Figure 4.3 shows the peak removal stress ranging from 0.091 MPa (B-4.5) to 0.11 MPa (A-4.5). C1 demonstrated the most abhesive character with a peak removal stress of 0.06 MPa, whereas, C2-4.5 had a minimum abhesive property with a peak removal stress of 0.45 MPa. The close proximity of the peak removal stresses for the triblock compositions and control C1 emphasizes the fact that these coatings have a release characteristic comparable to a silicone.

XPS and wetting behavior studies have demonstrated that the surface of these triblock coatings is dominated by the PDMS soft block domain. Hence, the low peak removal forces for the triblock copolymers can be partly explained due to a low near surface modulus and a low surface glass transition temperature (T_g).[34] Studies have shown that the presence of a surface having a low T_g hinders mechanical adhesion to the substrate. The presence of a low modulus and a low surface energy polymeric film promotes easy release of attached rigid bodies from the substrate.[131]

The energy required in removing an aluminum cylinder from the surface of the coating has been calculated from the removal stress versus distance curves. Figure 4.3 shows that the removal energy ranges from 12.8 J/m^2 for B-4.5 to 14.1 J/m^2 for A-1.1. Triblock A-4.5 has comparatively high removal energy at 28.7 J/m^2. C1 has a removal energy of 10.1 J/m^2, which is comparable to B-4.5 whereas, the polyurethane control C2-4.5 has a removal energy of 245 J/m^2. According to Eq 4.1, the removal stress is directly proportional to the bulk modulus and follows power law dependence. It has been observed that polymers with relatively high stiffness, such as urethanes, acrylates and epoxies have high adhesion strength. Similarly, in this study, a combined effect of higher surface energy and high bulk modulus of the control polyurethane translates to a very high removal stress and corresponding removal energy.

From the present data (Figure 4.3), it is observed that the urethane containing, high modulus substrate (C2-4.5) has a removal stress that is 4 times greater than the triblock compositions and a removal energy that is ~ 20 times greater than for a representative low modulus triblock coating B-4.5. As demonstrated by XPS studies in the previous chapter, the surface of these triblock copolymers is dominated by the silicone soft block. Hence, these copolymers would have a low surface energy analogous to PDMS elastomers.

4.3.3. Static Immersion test. The triblock copolymers show very good adhesion to aluminum substrate since the coatings did not show signs of peeling off from the edges even at the end of the static immersion test. Firstly, the panels were allowed to be heavily fouled with soft fouling organisms like bryozoans, barnacles, tunicates, sponges, tubeworms and biofilms.

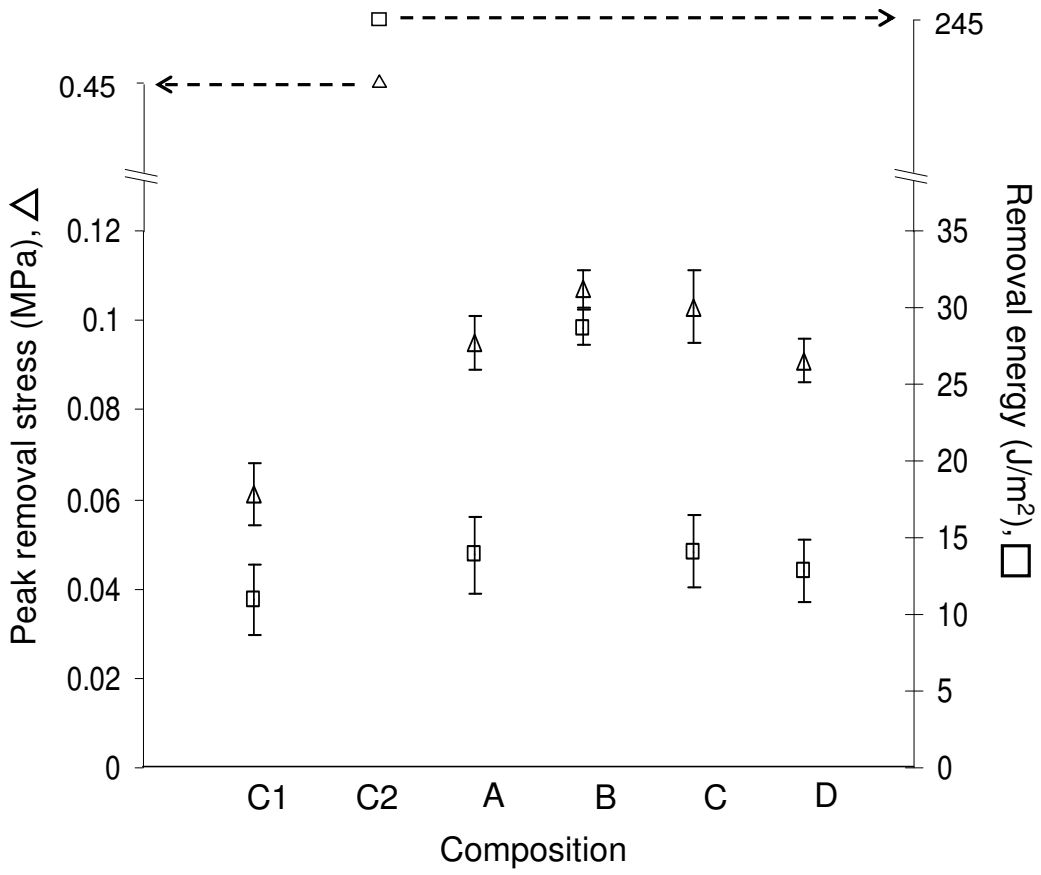

Figure 4.3. Plot represents the peak removal stress and the removal energy as a function of the triblock coating composition.

After a prolonged exposure (42 days) to these fouling organisms, the panels were cleaned and replaced to enable the settlement of hard fouling organisms. It was observed that soft fouling could be easily removed from the surface of the triblock coated panels as shown in figure 4.4. After a prolonged exposure to hard fouling organisms like barnacles and cyprids, it was observed that at 210 psi, the waterjet could remove most of the adhered species from the south facing replicate while the north facing replicate was almost completely clean (figure 4.4). As mentioned earlier, the waterjet was applied to a 50mm x 50mm portion on the panel to remove hard fouling settlement; hence figure 4.5 shows that only a small area at the center of the north and south facing replicates are clean.

As mentioned in the previous chapter, the cumulative effect of having traces of hard block content with hydrogen bonding among the urea and urethane moieties and bulk phase separation between the fluorous and silicone segments imparts remarkable mechanical strength to these triblock copolymers. The tested panels did not show any evidences of undercutting by the fouling organism through the coating. This observation further reinforces the fact that the triblock copolymers have tough bulk mechanical properties. In addition to a tough bulk, the presence of a soft surface (dominated by PDMS) having a low surface energy and low near surface modulus leads to weaker forces of interaction between the fouling organism and the substrate, leading to easy release.

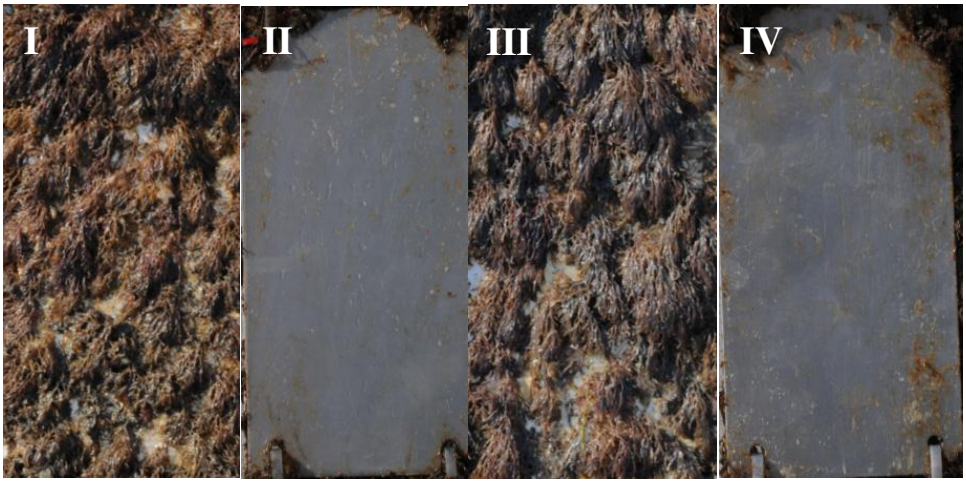

Figure 4.4. Static immersion tests showing the results after a period of 42 days, where I – before cleaning, North, II – cleaned, North, III – before cleaning, South and IV – cleaned, South.

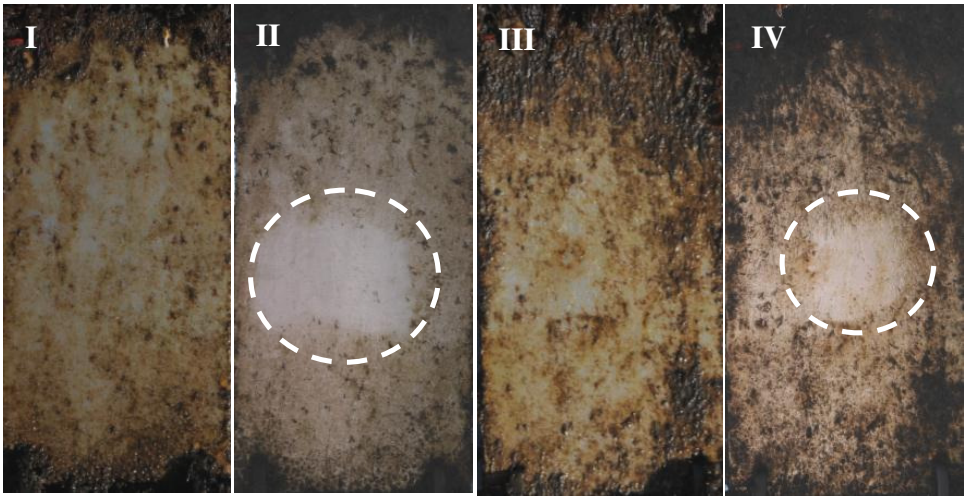

Figure 4.5. Static immersion tests showing the results after settlement of hard fouling, where I – before cleaning, North, II – cleaned, North, III – before cleaning, South and IV – cleaned, South. The waterjet has been applied to the circled portion on the panel.

4.4. Conclusion.

The triblock copolymer as discussed in the earlier chapter has shown interesting surface and bulk morphology. A complete characterization of the bulk and the surface has led us to the conclusion that the silicone domain concentrates at the near surface whereas, the fluorous domain phase separates in the bulk. Release studies performed on triblock coated microscope slides have shown the non adhesive character of the triblock surfaces, recording a low peak removal stress and corresponding removal energy for detachment of an aluminum stud epoxied to the substrate. The peak removal stresses and the removal energies are comparable to a silicone elastomer, with triblock D showing the most promising result. The static immersion tests have reconfirmed the excellent foul release characteristic of the triblock coatings with easy removal of both soft and hard fouling organisms. The observed results have been correlated with the Kendall equation (Eq 4.1). The presence of a PDMS soft block at the near surface generates a low modulus substrate, which further facilitates easy release of adhered objects. In-field tests have shown the effectiveness of a representative composition, B, against both soft and hard fouling organisms. Hence, the remarkable mechanical strength combined with the low surface energy and a low modulus silicone surface provides these triblock copolymers with immense potential for easy foul release applications.

CHAPTER 5

'Flexible Bottlebrush-Nanoglass' hybrid polyurethanes

5.1. Introduction.

Understanding fundamental biology of settlement and growth for fouling organisms and finding ways to control or minimize fouling have been goals of much research and development. The subject is complex, ranging over areas that include fundamental biology, polymer science, coatings technology and, ultimately, paint systems.

Two major components of marine fouling are "soft" organisms such as seaweed[133] and "hard" species including barnacles, mussels, oysters and tubeworms.[132,134,135] Depending on factors such as temperature, salinity, location and time of year, fouling can rapidly roughen a ship hull, greatly increase drag, and cause increased fuel consumption to maintain a given speed. Hard fouling can take the form of invasive species such as zebra mussels, which are notorious for fouling power plant heat exchangers,[136] and are opportunistic organisms in aquaculture.[137]

Various biocides have been incorporated in coatings so that by slow release fouling organisms are killed in the settlement stage. However, ships spend time in ports that are estuarine environments resulting in leached biocides affecting non-target species. For example, 20 ng/l tributyltin was found to cause defective shell growth in oysters.[138] Such developments have led to research and development on environmentally benign methods to control fouling.[139]

While the perfect nonfouling surface remains elusive, a practical target is a coating from which soft and hard fouling can be easily removed. Such coatings that minimize adhesion without release of toxicants or bioaccumulative species are referred to as *foul release coatings*

(FRCs).[139] Applications for such abhesive coatings include not only control of marine biofouling but, because of their benign nature, include a broad scope applications such as in medical devices and in biotechnology to limit bioreactor fouling.[140-142]

The most advanced FRCs are those based on polydimethylsiloxane (PDMS).[139] Commercial PDMS coatings can be maintained relatively free of fouling by cleaning procedures using water jets and brushes.[132,135,143] Factors that bring about weak adhesion (easy cleaning) for PDMS-based coatings include hydrophobicity and low modulus.[123]

The relative importance of low surface free energy compared to other factors is not clear, particularly if the coating is immersed in water. Chaudhury showed that adhesive strength for a thin viscoelastic adhesive on a rigid substrate (silicon) could not be predicted by surface free energy.[119] Unexpectedly, adhesion on a fluorocarbon surface was greater than on certain hydrocarbon surfaces, although the fluorocarbon surface had the lowest surface free energy. The result was explained by invoking a model of adhesion based on interfacial slippage of the adhesive. From this and other work, the paramount importance of mechanical properties to abhesion is clear, but this relationship is often overlooked.

The Kendall equation (Eq 5.1) relates coating thickness and bulk modulus to adhesion, where σ is the critical pull off stress, t is the thickness of the elastomer, w_a is the work of adhesion, and *K* is the bulk tensile modulus.[123]

$$\sigma \sim \left(\frac{w_a K}{t}\right)^{0.5}$$

Eq. 5.1

Instead of thin films on a rigid substrate, such as a silicon wafer,[119] foul-release coatings may have thicknesses that are 100 microns or more. The Kendall criteria for detachment of a rigid cylinder bonded to a thin elastomeric coating on a stiff substrate is an inaccurate approximation for multi-micron thick coatings that are conventionally employed for foul release.

However, a qualitative sense of the importance of modulus may be obtained by considering two coatings that differ only by one having twice the modulus of the other.[132] If only modulus varies, Eq 5.1 predicts that σ increases by 1.4 when the coating modulus doubles. Considering only thickness, σ decreases by 0.7 when coating thickness doubles. From this analysis, adhesion (σ) is minimized by increased thickness and decreased modulus.

The direct relationship between modulus and abhesion is clear from measurements of barnacle shear adhesion strength for a variety of polymers with different moduli.[134] Polymers with relatively high stiffness such as urethanes, epoxies, and acrylates have very high barnacle adhesion (≥ 1 MPa). As predicted by Eq 5.1, soft polysiloxanes have the lowest barnacle adhesion. FEP, a melt processable copolymer of hexafluoropropylene and tetrafluoroethylene has a lower surface free energy than typical polysiloxane elastomers, but ~170 times higher modulus when compared to RTV-11.[132] Barnacle adhesion strength on FEP is 10 times higher than a $CaCO_3$ filled, condensation cured RTV-11 elastomer.[134] Interestingly, considering only on modulus, the ratio of σ (FEP) / σ (RTV-11) = $(170)^{1/2}$ = 13, which is in fair agreement with the ratio of barnacle adhesion strengths for FEP and RTV-11. While the Kendall model is not rigorously applicable, these results provide evidence for the importance of modulus rather than surface free energy in facilitating weak adhesion.

Two polysiloxane FRCs were compared to assess the importance of modulus within this class of elastomers.[132] As for the tests described above, [134] barnacles were removed by an ASTM test that requires pushing with a force gauge at a shallow angle to the substrate.[135] The geometric arrangement approximates shear modulus rather than tensile modulus. Using the relationship E = 3G, where G is the shear modulus for elastomers,[144] adhesion data for an unfilled hydrosilylation cured coating was compared with a filled (RTV11) coating. The ratio of σ for the filled coating

to the unfilled hydrosilylation coating (1.5) was in the range of the value calculated from the respective moduli (1.9).

Although seemingly good candidates for resisting adhesive bonding, Williams has noted that many fluoropolymers (such as FEP discussed above) have relatively high moduli and do not facilitate adhesive bond fracture through peeling.[139] Fluoropolymer elastomers are relatively expensive specialty materials that are obtained in final-molded forms such as gaskets and o-rings tailored for under hood auto, aircraft, and aerospace applications. The precursors to these elastomeric products generally do not have processing characteristics amendable to coating applications. As a result, test facilities seeking fluoropolymers have turned to readily available fluoropolymers such as FEP[134] and polytetrafluroethylene (PTFE). The combination of high adhesion of marine fouling to such surfaces and the paucity of tailored elastomeric fluoropolymer coatings has resulted in the impression that fluoropolymers have poor performance for FR coatings.

However, fluorosilicones are amenable to coating processes and have been successfully employed in FR applications. Fluorosilicone elastomers showed resistance to bacterial adhesion.[145,146] Furthermore, fluorosilicones are established as marine FR coatings.[147] Fluorosilicones rely on incorporation of trifluoropropyl ($CF_3CH_2CH_2$-) side chains that results in high materials cost. As a rough estimate, silicones are a factor of 10 more expensive than commodity polymers, while fluorosilicones add another factor of 10. The high cost of fluorosilicones stems in part from rings being thermodynamically favored rather than chains in equilibrium based ring-chain polymerization processes.[54,148-150] Although fluorosilicones are employed in specialty applications such as tubing and o-rings because of resistance to hydrocarbons and high temperature stability, the high cost of fluorosilicones raises an obstacle

for wide adoption as marine coatings. Furthermore, fluorosilicones may be considered "over-engineered" because a use temperature of ≥250 ºC is not a requirement for marine coatings or even for biomedical applications that require sterilization procedures.

Exploring options beyond fluorosilicones, a series of cross-linkable perfluoropolyether (PFPE) graft terpolymers were characterized and shown to resist spore settlement of the green fouling macroalga Ulva.[151] This fluoropolymer coating with a soft PFPE coating / water interface provides an example of an abhesive coating paralleling the norm for PDMS coatings.

The approach to abhesive coatings described herein focuses on multiscale physical requirements illustrated in figure 5.1 that include the need for: **A**, low work of adhesion; **B**, "soft surface" or more correctly, near surface, that facilitates "peel" and low pull off force (Eq 5.1); **C**, tough bulk mechanicals; and **D**, adhesion to substrate.

These multiscale requirements are met via a hybrid polymeric coating, which is one comprised of inorganic and organic components. By a judicious choice of precursors to the hybrid siliceous inorganic network polymer (INP) and for the linear polymer component, a polyurethane simply designated "U", the multifunctionality required for the physical model shown in figure 5.2 has been achieved with a first generation INP-U abhesive coating. This approach has been validated by an innovative laboratory test for abhesion.

5.2. Experimental

5.2.1. Materials. PolyFOx, PF 6320, that is, poly(3-(2,2,2-trifluoroethoxymethyl)-3-methyloxetane) that is designated herein as 3F diol 1, was obtained from OMNOVA Solutions, Akron, OH. 3-isocyanatopropyltriethoxysilane, 2, (SII 6456) was purchased from Gelest, Inc. Bis(triethoxysilyl)ethane (BTESE), 4, (SIB1817) was obtained from Gelest. Dibutyltin dilaurate

(tech) and 4,4'-methylenebis-(cyclohexylisocyanate), HMDI, were purchased from Aldrich. Tetrahydrofuran, 99.6%, (for analysis ACS, stabilized with BHT) was purchased from Acros.

5.3. Instrumentation / Characterization.

5.3.1. Infrared spectroscopy. FT-IR spectra were obtained using a Nicolet 400 FT-IR spectrometer. Attenuated total reflection ATR-IR spectra of the copolyoxetane coated surfaces were obtained by using a Nicolet iS10 with Smart iTR attachment. A background spectrum was taken before each scan. Coated microscope slides were placed on Ge crystal and 32 scans were taken from 500 to 4000 cm^{-1}. The spectra were analyzed using Omnic software. The penetration of the evanescent infrared wave with the Ge crystal is 0.7 μm.

***5.3.2. Differential Scanning Calorimetry*.** M-DSC was done with a TA-Q 1000 Series™ instrument (TA Instruments) with modulation amplitude of ± 0.5 °C, modulation period of 20 seconds. The sample (5-15 mg) was equilibrated at -90 °C followed by a heating ramp of 6 °C/min till 150 °C. This was followed by a cooling ramp of 10 °C/min back to -90 °C and again the same heating cycle was repeated. Two consecutive heating cycles were also followed to observe any changes with heat treatment. A pre-run sample was also heated at 100 °C to mimic the curing conditions for 24 hr and then kept at ambient for another 24 hr. The same heating-cooling-heating cycles were followed to study thermal transitions. Standard samples of zinc, tin and lead were used for energy and temperature calibration.

***5.3.3. Wetting Behavior*.** The surface wetting characteristics of coated slides were measured by the dynamic contact angle (Wilhelmy plate). DCA was carried out using a Cahn model 312 contact angle analyzer.

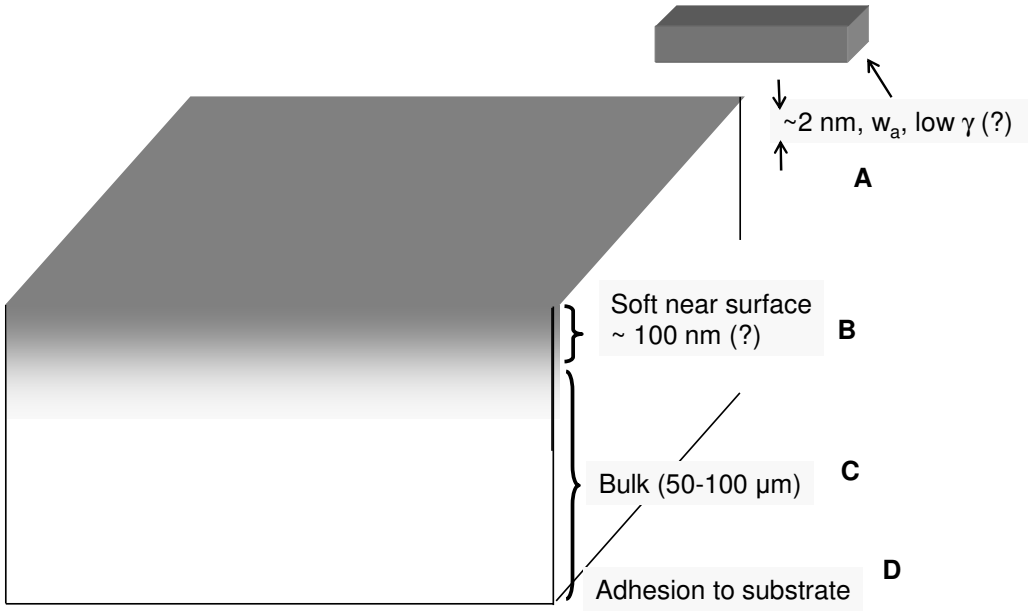

Figure 5.1. A nanoscale, microscale, and mesoscale model for abhesive coatings based on physical principles.

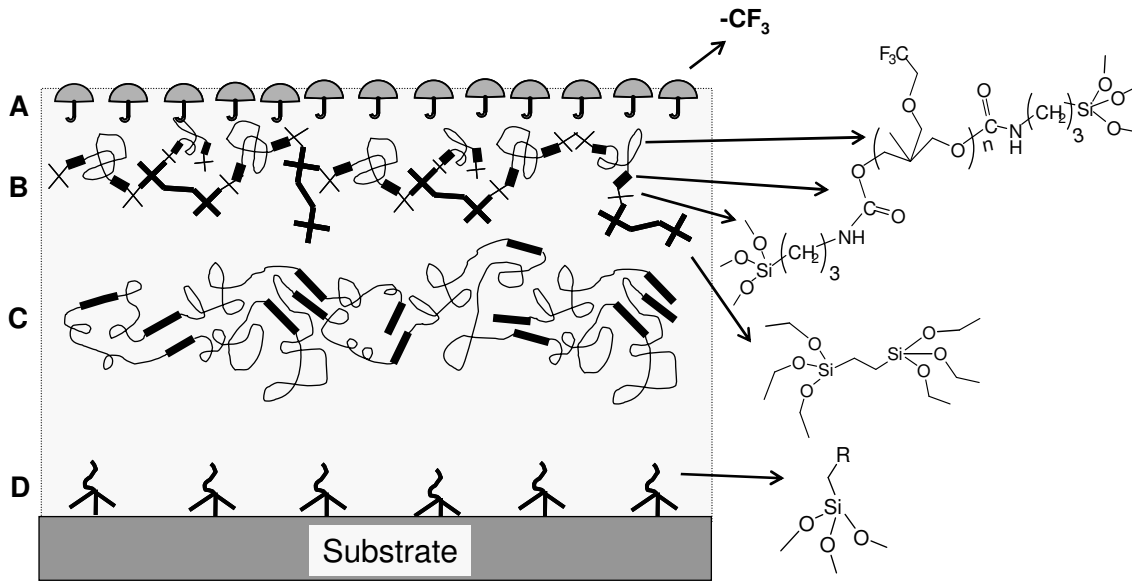

Figure 5.2. With reference to designations in Figure 5.1, schematic for components of INP-U hybrid: **A**, surface concentrated $–CF_3$ from 3F side chain; **B**, INP from the reaction of **1** and **2** followed by condensation polymerization with 3F soft block (~) , urethane (▀) and –Si(O-)3 network (+); **C**, polyurethane represented by hard (▬) and soft (~) block components; **D**, R-Si(O_3) bonding to substrate.

Deionised water was used as the probe liquid for all samples with an immersion/withdrawal rate of 100 μm/s. Reported contact angles are averages of several force-distance cycles. Accuracy is generally ± 1–2°.

Static contact angles and image profiles were obtained by using a Ramé-Hart goniometer equipped with a camera. The contact angles were calculated using Drop Image software (version 1.4.11). The reported value is an average of contact angles obtained from 3 drops taking 5 readings per drop.

5.3.4. Swelling. Oil was estimated by immersing a microscope slide with a representative 3F-Si/H(U-3F-40) coating in hexadecane for 24 hours. For comparison, a condensation cured PDMS coating was made from polydimethylsiloxane diol (4.5 kDa) cured with bis(triethoxysilyl)ethane (10 wt%). To determine mass uptake, each slide was weighed before and after immersion.

5.3.5. Tapping Mode Atomic Force Microscopy (AFM). A Dimension Nanoscope V (Veeco, CA) atomic force microscope was used for morphological analysis of the coated surfaces. Surface interrogation was done in tapping mode using silicon crystal cantilevers (40 N/m). Imaging was done at both soft and hard tapping by altering the setpoint ratio r_{sp} or A_{exp} / A_o from 0.95 to 0.8, where A_o is free oscillation amplitude and A_{exp} is the experimental oscillation amplitude. Images with scan sizes of 50 µm, 10 µm and 2 µm were taken to probe into microscale and nanoscale morphology of the coated surfaces.

***5.3.6. Abhesion test*.** The abhesion test parallels ASTM D5618-94(2011) "Standard Test Method for Measurement of Barnacle Adhesion Strength in Shear." The ease of release was tested by bonding an aluminum cylinder to a fully cured, coated glass slide with an epoxy resin adhesive (Loctite Epoxy, marine, white, Henke Corporation, Rocky Hill, CT, USA).

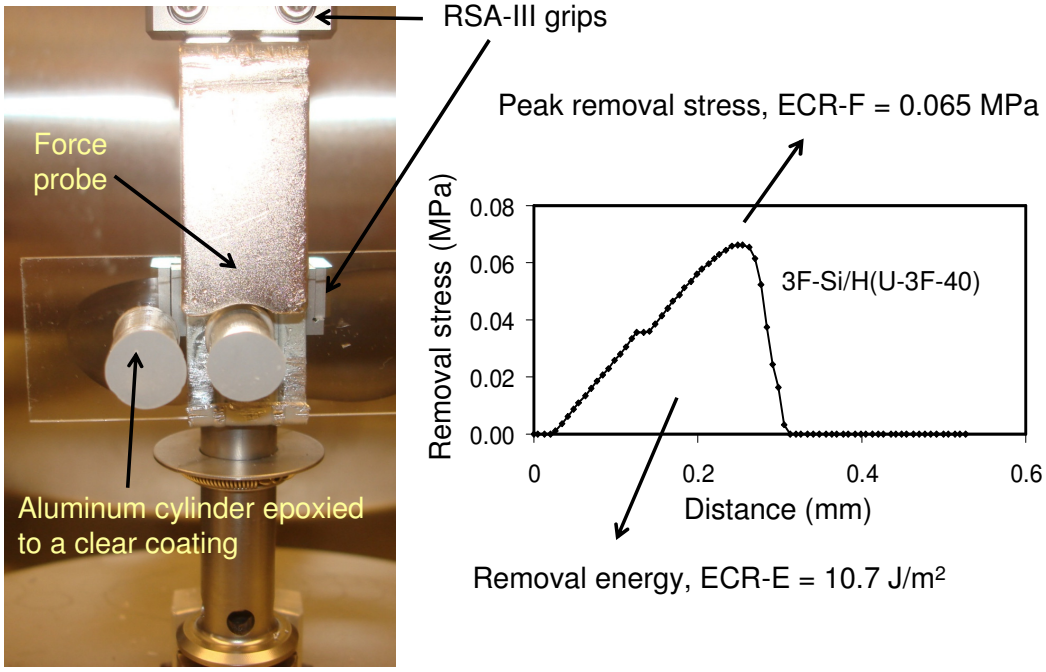

Figure 5.3. Picture of sample holder, force probe, bonded aluminum cylinder, and transparent 3F-Si/H(U-3F-40) coating on a microscope slide for abhesion testing using a TA RSA-III. A typical shear stress / distance result is shown.

This adhesive, recommended by the manufacturer for marine applications, has a suggested cure time of 2 hours. The diameter and height of the aluminum cylinder were 10 x 20 mm, respectively. After spreading a thin film of epoxy on the end of the cylinder, it was placed upright on a coated slide and lightly pressed into place. Over the course of a few minutes, usually three such cylinders were fastened to a single coated glass slide. The epoxy was allowed to cure for a minimum of 24 hr at ambient temperature.

A holder for a glass microscope slide was fabricated and installed in a Dynamic Mechanical Analyser-RSA-III (TA instruments) as shown in Figure 5.3. The coated slides with bonded aluminum cylinders were clamped into the fixture and peak removal stress and removal energy for detachment of the aluminum cylinder was determined. This test gives *peak* removal stress for "epoxied aluminum cylinder removal" (ECR-P) but also ECR *energy* (ECR-E).

The acronym ECR is chosen for the abhesion test so as not to include "A" for aluminum, as the test could just as well be carried out with other materials such as steel or fiberglass. Initially, the test was carried out with wooden dowels, but the dowel was dented by the force probe in the course of testing. Thus, the cylinder should be rigid so as not to deform during the abhesion test. The probe speed was constant at 0.3 mm/min. The RSA-III has a load cell with a maximum load of 3.5 kg. Thus, this abhesion test is only applicable to removal of test specimens those are weakly bonded.

5.3.7. Mechanical testing. Dynamical mechanical and tensile mechanical properties of the coatings/films prepared in last section were measured using a TA instruments RSA III dynamic mechanical analyzer. During analysis sample temperature was ramped from -90 to 150 °C at 5 °C/min while tension cycles were set at 1Hz with maximum strain set to 0.05%. Maximum autotension was set to 2 mm with maximum autotension rate of 0.01 mm/s.

For tensile testing, rectangular samples were stamped out of cast plaques and measure for thickness, width and gauge (mm). After obtaining the sample dimensions, the sample was clamped into the RSA holder. The data acquisition rate was set to 1 Hz while the initial sample elongation rate was set to 10 mm/min. The modulus of elasticity was determined from the initial portion of the stress strain curve. Strain to break was noted, provided that sample extension did not exceed the limits of the instrument (1200%).

5.4. Preparation of Hybrid Coatings.

The hybrid compositions described herein are comprised of (1) a fluorous polyoxetane end-capped with a $-Si(OEt)_3$ functionality for condensation cure and (2) a high strength fluorous polyurethane. GPC on the as received poly(3-(2,2,2-trifluoroethoxymethyl)-3-methyloxetane) showed the presence of ~ 50% impurities which was determined to be mostly comprised of cyclics, $(3FOx)_4$.[68] A liquid-liquid extraction scheme with hexane was devised as described in our previous work[68] which resulted in ≥ 98 % purity of the polyoxetane. Purity of the resulting polyoxetane has been confirmed by GPC and ^{1}H-NMR studies.

The synthesis of the fluorous end-capped copolyoxetane, the fluorous polyurethane and the crosslinked polymeric network is illustrated in Scheme 5.1 and described below.

5.4.1. Synthesis of 3FOx-polyurethane. The synthesis of the 3FOx-PU, designated U-3F, which is an important component of the hybrid system, is described in this section. U-3F was synthesized by modification of the two step, soft block first method described previously.[100] 4,4'-Methylenebis-(cyclohexylisocyanate) (HMDI) and 1,4 butanediol (BD) were used for the hard segment with 3FOx copolyoxetane (3F diol) as a soft segment in solutions with THF.

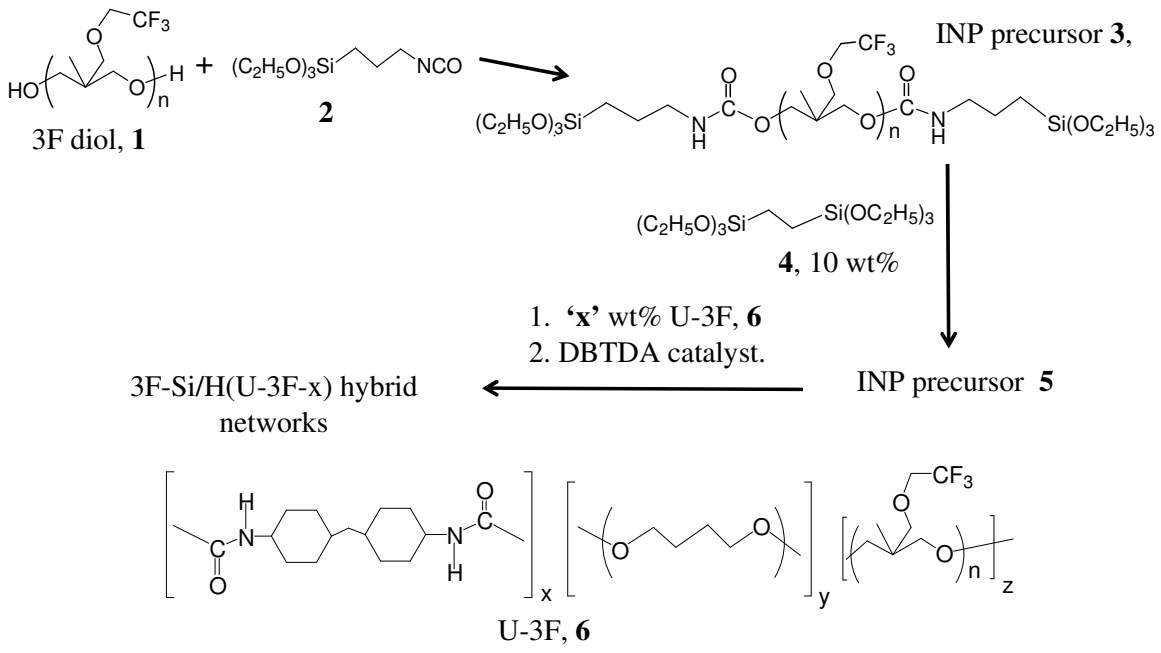

Scheme 5.1. Synthesis of the inorganic network precursors and the hybrid polymer.

In the first step, 7 grams (equivalent to 1.56 mmol polyoxetane diol) 3F diol and 2.34 grams (8.88 mmol) HMDI (a slight excess) are added to a three-neck round-bottomed flask equipped with a mechanical stirrer, nitrogen inlet, and condenser. After addition of 50 ml THF and T-12 catalyst (2 drops of 10 vol% DBTDL in THF), the reactants were kept at 70°C for 3 hr to prepare diisocyanate-terminated prepolymer.

In the second stage, 0.67 gram (7.43 mmol) of BD (diluted in 10 ml THF) was added slowly (with a syringe pump) over a 12-hour period while keep the reaction mixture refluxed at ~70 °C. With slight excess of BD, very slow addition process and relatively fast reaction rate between BD and isocyanate, there will be sufficient reaction time in the flask when the isocyanate/hydroxyl ration is in the vicinity of 1. This ensures high molecular weight polyurethane independent of stoichiometry control and how accurately 3F diol molecular weight is determined. An exception results from the presence of monofunctional 3F diol, which terminates chain growth and results in low molecular weight polyurethanes. Excess BD is removed during the precipitation and re-precipitation process.

After BD is added, a temperature of 70 °C is maintained for 4 hours before cooling to 50°C. The desired polyurethane precipitates when the reaction mixture is poured into 500 ml methanol/water (3:1) mixture. After precipitation, the product was vacuum filtered and dried in air for 2 days. The collected polyurethane was dissolved in 50 ml THF and precipitated in 500 ml methanol/water (3:1) mixture for an additional purification.

The GPC chromatogram for the purified polyurethane is compared to3F diol in figure 5.4. A low molecular weight component peak is not observed for the U-3F although a shoulder can be seen. The weight average molecular weight is 110 kDa.

Coatings (0.5 mm thick) and dip-coated glass slides were prepared by solution casting followed by drying at 60 °C under vacuum for 24 hours. The tensile strength and strain at break for HMDI/BD(30)-P[3FOx-4.5], U-3F, is 9.2 MPa and 1245 % elongation at break (Table 5.1).

Dynamic Contact Angle (DCA) measurements were carried out using dip-coated glass slides. The advancing contact angle for the U-3F is stable for the first 3 cycles within experimental error (Figure 5.11). The post-DCA water check shows no water contamination. Since a very small peak in GPC was attributable to low molecular weight polyurethane and/or cyclics (Figure 5.4), another 4 DCA cycles were carried out on the U-3F coating. Both advancing and receding contact angles remained stable. However, a post-DCA water check showed slight hysteresis in fdc's.

5.4.2. Prepolymer synthesis of fluorous polyoxetane end-capped with -Si(OEt)$_3$. The first step involves the reaction of the fluorous copolyoxetane designated as 3F diol or **1**, with 3-isocyanatopropylteiethoxysilane, **2** (Scheme 5.1). End capping 3F terminal hydroxyl groups via formation of urethane linkages marks completion of the first step. The second step involves addition of different weight percents U-3F polyurethane. The volume fraction of the siliceous domain is enhanced by the addition of bis(triethoxysilyl)ethane **3** (Scheme 5.1). Condensation cure sets in at ambient temperature, that is -Si(OEt)$_3$ condensation cure with concomitant formation of a siliceous coating component. The condensation cure process is driven to completion at 100 °C, overnight.

In a typical reaction 10 g (2.22 mmol) 3F diol **1** was added dropwise via an additional funnel to 1030 µl (4.44 mmol) 3-isocyanatopropyl triethoxysilane **2** (Scheme 5.1) with continuous stirring in a 250 ml reaction vessel. Each of the reactants was dissolved in THF (10 g). The reaction was carried out at room temperature (~ 30 °C) for 24 hours. To prevent

hydrolysis of alkoxy silane **2**, water the reaction was carried out under a continuous dry nitrogen purge.

The extent of reaction between terminal alcohol groups (1) and isocyanate (2) was determined by removing a small sample of the reaction mixture at successive time intervals and obtaining an IR spectrum on KBr discs. Disappearance of OH (~ 3500 cm-1) and NCO (~ 2200 cm-1) peaks with concurrent growth of NH (urethane, ~ 3300 cm-1) as observed in Figure 5.5, confirmed the completion of step 1. Next, 0.5 wt% of DBTDA catalyst and bis(triethoxysilyl)ethane 3, 10 wt% (~ 1.0 ml) were added (Scheme 5.1). Addition of 3 served to increase the volume fraction of siliceous domain in the final product. The composition at this stage comprises a solution of INP precursor designated 5 (Scheme 5.1).

5.4.3. 3F-Si/H(U-3F-x) Compositions. A THF solution of U-3F was added to INP precursor 5 to provide multiple compositions with increasing weight percent 'x', where, x (% U-3F) = 10, 30, 40, 50, 60, 75 and 90. After U-3F addition, stirring was continued for 30 minutes to obtain a homogenous solution and to achieve an increase in viscosity from condensation polymerization. As a control, a sample of INP precursor 5 was cured without addition of U-3F. This control sample is designated 3F-Si/H.

At this stage, and for an additional 4 hours, the solution had a suitable viscosity for coating. Microscope slides were drip coated and glass cover slips were dip coated and cured at ambient overnight before completing condensation / sol-gel cure at 100 °C for 24 hr. To prepare plaques with thickness ~ 150 µm, the solution was spread on PTFE plates, allowed to cure overnight at ambient temperature, and cured at 100 °C for 24 hr. Masses of reactants for the different hybrid compositions are listed later on in this chapter in Table 5.1.

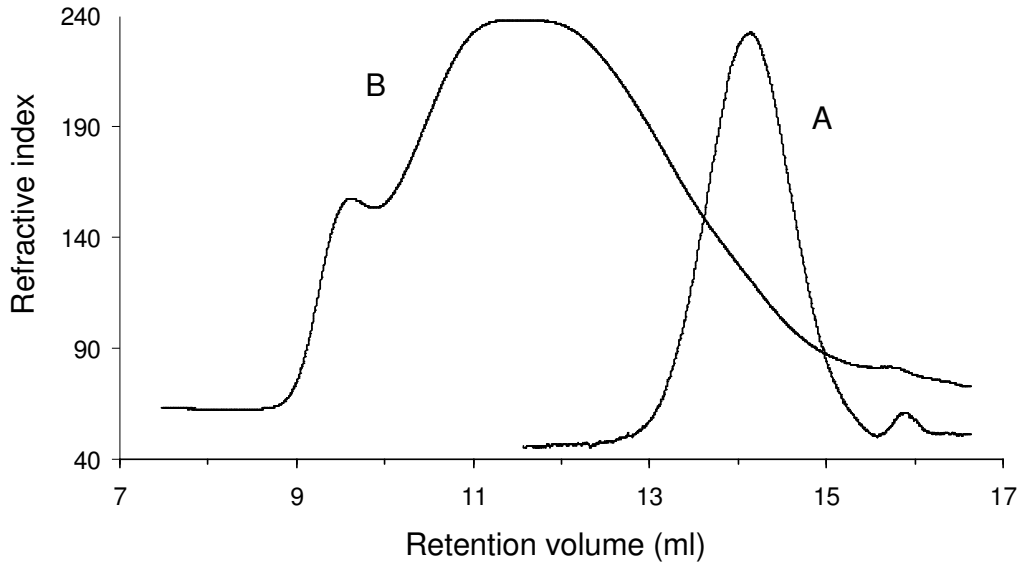

Figure 5.4. GPC for **A**, 3F diol **1** and **B**, HMDI-BD(30)/P(3FOx-C1-4.5), U-3F.

5.5. Results and Discussion - Implementation of Coating Design. The multiscale requirements delineated in figure 5.1 have been implemented in a hybrid coating comprised of components depicted in figure 5.2. The soft near surface domain is comprised of a hybrid siliceous inorganic network polymer (INP). Bulk toughening is affected by a linear polyurethane HMDI/BD(30)-(3F-4.5) designated "U-3F". Details on composition and processing are described followed by characterization of bulk and surface properties.

First generation elastomeric coatings are based on 1, poly(3-(2,2,2-trifluoroethoxymethyl)-3-methyloxetane) diol designated "3F" (Scheme 5.1). Characterization of bulk properties are discussed first, including thermal transitions, mechanical properties, and susceptibility to swelling by hydrocarbon oil (hexadecane). Secondly, surface properties are examined by ATR-IR spectroscopy and wetting behavior. Finally, a new test for abhesion is introduced that involves removal of an aluminum cylinder bonded to the coating with epoxy adhesive. The innovative part of this test is the facile determination of energy of removal in addition to peak removal force.

The soft block precursor for both INP and U is 3F diol **1** (Scheme 5.1). As the fluorous polymer ("P") component of the INP, concentration of $-CF_3$ moieties at the coating surface is aimed at a surface with a low work of adhesion (Figure 5.1). The 3F soft block is the "soft" organic component of the INP (Figure 5.2).

5.5.1. INP Precursors 3 and 5. The reaction sequences for the INP reactive precursors are shown in Scheme 5.1. Common to all coatings, reaction of 3F diol **1** and isocyanate **2** in THF is carried out under nitrogen purge at near ambient temperature (~30 °C) to prevent premature alkoxide hydrolysis. The reaction of polyol **1** with isocyanate **2** followed the approach developed by Saegusa and Chujo.[76,152]

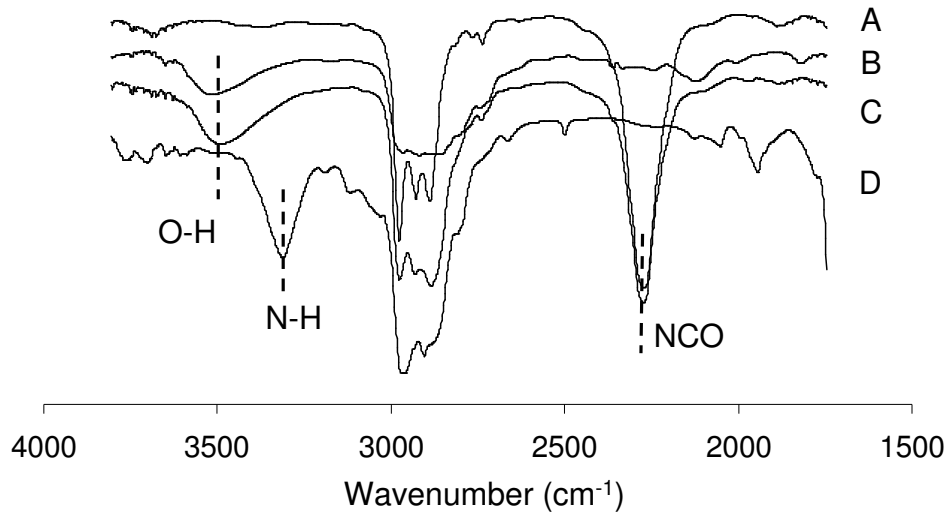

Figure 5.5 FTIR spectroscopic monitoring of INP precursor **3** formation: **A**, isocyanate alkoxysilane **2**; **B**, 3F diol **1**; **C**, initial (t = 0) reaction mixture; **D**, reaction mixture at t = 24 hr.

The formation of INP precursor **3** was monitored by IR spectroscopy (Figure 5.5).[100,153] The FTIR spectrum for **1** (Figure 5.5) has a broad peak at 3500 cm^{-1} characteristic of terminal -OH for the 3F diol. The spectrum for **2** has a peak at 2200 cm^{-1} confirming the presence of isocyanate.[154] The spectrum at time (t = 0) after mixing **1** and **2** has the expected OH and NCO peaks. The IR spectrum after 24 hr (Figure 4-0) shows the absence of NCO and OH peaks and the presence of amide NH (3300 cm^{-1}).[100,153] This finding confirms the formation of INP precursor **3** with end-capped alkoxy silane moieties.

The volume fraction of siliceous domain was increased by introducing 10 wt% BTESE **4** to generate INP precursor **5**. Condensation polymerization was initiated by terminating the nitrogen purge and adding 0.5 wt% DBTDA catalyst. As a control, a crosslinked hybrid coating was made without addition of U-3F, polyurethane **6**. This composition is designated 3F/Si-H-10. The weight percent **4** is the same in all hybrid coating compositions. To simplify designations, "3F-Si/H" will be used for the hybrid 3F composition. For example, 3F-Si/H(U-3F-40) is the hybrid composition consisting of the 3F-Si/H siliceous component together with 40 wt% U-3F.

5.5.2. U-3F. Polyurethanes containing **1** were prepared following a modification of routes described previously.[71,155] To optimize molecular weight for maximum mechanical properties and to avoid water contamination that can confound contact angle determinations, 3F diol was purified by liquid-liquid extraction with hexane to remove cyclics and low molar weight (LMW) species. A two step process was used to prepare polyurethane 3F-U. The first step was addition of 3F diol to HMDI (THF, 70 °C). In the second stage, BD was added slowly with a metering pump or syringe pump over a 12-hr period. With slow addition and a relatively fast reaction rate between BD and isocyanate, high molecular weight polyurethane is obtained. 3F-U was isolated by precipitation into methanol/water (3:1), which was used for an additional reprecipitation.

The GPC for U-3F (Scheme 5.1) is compared to the 3F diol **1** in Figure 5.4. The peak due to residual cyclics and LMW species seen in the GPC for 3F at a retention volume of 16 ml is negligible for U-3F. M_w for U-3F is 110 kDa. The tensile strength and strain at break for U-3F are 9.2 MPa and 1245 %, respectively. U-3F dip-coated coverslips were used for dynamic contact angle (DCA, Wilhelmy plate) measurements. Contact angles were stable for 4 cycles (θ_{adv} = 109 ±1°; θ_{rev} = 70 ±1°) with no water contamination being observed in a post-DCA water check.

5.5.3. 3F-Si/H(U-3F-x) crosslinked hybrid networks. Polyurethane **6**, U-3F, was added to INP precursor **5**. The solution was stirred for 30 min to initiate crosslinking and build viscosity to facilitate casting and dip or drip coating. After condensation cure in air (25 /100 ºC) 3F-Si/H(U-3F-x) hybrid network coatings are formed where x is the wt% **6** (Scheme 5.1). The coatings have a slight haze but are essentially optically transparent (Figure S5.1). Coatings on microscope slides were immersed in water for several days without delaminating. Excellent adhesion to glass and aluminum is attributed to bonding of intermediates in the hydrolysis / condensation polymerization of silyl alkoxides.

5.6. Bulk Characterization.

5.6.1. Differential Scanning Calorimetry. Figure 5.6 shows MDSC for compositions discussed below, while Figure S5.2 contains MDSC thermograms for remaining compositions. The control hybrid 3F-Si/H has a T_g for 3F at -45 ºC (Figure 5.6). The T_g for 3F is virtually identical to that for the 3F diol (-47 °C).[43,100]

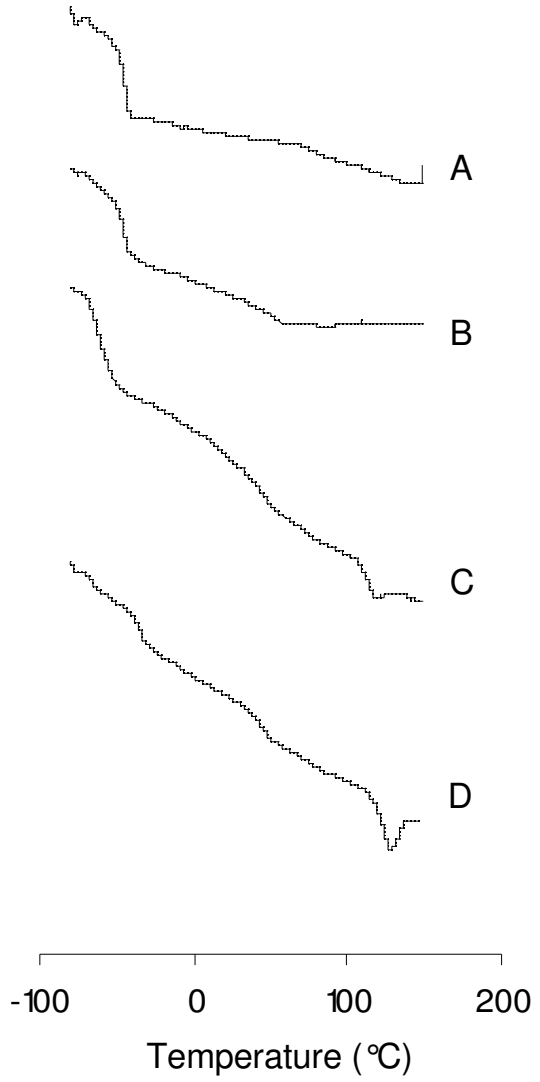

Figure 5.6. Differential scanning calorimetry, MDSC: **A**, 3F-Si/H; **B**, 3F-Si/H(U-3F-40); **C**, 3F-Si/H(U-3F-50) and **D**, U-3F.

Polyurethane 3F-U has a 3F soft block T_g at -35 ºC and a hard block T_m at 128 ºC with a modest ΔH_m (3.4 J/g). The 3F T_g for U-3F is 12 °C above that for the 3F diol indicating good phase separation.[43] 3F-Si/H(U-3F-50) is the threshold composition for detecting a hard block T_m in the hybrid elastomer (117 °C, ΔH_m, 0.94 J/g, Table 5.1). For compositions with higher wt% U-3F, T_m occurs at approximately the same temperature. The wt% HMDI-BD hard block for 3F-Si/H(U-3F-50) is 15%, half that of 3F-U (30 wt%). The ΔH_m (0.94 J/g) is ~30% that of neat U-3F, which has a T_m about 10 °C higher than the hybrid compositions (Table 5.1).

In summary, 3F-Si/H(U-3F-x) hybrid elastomers with greater than 40 wt% U-3F have a separate hard block phase. However, the volume fraction of this phase is about 1/3 that for neat U-3F. Nevertheless, it is interesting that despite the 3F-Si/H siliceous network the HMDI-BD hard block phase separates.

Glass transition temperatures are often difficult to detect in DSC due to small endotherms associated with the second order glass to rubbery transition. As discussed above, the T_g for the 3F soft block is easily identified. Thermal transitions that are associated with the hard block, which has a much lower weight percent compared to the soft block, are assigned to changes in slope in some of the thermograms in the vicinity of 80 °C. These assignments (Table 5.1) are tentative and are the subject of continuing investigations. Surprisingly, even low weight percents of U-3F result in compositions that display hard block T_g's. The 10% and the 30% U-3F show a higher T_g at 85 and 102 ºC, respectively.

5.6.2. Tensile Mechanical Properties. Coatings were obtained for 3F-Si/H and 3F-Si/H(U-3F-10) compositions, but plaques were easily fractured precluding mechanical property measurements. 3F-Si/H(U-3F-30) was the strength threshold for obtaining tensile mechanical property measurements (Table 5.1).

Table 5.1. Hybrid coatings: reactant quantities, DSC transition temperatures, tensile testing and dynamic mechanical data.

Designation	Mass INP **5** (g)[a]		Mass 3F-PU **6** (g)[a]	MDSC			Tensile test		DMA				
	3	**4**		$T_{g,sb}$, $T_{g,hb}$ (ºC)	$T_{m,hb}$ (ºC)	ΔH_m (J/g)	Modulus (MPa)	Strain at break (%)	T_g (ºC)	T_m (ºC)	Storage modulus (MPa)		
											0 ºC	25 ºC	100 ºC
3F-Si//H			0	-45, 65	-	-	-[b]	-[b]	-[b]	-[b]	-[b]	-[b]	-[b]
3F-Si/H(U-3F-10)	2	0.2	0.22	-47, 84	-	-	-[b]	-[b]	-[b]	-[b]	-[b]	-[b]	-[b]
3F-Si /H(U-3F-30)	2.2	0.22	0.94	-62, 102	-	-	0.2	47	-27	94	28	25	3.9
3F-Si /H(U-3F-40)	2.2	0.22	1.46	-45, 35	-	-	2.1	391	-22	-	11	6.4	2
3F-Si /H(U-3F-50)	2.2	0.22	2.2	-62, 36	117	0.9	0.94	463	-29	115	14	9.6	2
3F-Si /H(U-3F-60)	2.2	0.22	3.3	-49, 56	122	1.4	2.3	549	-24	148	17	7.8	1.7
3F-Si /H(U-3F-75)	2	0.2	6	-55, 52	118	1.0	1.2	574	-27	142	16	7.7	1.5
3F-Si /H(U-3F-90)	2.2	0.22	19.8	-53, 44	119	3.1	2.2	1175	-30	129	20	13	1.6
U-3F	-	-	-	-35, 45	128	3.4	8.4	1250	-	-	-	-	-

a. Sufficient THF for solution.
b. Too fragile for stress-strain tests.

3F-Si/H(U-3F-30) had a strain-to-break of 47%. On further increasing U-3F content to 3F-Si/H(U-3F-40), a remarkable improvement in toughness was observed with a strain-to-break of 490%. For hybrid compositions with U-3F ≥ 40 wt%, toughness increased with increasing wt% U-3F. The mechanical properties for 3F-Si/H(U-3F-90) were comparable to neat U-3F; samples did not break in the tensile test up to the strain limit of ~ 1200 %.

5.6.3. Dynamic Mechanical Analysis. DMA measurements were carried out to probe retention of mechanical properties at elevated temperatures. Again, samples for the 3F-Si/H control and 3F/H(U-3F-10) were too fragile to test.

Figure 5.8 shows the results from DMA for 40 and 50 wt% U-3F films. All compositions are glassy below T_g with storage moduli of ~ 10^{10} Pa. Above the 3F T_g that ranges from -40 to -50º C depending on composition (Table 5.1), the storage moduli decrease about 100 fold over a 40 ºC interval. The onset of a long rubbery plateau with a storage modulus of ~ 10^6 Pa begins at 0 ºC. The long plateau suggests a broad use temperature. Storage moduli for all compositions at 0 and 100 ºC are listed in Table 5.1.

Figure 5.8 shows that there is a broad rise in tan δ but no distinct thermal transition for 3F-Si/H(U-3F-40) above 100 ºC. Increased 3F-U content for 3F-Si/H(U-3F-50) results in a tradition centered at 130 ºC that corresponds to the endotherm in DSC and is assigned to hard block melting. Above the hard block T_m, the modulus drops by another order of magnitude.

5.6.4. ATR-IR Spectroscopy. Attenuated total reflection infrared (ATR-IR) spectroscopy using a Ge crystal gives us a qualitative idea of the surface functionalities to a depth of ~ 700 nm. ATR-IR spectra were obtained for all compositions and a representative spectrum is shown in figure 5.9 for 3F-Si/H(U-3F-40). Figure 5.9 shows the expected carbonyl peak at 1700 cm^{-1} and NH peak at ~3300 cm^{-1}.

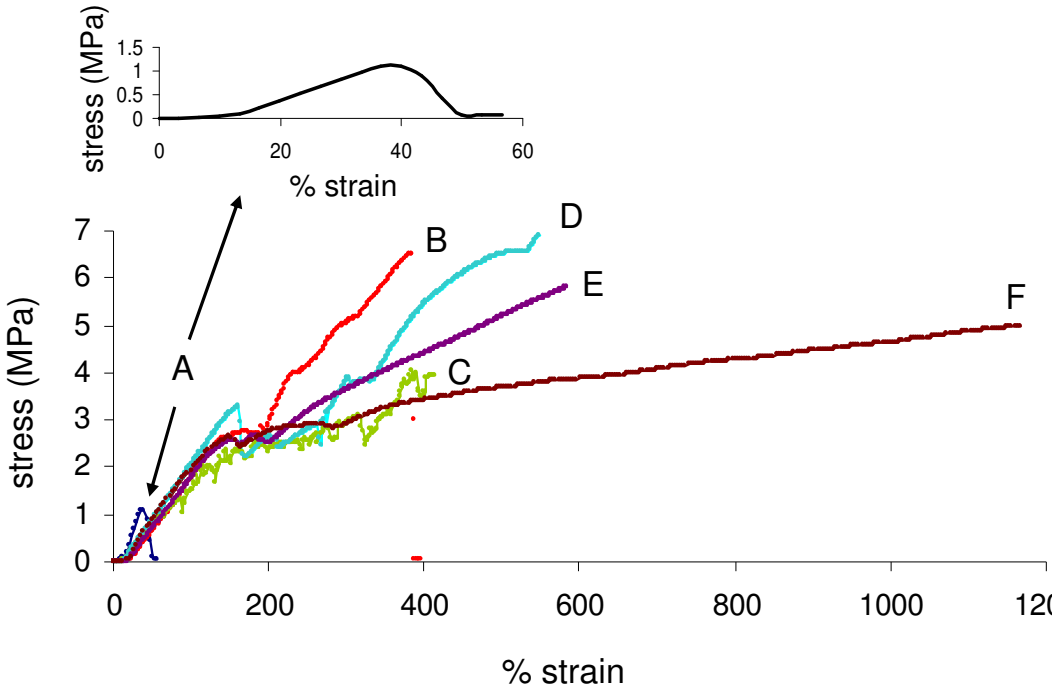

Figure 5.7. Stress-strain curve for 3F-Si/H(U-3F-x). **A**, 30, **B**, 40, **C** , 50, **D**, 60, **E** , 75, **F**, 90. The insert shows the stress vs strain relationship for 3F-Si/H(U-3F-30).

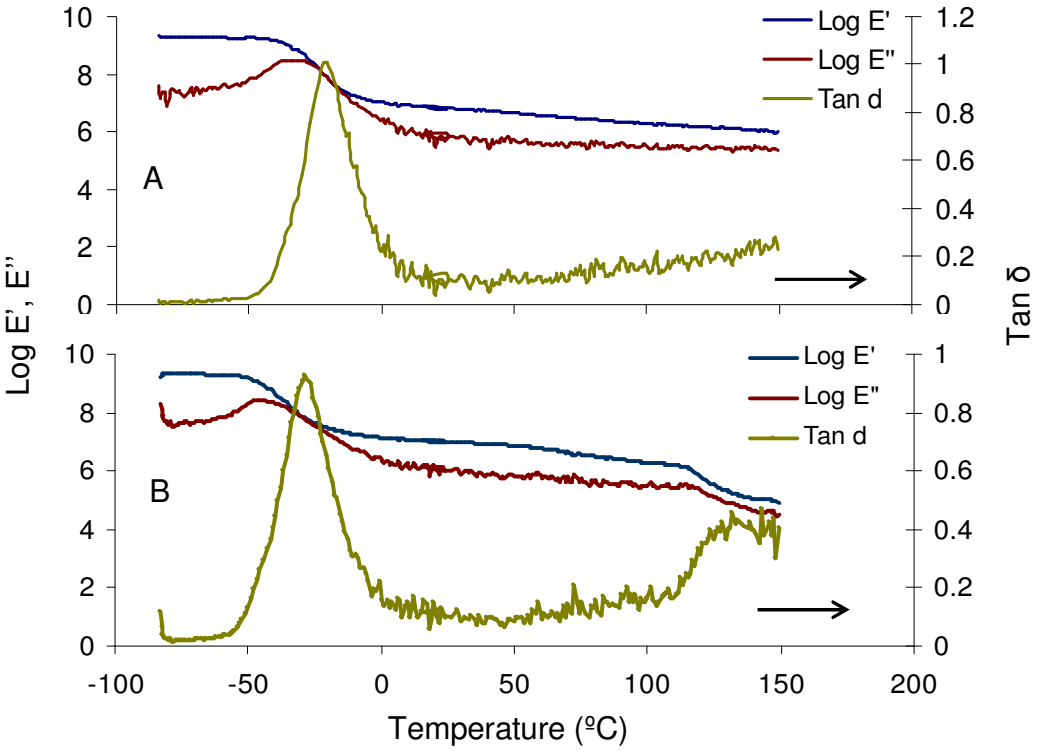

Figure 5.8. DMA vs temperature for: **A**, 3F-Si/H(U-3F-40) and **B**, 3F-Si/H(U-3F-50) cast films. Left ordinate: Log storage modulus (E') and loss modulus (E''); Right ordinate: Tan δ.

The ATR-IR study was done in order estimate the near surface concentration of urethane moieties. The area of the CO peaks was measured for each of the composition, normalized with respect to the peak area for the neat U-3F (Figure 5.9). The normalized CO peak areas have been listed in Table 5.2. It is seen that for compositions ranging from 40% to 75% U-3F, the carbonyl peak area is 0.3 to 0.34 times the area for the neat polyurethane, i.e., the number of urethane groups at the surface for these compositions is one-third as compared to that of the neat U-3F. Even the 3F-Si/H(U-3F-90) hybrid coating has a normalized peak area of ~ 0.5 which shows that the presence of even 10 wt% of the prepolymer is able to capture 50 % of the urethane moieties in the bulk and prevent them from concentrating at the near surface.

5.7. Surface Characterization.

5.7.1. TM-AFM. Images for 3F-Si/H(U-3F-x) coatings were obtained to investigate topology and morphology for these novel hybrid systems. An entire set of AFM images are provided in Supplemental Information (Figures S5.5-S5.7). Selected images are presented in Figures 5.10 and 5.11. Previously other alkoxysilanes have been used for condensation cure. However, mass loss and/or delayed onset of surface features were observed.[37,Uilk, 2000]

[#5932]Bis(triethoxysilyl)ethane **4**, was chosen to augment the siliceous domain because it is a single chemical compound that is nonvolatile.

TM-AFM of 3F-Si/H was investigated to compare surface morphological changes resulting from the addition of U-3F. TM-AFM images for 3F-Si/H are shown in Figure 5.10 (r_{sp} = 0.95). Images at harder tapping (r_{sp} = 0.8) are similar (Figure S5.5). The 50 x 50 μm phase image reveals a remarkably complex near surface morphology. These features are an apparent result of phase separation and shrinkage during condensation cure.

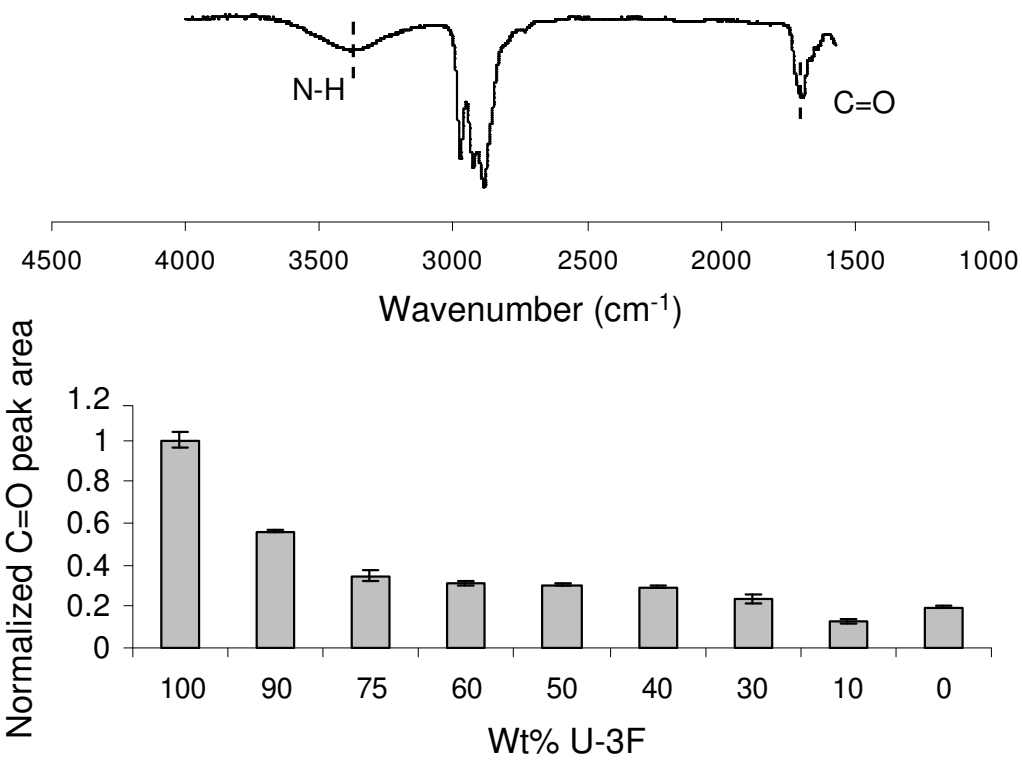

Figure 5.9. ATR-IR spectrum of 3F-Si/H(U-3F-40) showing the presence of an NH and a C=O peak and below, the normalized C=O peak area has been plotted as a function of wt% U-3F.

Table 5.2. Hybrid coatings: contact angles, ATR-IR normalized carbonyl peak areas and RSA-III abhesion data.

Designation	Contact angles (°)		Normalized C=O peak area	Coating thickness (μm)	Abhesion (RSA-III)	
	θ_{adv}	θ_{rec}			ECR-P Peak Removal Force (MPa)	ECR-E Removal Energy (J/m^2)
3F-Si//H	110	64	0.18	400	0.046	6.4
3F-Si/H(U-3F-10)	108	55	0.13	300	0.093	17.5
3F-Si /H(U-3F-30)	115	47	0.24	300	0.094	18.2
3F-Si /H(U-3F-40)	106	56	0.29	300	0.068	10.3
3F-Si /H(U-3F-50)	102	58	0.3	200	0.078	5.1
3F-Si /H(U-3F-60)	103	56	0.31	250	0.14	37.1
3F-Si /H(U-3F-75)	108	57	0.34	200	0.15	36
3F-Si /H(U-3F-90)	112	51	0.56	200	0.46	133
U-3F	106	55	1	300	0.5	145.4

There may be a synergy resulting from hydrogen bonding between the urethane and remainder –Si-OH groups that underlies this complex morphology.

3F-Si/H(U-3F-x). Figures S5.5-S5.7 contain a complete set of TM-AFM images for 3F-Si/H(U-3F-x) compositions. Figure 5.10 shows that including only 10 wt% U-3F results in a dramatic change in near surface morphology. 3F-Si/H(U-3F-10) has a much less complex surface morphology with only fine grained features noticeable in the 10 x 10 μm (r_{sp} = 0.95) 2D and phase images (Figure 5.10). Only one set of images is shown as the entire set of phase and 2D height images are virtually featureless.

Like 3F-Si/H(U-3F-10), hybrid compositions with higher U-3F weight percents generally have much less complicated near surface morphologies compared to 3F-Si/H. 3F-Si/H(U-3F-30) images are shown in Figure 5.10. A pattern of fine micron scale features are seen in the 50 x 50 μm images as well as nanoscale phase separated domains in the 2 x 2 μm images. For a comparable scan area, surface roughness (R_q is shown in the 2D height images) is less for 3F-Si/H(U-3F-x) hybrids compared to 3F-Si/H.

Figure 5.11 shows images for 3F-Si/H(U-3F-40) and 3F-Si/H(U-3F-50). Because of the relatively featureless surfaces, only images for a setpoint ratio of 0.8 are shown. Nanoscale features are attributed primarily to near surface siliceous domains, as surface depletion of U-3F is shown by ATR-IR (vida infra). Darker colored patches similar to the 3F-Si/H(U-3F-30) hybrid coatings are also observed here for smaller scan sizes. The 3F-Si/H(U-3F-50) hybrids show a very smooth surface with very faint or no features at softer tapping whereas hard tapping shows a phase mixed near surface morphology.

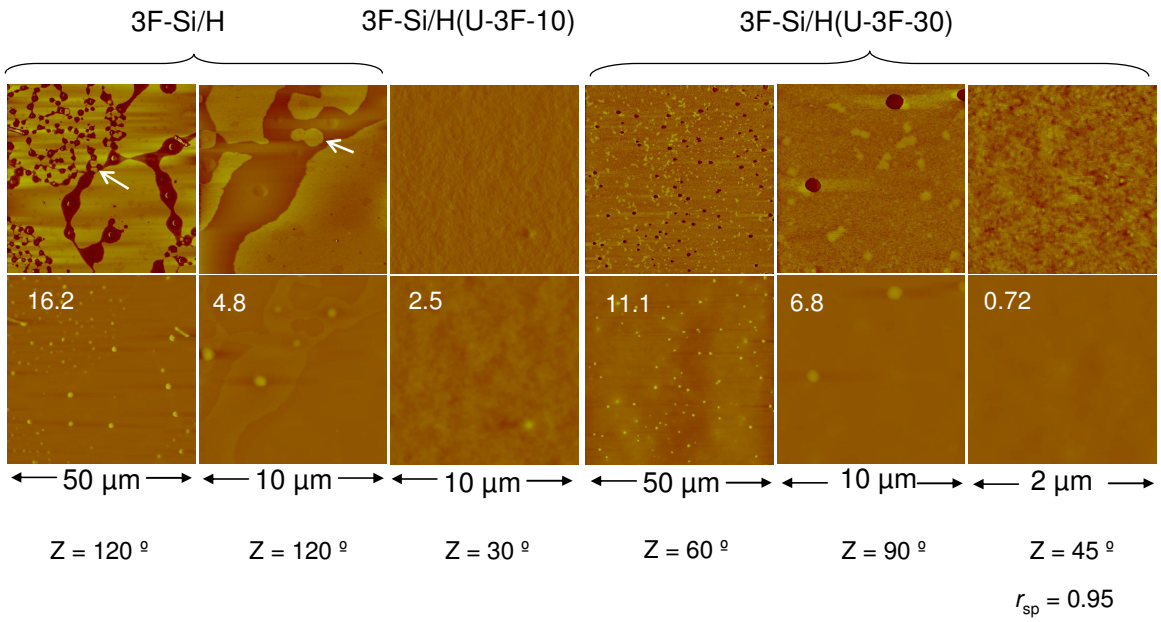

Figure 5.10. TM-AFM images for 3F-Si/H (arrow points to enlarged feature), 3F-Si/H(U-3F-10) and 3F-Si/H(U-3F-30) coatings; upper, phase; lower, 2D height with Rq; r_{sp} = 0.95

3F-Si/H(U-3F-60) coatings are exceptional in showing high surface roughness and a very well segregated near surface morphology (Figure S5.7). Perhaps some as yet not understood variation in coating deposition accounts for this exceptional surface morphology. Smaller scan sizes show a phase mixed near surface morphology.

The 3F-Si/H(U-3F-75) coating shows strand like near surface features that are well dispersed throughout the phase image. These features are observed to be more prominent at softer tapping rather than hard tapping, signifying that they are more predominant at the near surface. For harder tapping at the nanoscale, some signs of phase separation are observed.

The 3F-Si/H(U-3F-90) coating shows a fair amount of phase separation at both the microscale and the nanoscale having distinct light and dark colored regions throughout the phase image. These AFM images are very much analogous to those for the neat 3FOx polyurethane signifying the fact that most of the near surface of 3F-Si/H(U-3F-90) is dominated by the linear U-3F. 3F-Si/H(U-3F-90) coatings have relatively high Rq values.

5.7.2. Dynamic Contact Angles. DCA measurements were done to analyze the surface wetting characteristics of the hybrid polymeric coatings. To determine hydrophobicity of the coated surfaces, water was used as the probe liquid. Figure S5.8 shows representative force distance curves (fdc) for 3F-Si/H and 3F-Si/H(U-3F-40). Completely overlapping force-distance curves demonstrated the fact that there were no leachable components from the coating and the surface tension of water remained unaltered after running a coated slide (no water contamination).

Figure 5.12 shows that the advancing contact angles for all the other hybrid compositions are between 102º and 112º, less than that for the neat U-3F. Figure 5.12 shows that except for the 3F-Si/H(U-3F-30), all the other hybrid compositions have shown a fairly constant contact angle hysteresis of ~ 50º. The 3F-Si/H has shown a θ_{adv} of 110 degrees and a θ_{rec} of 63 degrees.

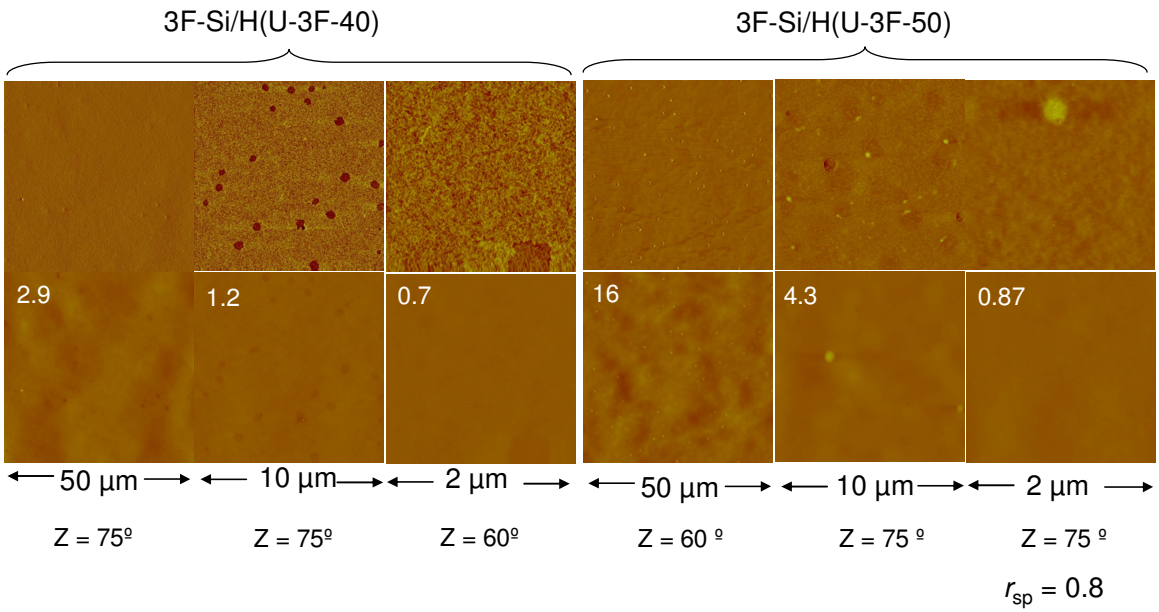

Figure 5.11. TM-AFM images for 3F-Si/H(U-3F-40) and 3F-Si/H(U-3F-50) coatings; upper, phase; lower, 2D height with Rq; r_{sp} = 0.8

Three consecutive cycles were run with each sample and the fdc's overlap each other, which further signify no water contamination. The advancing contact angles for each of the hybrid compositions have shown that the near surface has a considerable hydrophobic character. This result can be attributed to the fact that the near surface has a monolayer of fluorinated moieties that prevent diffusion of leachable components to the aqueous environment.

The oil uptake by these coatings in comparison to PDMS was investigated by selecting the 3F-Si/H(U-3F-40) composition. After immersing the coated slides in hexadecane for 24 hours it was observed that the 3F-Si/H(U-3F-40) absorbed 5.1% of hexadecane while the neat PDMS coated slide absorbed 35.5% of hexadecane. This remarkable difference in oil uptake between the 3F-Si/H(U-3F-40) hybrid coating and PDMS can be attributed to the fact that the presence of a certain fraction of fluorous moieties at the surface acts as a barrier to the diffusion of hexadecane into the matrix.

5.7.3. Sessile drop measurement. The static contact angle was also measured for these hybrid polymers and the values have been plotted in Figure 5.12. High contact angles have been observed for the 3F-Si/H, 3F-Si/H(U-3F-10) and the 3F-Si/H(U-3F-30) hybrid coatings. The static contact angle values follow a similar trend as compared to the advancing contact angles measured by DCA. A minimum in the static contact angle curve is reached for the 3F-Si/H(U-3F-50) and 3F-Si/H(U-3F-60) hybrid coatings with values of 98º and 97º respectively. The contact angle value increases again with an increase in the weight percent of the linear U-3F in the bulk matrix. Overall these measurements suggest that these coatings have a hydrophobic near surface with the extent of hydrophobicity varying with the weight percent of linear polyurethane in the matrix.

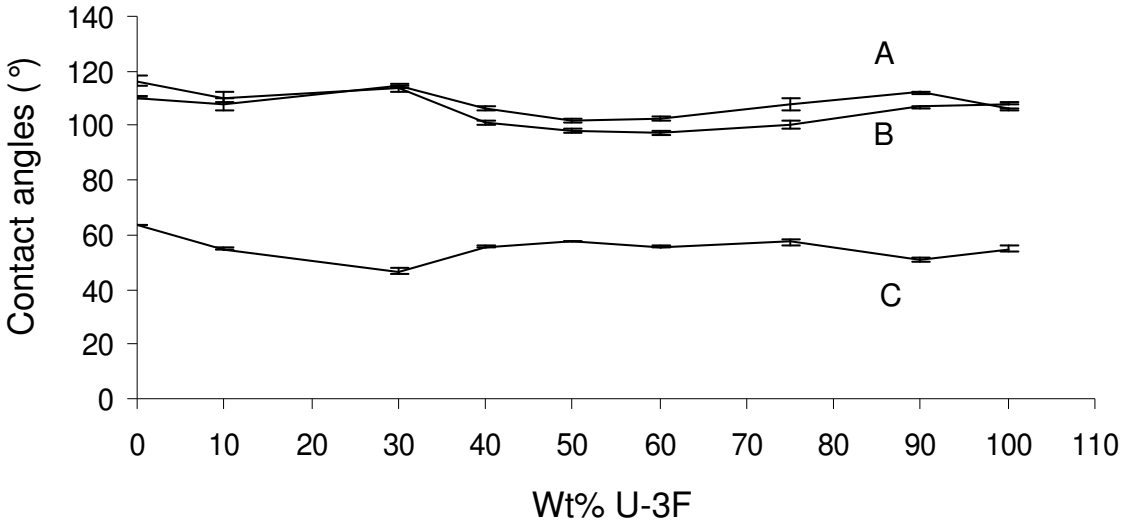

Figure 5.12. Contact angles as a function of wt% U-3F for hybrid coatings: DCA (Wilhelmy plate), **A**, **B;** sessile drop, **C**.

5.7.4. Abhesive Surface test. An abhesion test was developed using a TA RSA-III dynamic mechanical analyzer. This test gives *peak* force for "epoxied aluminum cylinder removal" (ECR-P) but also ECR *energy* (ECR-E). The ECR test was used for all hybrid compositions and U-3F. That is, although plaques of 3F-Si/H and 3F-Si/H(U-3F-10) tore easily and were too fragile for tensile and DMA tests, the coated slides could be tested by ECR.

3F-Si/H had a peak removal force at 0.046 MPa (Figure 5.13, Table 5.2). With incorporation U-3F, the peak removal stress ECR-P increased to 0.093 MPa for 3F-Si/H(U-3F-10) and 0.094 MPa for 3F-Si/H(U-3F-30). Unexpectedly, increasing U-3F weight percent resulted in a reversal of the trend and a minimum in ECR-P of 0.068 MPa for 3F-Si /H(U-3F-40). The ECR-P of 0.078 MPa for 3F-Si /H(U-3F-50) is slightly higher at but ECR-E, the removal energy, is the minimum observed for all hybrid coatings (5.1 J/m^2). For 3F-Si/H(U-3F-60), ECR-P (0.14 MPa) and ECR-E (37.1 J/m^2) are increased substantially. ECR-P and ECR-E are similar for 60 and 80 wt% U-3F hybrids, but a jump in removal force (0.46 MPa) and energy (133 J/m^2) is observed for 3F-Si/H(U-3F-90).

The minimum for the ECR-P and ECR-E in the 40-50% U-3F range is an important and non-obvious result (Figure 5.13 and Table 5.2). ATR-IR results show an unexpected depletion of U-3F in the coating near surface (Figure 5.9). In a way that is not clear, hybrid coatings with 30-75% U-3F have depleted concentrations at the depth interrogated by ATR-IR with a Ge crystal (700 nm). From DSC, hard block phase separation is observed at the threshold concentration of 40-50 wt% U-3F. Hard block phase separation is coincident with compositions having increased strength (Figure S5.4, Table 5.1). Finally, wetting behavior determined by dynamic and static contact angle measurements (Figure 5.12, Table 5.2) fall in a narrow range fairly independent of composition.

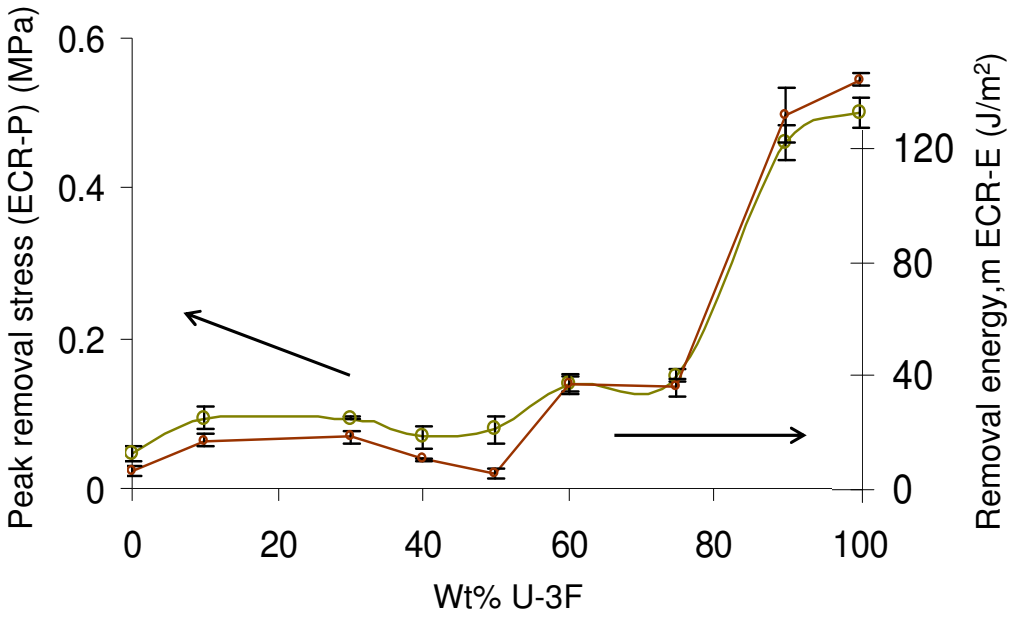

Figure 5.13. Peak removal force and removal energy has been plotted as a function of the weight percent of U-3F in the hybrid system.

This is consistent with an outermost surface composition dominated by the 3F soft block.

5.8. Conclusion

Characterization of hybrid coatings with 40-60% U-3F suggest that the near-surface compositional profile parallels the physical model for nanoscale, microscale, and mesoscale gradation for abhesive coatings based on figure 5.1. The combination of compositional and morphological features illustrated in figure 5.2 is suggested by contact angle measurements (A) and ATR-IR (B, C). Surprisingly good bulk mechanicals were confirmed by tensile and dynamic mechanical tests. Good adhesion to substrate (glass, aluminum) was not the subject of an engineering test. Qualitatively, coated aluminum panels were immersed in water and sea water followed by visual inspection. No sign of coating detachment was observed. Similarly, coated glass slides were immersed in water for several days without coating detachment.

The resistance to oil uptake is an important aspect of these fluorous hybrid coatings. Our results demonstrate that surface and bulk properties can be independently controlled through a hybrid coating formulation. The formulation scheme for this class of hybrid coatings offers a wide scope of compositions.

5.9. Supporting Information.

Figure S5.1. Image of crosslinked hybrid network coating 3F-Si/H(U-3F-40) demonstrating optical transparency.

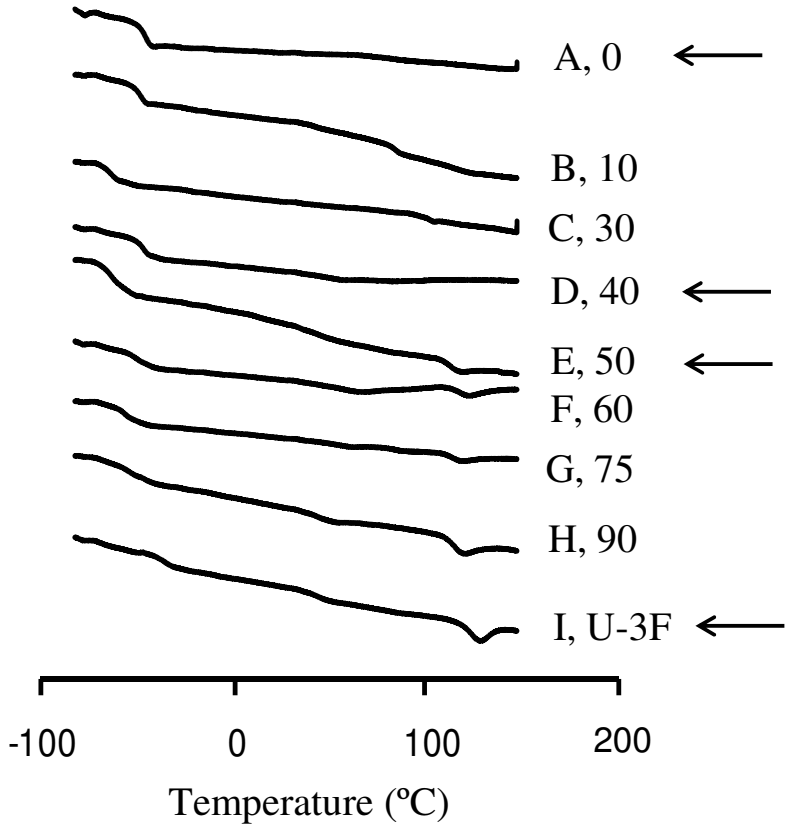

Figure S5.2. MDSC for 3F-Si/H-10-(U-3F-x) crosslinked hybrid networks with indicated wt% of U-3F.

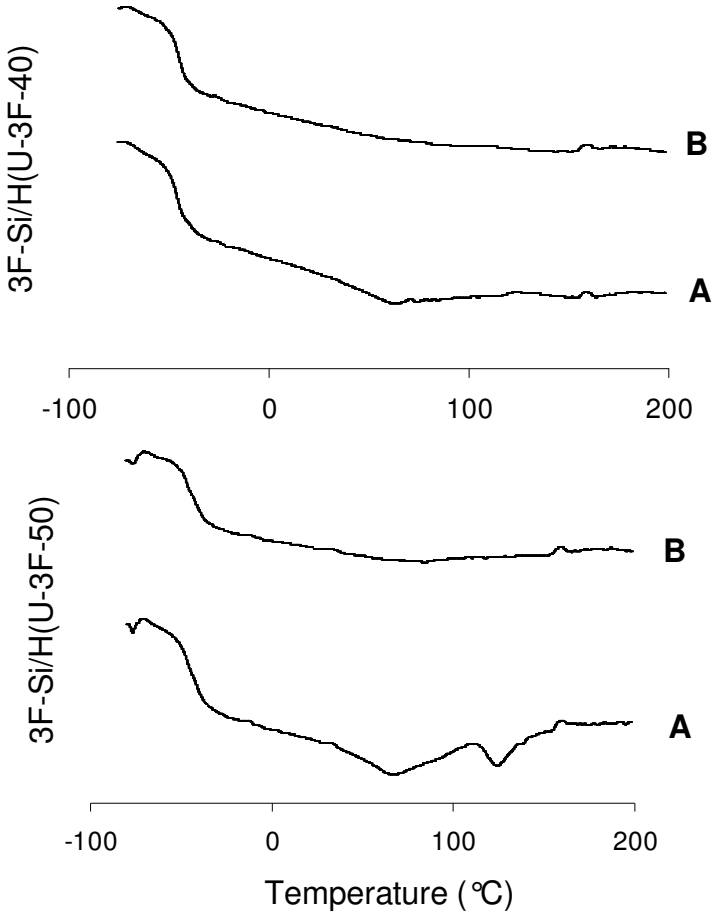

Figure S5.3. MDSC thermograms for 3F-Si/H(U-3F-40) and 3F-Si/H(U-3F-50), A – 1st heating cycle and B – 2nd heating cycle.

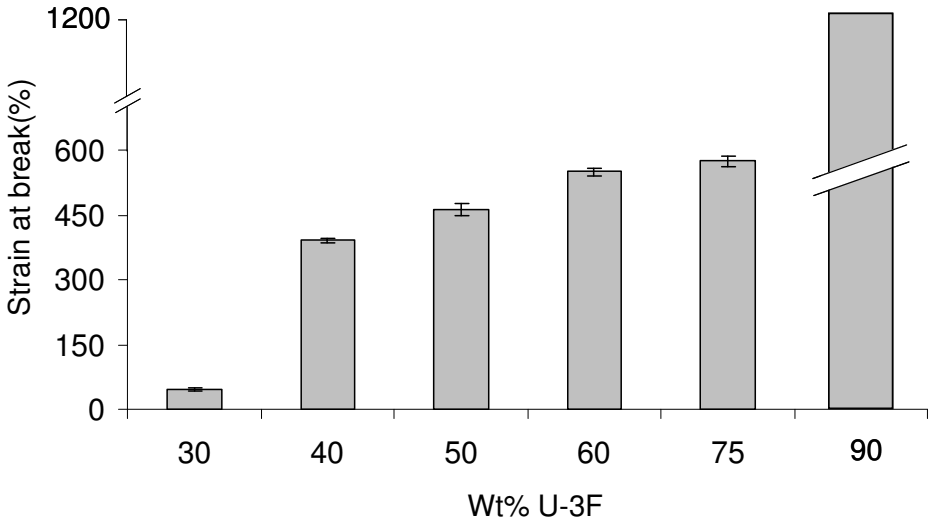

Figure S5.4. Strain at break as a function of wt% U-3F. The value for the neat U-3F (not shown) is similar to that for 3F-Si/H(U-3F-90)

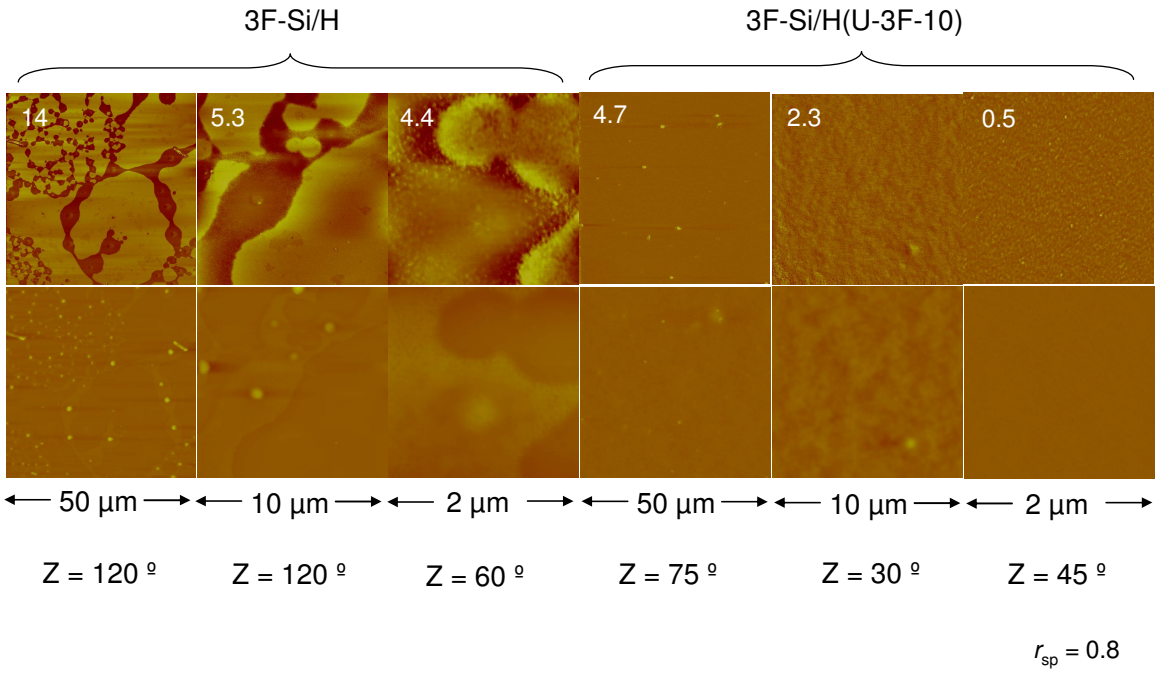

Figure S5.5. TM-AFM images for 3F-Si/H and 3F-Si/H(U-3F-10) coatings; upper, phase; lower 2D height with Rq at r_{sp} = 0.8.

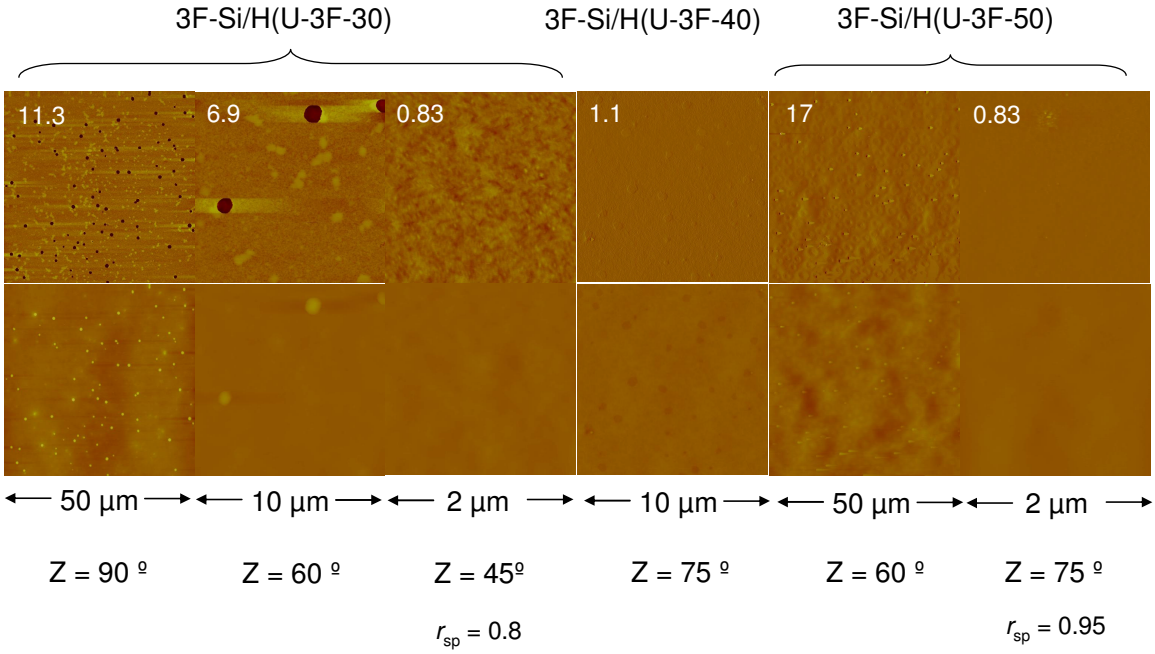

Figure S5.6. TM-AFM images for 3F-Si/H(U-3F-30), 3F-Si/H(U-3F-40) and 3F-Si/H(U-3F-50) coatings; upper, phase; lower 2D height with Rq.

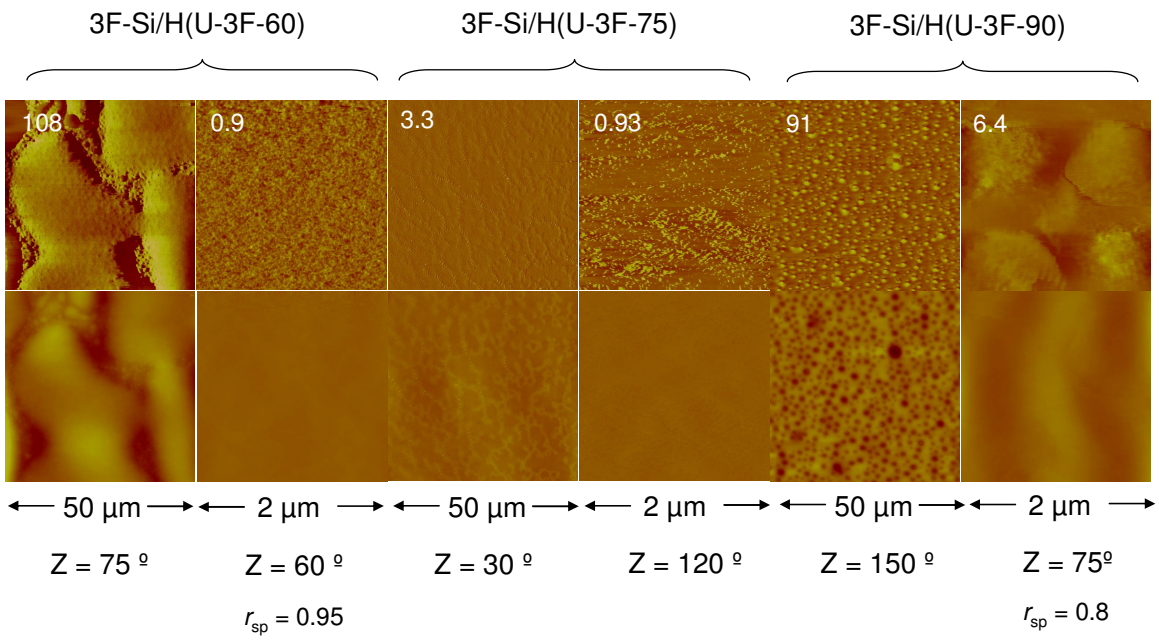

Figure S5.7. TM-AFM images for 3F-Si/H(U-3F-60), 3F-Si/H(U-3F-75) and 3F-Si/H(U-3F-90) coatings; upper, phase; lower 2D height with Rq.

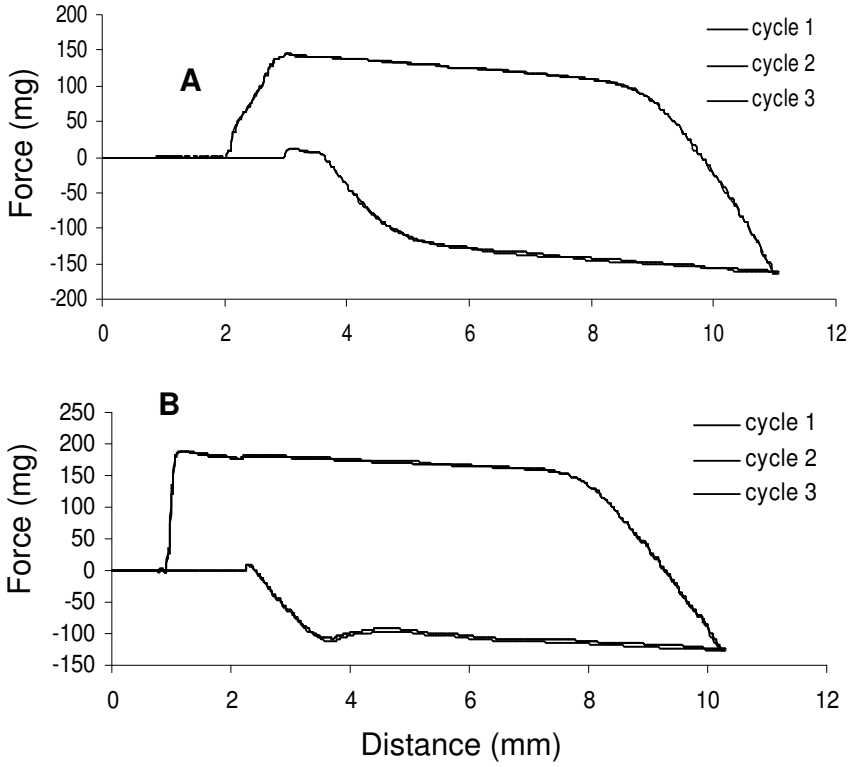

Figure S5.8. FDCs (3 cycles) for two representative compositions, **A**, 3F-Si/H and **B**, 3F-Si/H(U-3F-40). The advancing and receding contact angle values are listed in Table 5.2.

CHAPTER 6

Biocidal Polydimethylsiloxanes via cationic surface modifying additives

6.1. Introduction.

Infection acquired from health care environments is a major medical complication.[156] Studies have shown that ~ 6% of patients admitted to hospitals acquire infections during their course of treatment and over the years there is an increase in the number of such cases.[157] According to reports by the US Center of Disease Control (CDC), hospital acquired infections (HAIs) account for more than 2 million cases (2002) leading to 99,000 deaths annually.[158]

The most common hospital acquired infections (HAIs) include urinary tract infections,[159,160] surgical wound infections[161] and those associated with intravascular cannulas[162,163]. The mode of transmission of these infections is mostly by physical contact with infected medical devices. *Staphylococcus aureus*, *Pseudomonas aeruginosa* and *Escherichia coli* are the most common bacterial isolates giving rise to these infectious diseases.[164] Treatment of HAIs become more difficult since most of these bacterial strains develop resistance to antibiotics.[165-168] In a hospital environment it has been observed that over 50% of *Staphylococcus aureus* strains that cause surgical wound infection and catheter related sepsis,[169] develop resistance to common antibiotics like, methicillin and vancomycin.[170,171] Some of the emerging antibiotic resistant pathogens include vancomycin resistant *enterococci*[172], vancomycin intermediate *staphylococcus*[173] and multiple antibiotic resistant Gram (-) organisms such as acinetobacter, enterobacter and mycobacterium.[174,175]

Over the past two decades, studies have shown that naturally occurring peptides have an undiminished effectiveness against bacteria, fungi and viruses, thus challenging the notion of pathogenic resistance.[176] It has been observed that naturally occurring antimicrobial peptides (AMPs) provide the first line of defense against pathogen invasion.[176,177] These host defense peptides have a broad spectrum of antibacterial activity while being non-toxic to mammalian cells. AMPs have an α-helical[178] or β-sheeted[179] structure in solution, with a characteristic amphiphilic architecture. A general AMP architecture involves combination of hydrophilic (cationic) and neutral (hydrophobic) moieties, which impart an overall positive charge to the peptide chain.[180]

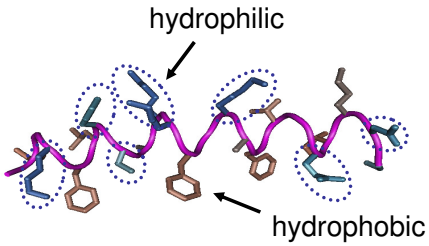

AMP

Some of the most common AMPs include Magainin-2[181], PGLa[182], Cecropin-P1[183] and Tachyplesin-1.[184] The charge to uncharged ratio of the repeat units vary between 0.2-0.3 for these peptide chains.[180,185] Antimicrobial activity is favored by binding of the cationic sites to the anionic lipopolysaccharide present in the microbial membrane. The *charge-charge* interaction is thought to be followed by insertion of the peptide chain into the bacterial membrane, which is facilitated by the hydrophobic moiety. Membrane disruption leads to an imbalance in cell osmotic potential causing cell lysis[186,187]. Various modes of peptide-membrane interaction, like the barrel stave, torroidal pore and the carpet models have also been studied recently.[188]

Structural cues from these naturally occurring antimicrobials led to widespread research over the past few decades in the field of synthetic antimicrobials.[189-194] Surfaces achieving microbial kill by the actual interaction of attached biocidal moieties with the membrane of the bacterial strain under investigation[195,196] was favored compared to release kill.[197,198] It was

observed that surfaces that affect bacterial kill by controlled release of the biocidal moiety, loses their activity after a certain period of time,[199] whereas, for contact kill coatings, the biocidal activity can be regenerated since there is no leaching out of the biocidal functional group from the surface. Contact kill biocides negate any unwanted side effects that may arise from the leaching of harmful substances as observed in release kill mechanism.

40 years ago, Isquith demonstrated highly effective antimicrobial coatings by chemically attaching an alkylammonium bearing trimethoxysilyl functional group to a glass surface.[200] A more recent study was done on non-leaching biocidal polyurethanes by Cooper, where the quaternary charge was incorporated in the chain extender, N,N-bis(2-hydroxyethyl)isonicotinamide (BIN).[195] Polymeric thin films employing contact kill was studied by Klibanov, employing the layer by layer (LBL) synthesis technique,[201] where a polycation (N,N-dodecyl, methyl-polyethylenimine) was layered with a polyanion to produce biocidal coatings. Some studies on polymeric nanofilms include coating textiles with alkylated polyethylenimine and coating polyethylene slides with silica, derivatized with poly(vinyl-N-hexylpyridinium) chains, tested against airborne pathogens. Antimicrobial activity of polymer brushes grown on inorganic surfaces by ATRP was also investigated.

A study on biocidal polyurethanes was done in the Wynne research group,[192] where a specialty polyurethane, HMDI/BD(30)-P(3FOx:C12)-(86:14) having an alkylammonium based semifluorinated soft block was used as a surface modifier for conventional HMDI/BD(50)-PTMO(1000) base polyurethane. Varying weight percents of the (3FOx:C12)-PU was solution blended with the base polyurethane to achieve surface concentration of the cationic moiety. It was observed that a 2 wt% of the (3FOx:C12)-PU surface modifier affected a 100% kill on bacterial strains of in 30 min.

Contact kill silicone coatings include a class of biocidal polysiloxanes with 3-(alkyldimethylammonium)propyl pendant groups. These polysiloxanes were synthesized by quaternization of n-octyldimethylamine or n-dodecyldimethylamine with linear polysiloxanes containing 3-chloropropyl groups and/or 3-bromopropyl groups attached to silicon atoms.[202] Another study investigated the antimicrobial activity of PDMS chains terminated with quaternary ammonium functionalities bearing oxyethylene moieties.[186] In a humid environment, these oxyethylene chains spread out, exposing the ammonium moieties which imparts biocidal property to these compounds. Simultaneously, cationic silicones have also been used as surface modifiers, one of them being a reactive silane, $(MeO)_3Si(CH_2)_3N^+Me_2C_{18}H_{37}Cl^-$ (DC 5700). This compound, developed by Dow Corning, renders bactericidal properties to surfaces like glass, cotton, polyester fibres.[203]

A recent study was done on poly(dimethylsiloxane) based coatings containing quaternary ammonium salt (QAS 1) moieties, exerting biocidal activity through contact kill. Condensation reaction was carried out on a silanol terminated PDMS (49 kDa) using methyltriacetoxysilane as the crosslinking agent. The quaternary ammonium salt contains trimethoxy end groups which also plays a role in the condensation process. Weight percent of QAS in the matrix was varied from 10-15% of the entire polymer. A maximum antimicrobial activity was obtained for the QAS 1 having a 14 carbon atom alkyl chain (R_1) extending from the cationic charge. A major point of concern about this study was the use of a high weight percent (10-15%) of the trimethoxy functionalized alkylammonium salt (QAS 1). A higher weight percent of the modifier would lead to a larger volume fraction of siliceous phase, which would have a greater tendency of binding to the

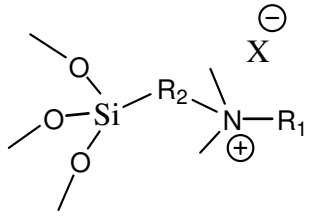

QAS 1

siliceous domain generated from the triacetoxy-condensation cure. Moreover, the presence of a trifunctionality at the modifier chain end would cause the QAS 1 to get trapped in the bulk of the polymer along with the crosslinking agent leading to surface depletion of quaternary charge. The moderate biocidal activity observed for these coatings suggest the presence of a substantial amount of the alkylammonium modifier QAS 1, in the bulk.

Gaining insights from prior works focusing on surface modification of PDMS, a new strategy has been developed for surface modification of PDMS with cationic moieties. The quaternary ammonium salt **3** that is the subject of study has a 12 carbon atom chain extending from the cationic charge. An alkyl chain of 12 carbon atoms was chosen for the present study based on a prior investigation done on modified HMDI/BD(50)-PTMO(1000) base polyurethane.[192] It was observed that having a 12 carbon atom alkylammonium side chain bearing semifluorinated polyurethane surface modifier affects 100% kill on strains of *P. aeruginosa*, *E. coli* and *S. aureus* in 30 min. The presence of a dimethoxy functional group is a major conceptual innovation compared to QAS 1, discussed in the earlier section. A difunctional alkoxy group would allow incorporation of the modifier in the linear polymer chain favoring surface concentration, prevent it from getting trapped in the bulk. The alkylammonium surface modifier being in the linear chain would have greater mobility and a tendency of concentrating at the surface. It has been seen from past studies that the side chains present in a linear polymer have a tendency to concentrate at the surface entropically.[192,204,205]

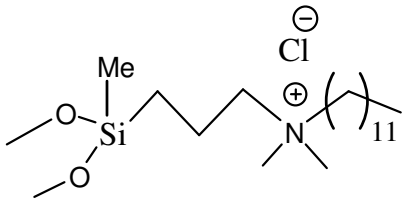

3

6.2. Experimental.

6.2.1. Materials. Hydroxyl terminated polydimethylsiloxane (DMS-S21, 90-120 cSt, 4 kDa), 3-chloropropylmethyldimethoxysilane (SIC 2355) and bis(triethoxysilyl)ethane (SIB 1817, BTESE) were purchased from Gelest Inc. N,N-dodecyldimethylamine (C12) and dibutyltin diacetate were obtained from Aldrich. Tetrahydrofuran, 99.6%, (for analysis ACS, stabilized with BHT) was obtained from Acros. Modified fumed silica nanoparticles (T-FSN, Cab-o-sil TS530 HMDZ treated fumed silica) having a BET surface area of 200 m^2/g was generously provided by Quantum Silicones, Midlothian, VA.

6.2.2. Quaternary ammonium modifier (QAM) Synthesis. With reference to Scheme 6.1, synthesizing the modifier involves a single step. A substitution reaction occurs between 3-chloropropylmethyldimethoxysilane 1 and N,N-dodecyldimethylamine 2 to incorporate the quaternary charge.

A typical precursor synthesis involves reacting 5g (27.4 mmol) of reactant 1 with 5.5g (25.8 mmol) of the tertiary amine 2 in a reaction vessel at 30 °C for 48 hrs. The reaction was carried out in the presence of ~ 25 ml of THF as a solvent. A constant purge of dry nitrogen was maintained inside the reaction vessel to eliminate the presence of any moisture since the methoxy functional groups present in 1 are susceptible to hydrolysis. The reaction of 1 with 2 provided the desired modifier 3 in quantitative yield. A complete substitution of the chlorine atom by the C12 tertiary amine was characterized by ^{1}H-NMR and FT-IR spectroscopy. The modifier was stored below room temperature inside a properly vacuum sealed container to prevent hydrolysis of the alkoxy functional groups.

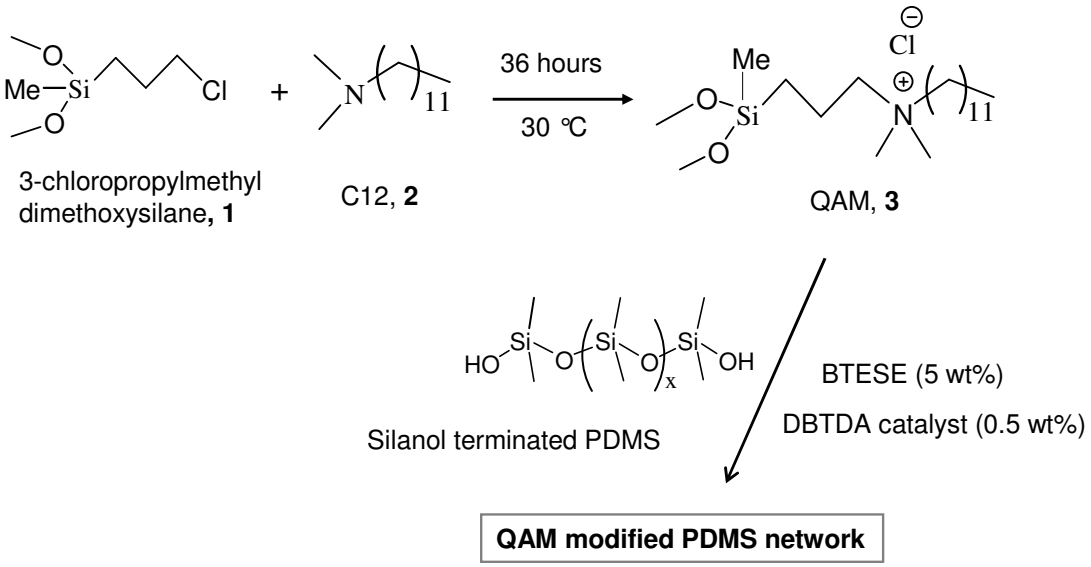

Scheme 6.1. Synthetic procedure for preparation of the quaternary ammonium modifier and a representative modified PDMS coating.

6.2.3. Coating preparation. Coatings were prepared on microscope slides by adding varying weight percents of the QAM to a silanol terminated PDMS following a condensation cure. PDMS coatings with 0.5%, 1% and 2% (by weight) of the modifier were prepared for further characterization. The modified coatings have been designated as P-x, where, 'P' stands for the 4 kDa poly(dimethylsiloxane) and 'x' refers to the wt% of the surface modifier incorporated in the coating. Preparation of a typical 0.5 wt% modified PDMS (P-0.5) coating involves adding 0.025g of the QAM 3 to 5g of a 4 kDa silanol terminated PDMS. The resin was mixed in a high shear equipment at 2700 rpm for 4 times at 60 seconds/cycle. A transparent, homogenous resin was obtained to which 0.25g (5 wt%) of the crosslinker, BTESE along with 0.5 wt% of DBTDA catalyst was added. The resulting resin was again mixed in a high shear equipment at 2700 rpm for 3 times at 60 seconds/cycle. Microscope slides were drip coated with the resin and was kept at ambient (~ 25 °C) overnight to initiate the formation of crosslinks. The condensation cure process was driven to completion by keeping the coated microscope slides at 100 °C for 24 hr. Plaques were formed by pouring the resin into PTFE plates and following the same curing technique (Scheme 6.2).

A representative PDMS coating reinforced with 10 wt% of fumed silica nanoparticles was synthesized to investigate the effect of adding fillers on surface and bulk properties. Treated fumed silica nanoparticles (0.5g, 10 wt%) was added to 5g of the 4 kDa poly(dimethylsiloxane) and mixed in a high shear equipment at 2700 rpm for 60 sec. The cycle was repeated for 4 more times to obtain a homogenous resin. The remaining process is identical to that described in the above paragraph. These samples are designated as PR-x, where 'PR' stands for reinforced PDMS and 'x' denotes the wt% modifier.

6.3. Instrumentation / Characterization.

6.3.1. Infrared spectroscopy. FT-IR spectra were obtained using a Nicolet 400 FT-IR spectrometer. A background spectrum was taken before running each sample and 32 scans were taken from 500 to 4000 cm-1. The spectra were analyzed using Omnic software.

6.3.2. NMR spectroscopy. ^{1}H-NMR (Varian Mercury 300, 283 MHz) spectra were used to qualitatively confirm the complete substitution of the chlorine atom from 1, followed by quaternisation. Spectrum for QAM samples dissolved in chloroform-*d* was obtained for 32 scans.

6.3.3. Streaming potential. Streaming potential of the control and the QAM modified coatings were measured using a clamping cell device. Coated microscope slides were clamped into the cell which was connected to the respective electrodes for measuring the potential difference across the channel. Electrolyte (1mM NaCl) was passed through the channel at 50 psi and the voltage generated across the channel was measured by a voltmeter.

6.3.4. Antimicrobial assay. Bacterial strains of *Pseudomonas aeruginosa* (PAO1), *Staphylococcus aureus* (ATCC-25904) and *Escherichia coli* (DH5α) were used for investigating the biocidal activity of P-0.5, P-1 and P-2 coatings. Condensation cured PDMS elastomer (P-0) was used as a control for this study. Bacterial cultures were streaked on Luria Agar plates from frozen stocks and incubated overnight at 37 °C. A single colony from each strain was used to inoculate 6 ml of Luria Broth (LB) and grown overnight at 37 °C, 225 rpm. A starting inoculum of 10^{8}-10^{9} colony forming units per milliliter (CFU/ml) of the desired pathogen was used for the culture. Aliquots from the overnight culture were taken and reinoculated in LB in a 1:100 dilution.

A biocidal test was devised to simulate aerosol deposition (cough, sneeze) of pathogenic bacteria. With a sprayer designed to deliver a controlled volume (or weight), a challenge of the

bacterial culture (~10^7 CFU/mL) was delivered to the surface of the coated samples. A constant weight of ~6 mg of the bacterial culture was sprayed on the coated microscope slides. The coated slides were placed in a humidified chamber (85-95%) environment, since a constant humidity is important because control experiments at ambient air showed irreproducible fractions of dead bacteria as a function of time. This step anticipates future studies for estimating kill kinetics. After 30 min residence time, the slides were placed in saline solution and vortexed for 2 min. An 100 µl aliquot and a 1:100 dilution were removed and spread onto agar plates that were incubated at 37 °C for 18 h. Live bacteria (cfu's) on plates were counted to obtain the percent kill and log reduction. The same protocol was followed for microscope slides coated with conventional condensation cured PDMS that served as a control for this study. Kinetics of kill was determined by altering the residence time to 15 and 45 min.

6.3.5. Mechanical test. For tensile testing, samples were stamped out of cast plaques, which were measured for thickness, width and gauge prior to mounting in the RSA III tensile clamps. Data acquisition rate was 1 Hz while the initial sample elongation rate was 10 mm/min. The maximum elongation at break was determined for different samples.

6.4. Results and Discussion.

6.4.1. Quaternary ammonium modifier (QAM) synthesis. The QAM was synthesized by following a substitution reaction between 3-chloropropylmethyldimethoxysilane 1 and N,N-dodecyldimethylamine 2 leading to quaternization of the ammonium moiety. The presence of alkoxy functional groups in 1 increases its susceptibility towards hydrolysis. As a preventive measure, both inner and outer walls of the reaction vessel were properly flamed to eliminate the presence of any adhered water molecules.

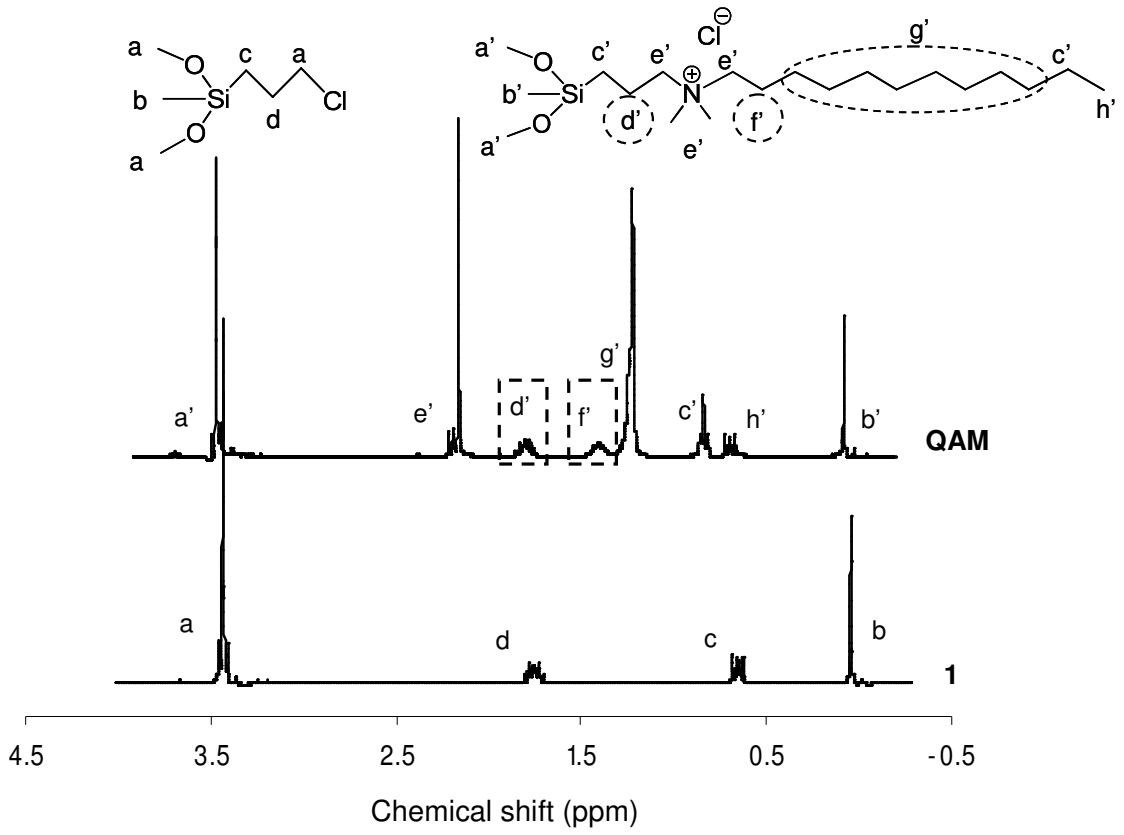

Figure 6.1. ^{1}H-NMR spectra for reactant 1 and the quaternary ammonium modifier (QAM) showing complete substitution by the tertiary amine.

The reaction was carried out in a moisture controlled environment by having a continuous supply of dry nitrogen through the reaction vessel. Generally, a quaternisation reaction is performed at higher temperatures (~ 60 ºC), but this reaction was carried out at a temperature close to ambient (~ 30 ºC) in order to protect the methoxy groups from hydrolysis.

Formation of the quaternary ammonium modifier was monitored by ^{1}H-NMR and IR spectroscopic analysis. Figure 6.1 shows the NMR spectra for reactant 1 and the QAM. Signature peaks in both the reactant 1 and the QAM helps us in qualitatively and quantitatively determining the extent of substitution. It can be observed from figure 6.1 that the H atoms attached to the α carbons adjacent to the quaternary nitrogen (-C**H**$_2$NC**H**$_2$-) and the –C**H**$_3$ groups attached to the quaternary nitrogen in the QAM gives a chemical shift at ~ 2.3 ppm, designated as peak e'. The H atoms attached to the carbon at the β positions from the quaternary nitrogen (-CH$_2$C**H**$_2$CH$_2$N-, d') and (-NCH$_2$C**H**$_2$CH$_2$-, f') gives a chemical shift at 1.8 ppm and 1.6 ppm respectively. Ratio of the integrated peak areas corresponding to d' and f' (9.23/9.08) gives a value of 1.01, which correlates with the ratio of the number of H atoms.

FTIR was done on both the 3-chloropropylmethyldimethoxysilane 1 and the QAM to ensure substitution of the chlorine atom by C12 amine (Figure S6.1). It is observed that 1 has a broad C-Cl absorption peak at ~ 800 cm^{-1}, whereas the same peak is absent in the spectrum for the QAM. The above analyses confirms both qualitatively and quantitatively a complete substitution of the chlorine atom in 1 by the tertiary amine.

6.4.2. Coating preparation. As shown in Scheme 6.2, coating preparation involved condensation cure reaction between: (1) PDMS and QAM, (2) PDMS and BTESE (crosslinking agent) and between BTESE moieties themselves. Very minute traces of the modifier (0.5%, 1% and 2%, by weight) were used in the coatings. Scheme 6.2 demonstrates a condensation cure technique,

where water is both a reactant and a product. The surface modifier was physically mixed with the hydroxyl terminated PDMS, which ensured incorporation of the modifier in the linear siloxane chain due to its difunctional methoxy groups. To further facilitate formation of crosslinks, an additional amount of BTESE (5 wt%) was added. Condensation reaction proceeds in the presence of trace amounts of catalyst, DBTDA (0.5 wt%) to form a slightly viscous resin. Microscope slides were drip coated and kept in the ambient overnight to initiate the formation of crosslinks. Finally, the condensation reaction was driven to completion by placing the slides at 100 ºC for 24 hour. The resultant coatings were optically transparent.

6.4.3. Streaming potential. The basic principle behind this technique is that the presence of heterogeneity at a coating surface would generate a potential difference which can be quantified by the streaming potential (SP) measurements. In this process, an electrolyte of a given concentration is passed through a channel created over a surface by applying a pressure drop (ΔP).

The presence of a charge on the surface induces an equal but opposite charge on the adjacent fluid. A net zero current in the cross sectional area of the slit induces a potential difference which is measured by electrodes present at the two poles. Drawing analogy to this concept, a surface concentrated with cationic charge would generate a SP value greater than an uncharged/neutral surface.

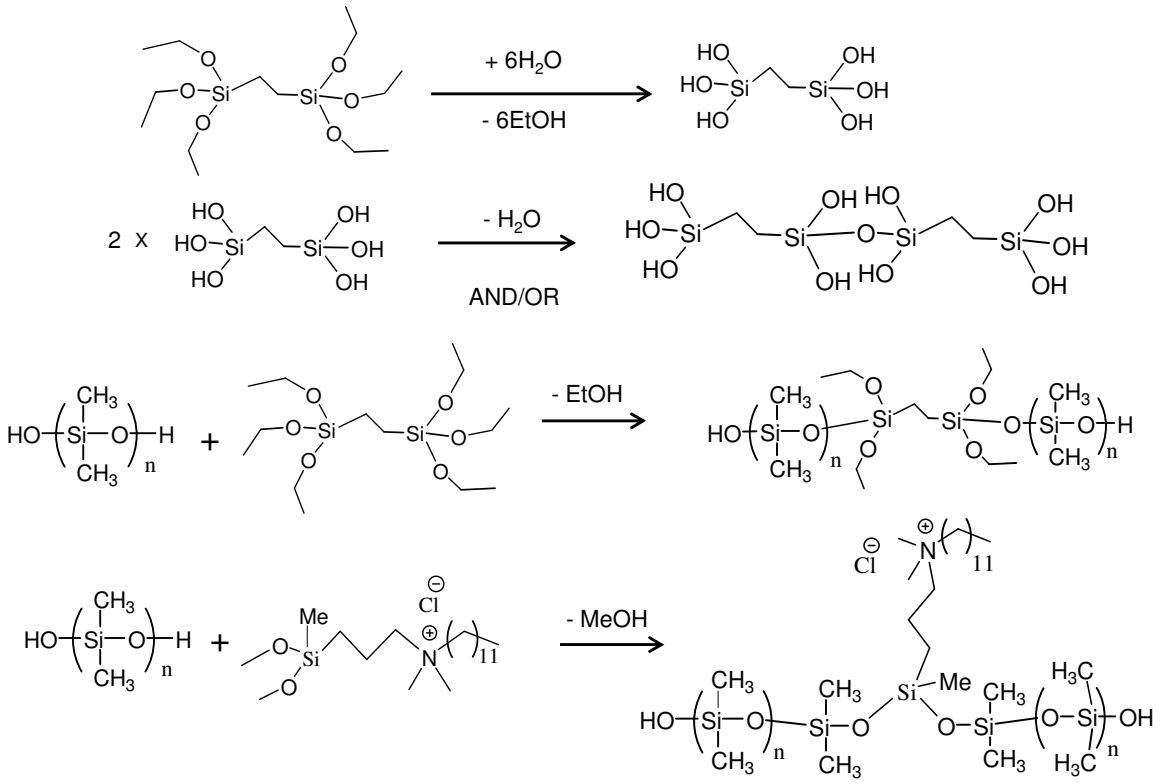

Scheme 6.2. Typical condensation reactions occurring between PDMS, crosslinking agent and the surface modifier.

Quantification of accessible quaternary charge is vital in understanding biocidal effectiveness. Results from the streaming potential experiments will be correlated with the biocidal activity obtained from the antimicrobial tests. The dependency of surface concentration of quaternary charge on weight percent of the alkylammonium modifier has been investigated in an earlier study by measuring the SP of polyurethane surfaces modified by a quaternary ammonium moiety. It was observed that an as-cast HMDI/BD(30)-P[(3FOx)(C12)-(87:13)] polyurethane gave a SP value of 174 mV, whereas, an annealed sample had a SP value of 223 mV. It is expected that a conventional HMDI/BD(30)-PTMO-1000 polyurethane modified with 1 wt% of the fluorinated alkylammonium bearing PU, would have a lesser concentration of cationic charge at the surface. As per expectation, a 1 wt% modified base PU coating gave a SP value of 93 mV.[204]

$$\zeta = \frac{\frac{\Delta E}{\Delta P}\eta\kappa}{\varepsilon\varepsilon_o} \qquad \text{Eq. 6.1}$$

Another study investigated the surface charge on ion conductive sulfonated poly(sulfone) membranes for aqueous applications.[206] Coatings were prepared with degrees of sulfonation (DS) varying from 0.26 to 1.28, followed treatment with 0.5M sulphuric acid to protonate the sulfonated groups. Potential measurements were made with 1mM KCl solution. It was observed that at a particular pH (5), the zeta potential increased from -60mV (DS = 0.46) to -5mV (DS = 1.28). The trend observed for zeta potential values can be correlated to streaming potentials, since these parameters share a direct proportionality (Helmholtz Schmoluchowsky equation, Eq. 6.1).[207]

Hence, from the above results it is evident that the streaming potential of any charge bearing polymer coating is a function of the surface accessible quaternary charge. Increasing weight percent of the surface modifier would lead to an increased surface concentration of

quaternary charge, which can be quantified through streaming potential measurements. Streaming potential measurements would also give insights regarding the concentration of surface modifier needed to achieve optimum biocidal activity by surface concentration of quaternary charges.

In the current study, SP measurements were done on P-0, P-0.5, P-1, P-2 and the PR-1 coatings. Streaming potential on condensation cured PDMS elastomer served as a control for this study. Figure 6.2 shows the streaming potentials of the respective coatings. It has been observed that the PDMS control had the least SP, which increased with incorporation of a small amount (0.5%) of the surface modifier. The normalized SP values have been plotted in figure 6.2 which emphasizes the phenomena that surface heterogeneity increases with an increase in the concentration of the quaternary surface modifier.

The SP increases from 14 mV (0.5%) to 86 mV (1%), which further reinforces our hypothesis that increasing the amount of surface modifier would lead to a greater tendency of surface concentration. P-1 coating gave a SP of 36 mV whereas; when the coatings were reinforced with treated fumed silica nanoparticles, the SP decreased to 21 mV. A detailed explanation for this observation is given in the succeeding sections.

It is postulated that the alkyl side chain bearing a cationic charge would be entropically driven to the surface of the polymer. This entropic driving force stems from the solubility parameter mismatch between the QAM and PDMS (7.3 $(cal/cm^3)^{1/2}$) and also due to the fact that the cationic charge would be incompatible with the silicone matrix. Hence, surface concentration of cationic groups would confer antimicrobial property to the PDMS coating and lead to surface heterogeneity.

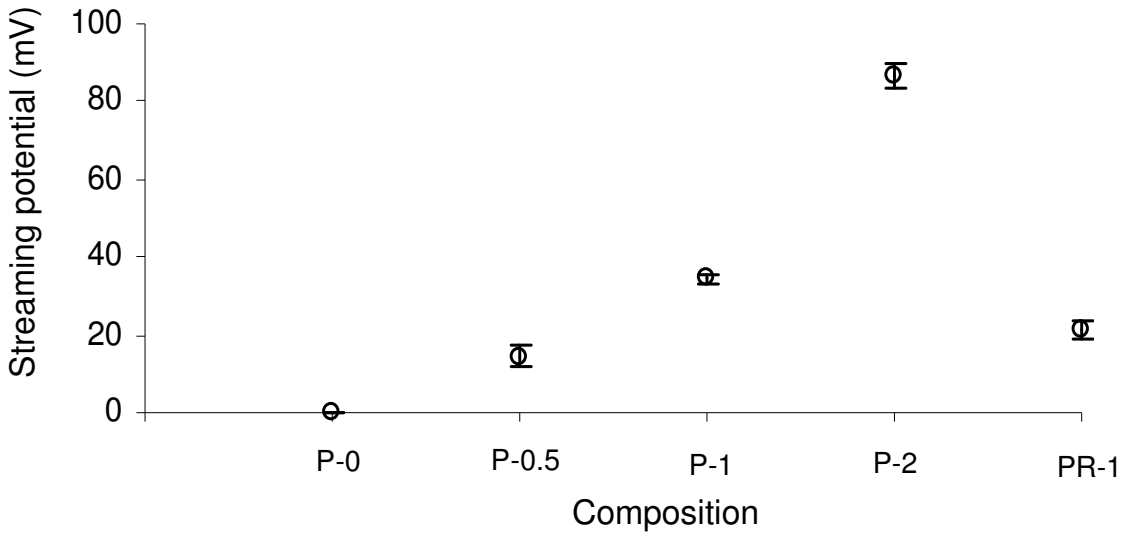

Figure 6.2. Streaming potential of the modified PDMS coatings and the control.

This above hypothesis is confirmed from streaming potential measurements where an increase in the amount of the quaternary surface modifier has led to an increase in positive potential at the surface (Figure 6.2).

6.4.4. Antimicrobial assay. Having established the presence of positive charges at the polymer-air interface, the antimicrobial activity of these coatings was investigated against both Gram positive and Gram negative strains of bacteria. Antimicrobial activity of the modified samples was tested for a residence time of 30 min. As compared to the control (P-0) which had 118 and 331 cfu for *S. aureus* and *P. aeruginosa* respectively, P-0.5 showed some biocidal activity by affecting 68% kill against *S. aureus* and 75% against *P. aeruginosa* in 30 min. Increasing the amount of surface modifier to 1% (for P-1) led to an enhancement in biocidal activity to 99.5% (*SA*), 99.6% (*PA*) and 98% (*EC*) as seen in figure 6.3. Within experimental errors, the same extent of bacterial kill was achieved on increasing the amount of QAM to 2% (P-2).

Log reductions in bacterial colony forming units follow the same trend, with the P-1 having comparatively higher values than P-2 for all three strains (Figure 6.3). The biocidal test result complies well with the observed streaming potential measurements, where P-2 > P-1 > P-0.5 > P-0. It is postulated that increasing the weight percent of the quaternary ammonium surface modifier would lead to an increase in the fraction of cationic groups at the surface which would translate to an enhanced biocidal activity. It has been shown in previous studies with polymer compositions having different surface modifiers that an increase in the amount of modifier correlates with increased kill/unit time.[208] A prior study on a polyurethane surface modifier containing semifluorinated and hydantoin side chains has shown the dependence of antimicrobial activity on modifier concentration.

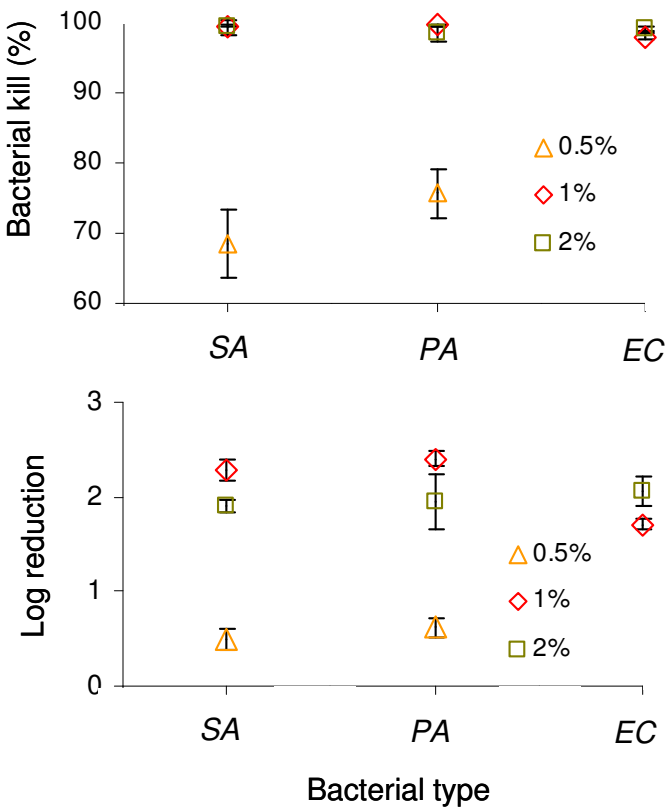

Figure 6.3. Percent kill and log reduction of affected by the modified PDMS coatings against the given bacterial strains. $R^2 > 0.96$

It was observed that there is an enhancement in antimicrobial activity on increasing the weight percent of modifier from 0.4% to 1.6% after which the activity stabilizes.[208] The same phenomena has been observed in the present study, where the biocidal activity increased from P-0.5 to P-1 whereas, increasing the concentration of the surface modifier from 1% to 2% (P-2) affects the same extent of bacterial kill (Figure 6.3). Figures 6.2 and 6.3 demonstrates that an optimum biocidal activity is achieved at a modifier concentration of 1% (P-1), after which the antimicrobial effectiveness stabilizes even though there is an increase in the surface charge density.

Figure S6.2 shows the remnant number of bacterial CFUs from antimicrobial assays performed on different modified coatings and the control. It was observed from a past study by Isquith that a surface coated with a quaternised silane exhibits a more pronounced antimicrobial activity compared to a surface coated with just a QAC. The kill kinetics was also measured for these contact kill biocidal surfaces and it was observed that for an exposure time ≥ 45 mins, > 99% kill was obtained against a strain of *E. coli*.[209]

An investigation of the antimicrobial activity of MDI/BIN/PTMO polyurethanes was performed where the hard block segments were quaternised with a C8, C18 and a CF halide to incorporate the cationic charge.[195] Antimicrobial efficacy of the polyurethanes increased with the mol% hard segment (25 to 38% HS), with the C18 being the most effective against a strain of *S. aureus* (~ 95% kill) in 30 min. These coatings showed negligible activity against *E. coli*, with the C18-PU affecting 10% kill over 30 min. A major shortcoming in this study was that the quaternised polyurethanes absorbed water ranging from 23 to 49% by weight.

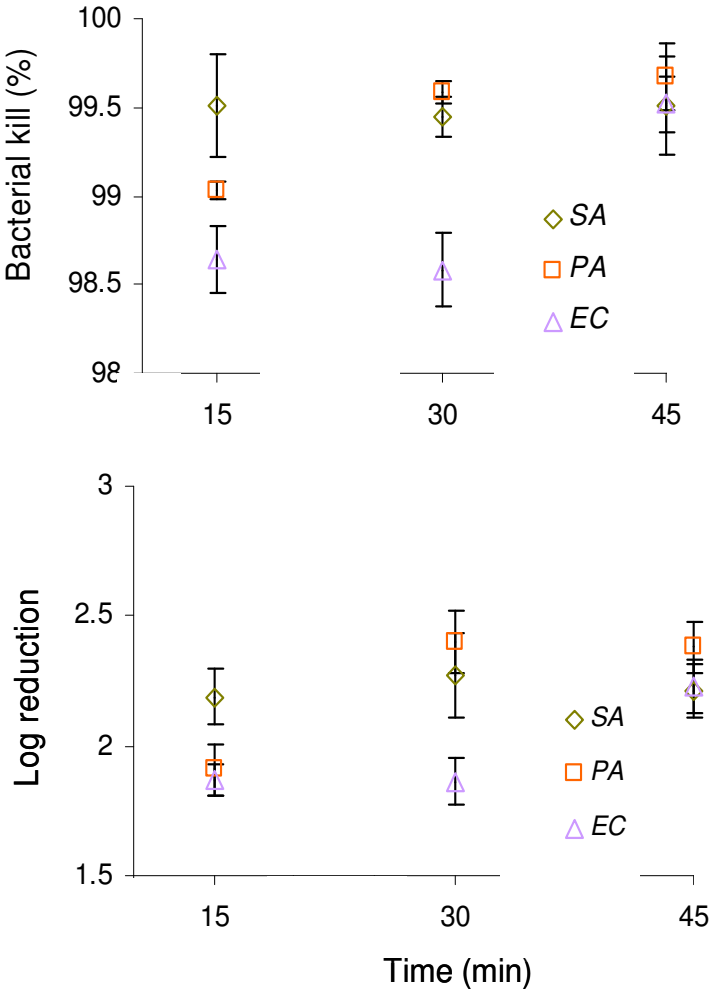

Figure 6.4. Percent kill and log reduction of a PDMS coating modified with 1 wt% of QAM, as a function of time. $R^2 > 0.94$

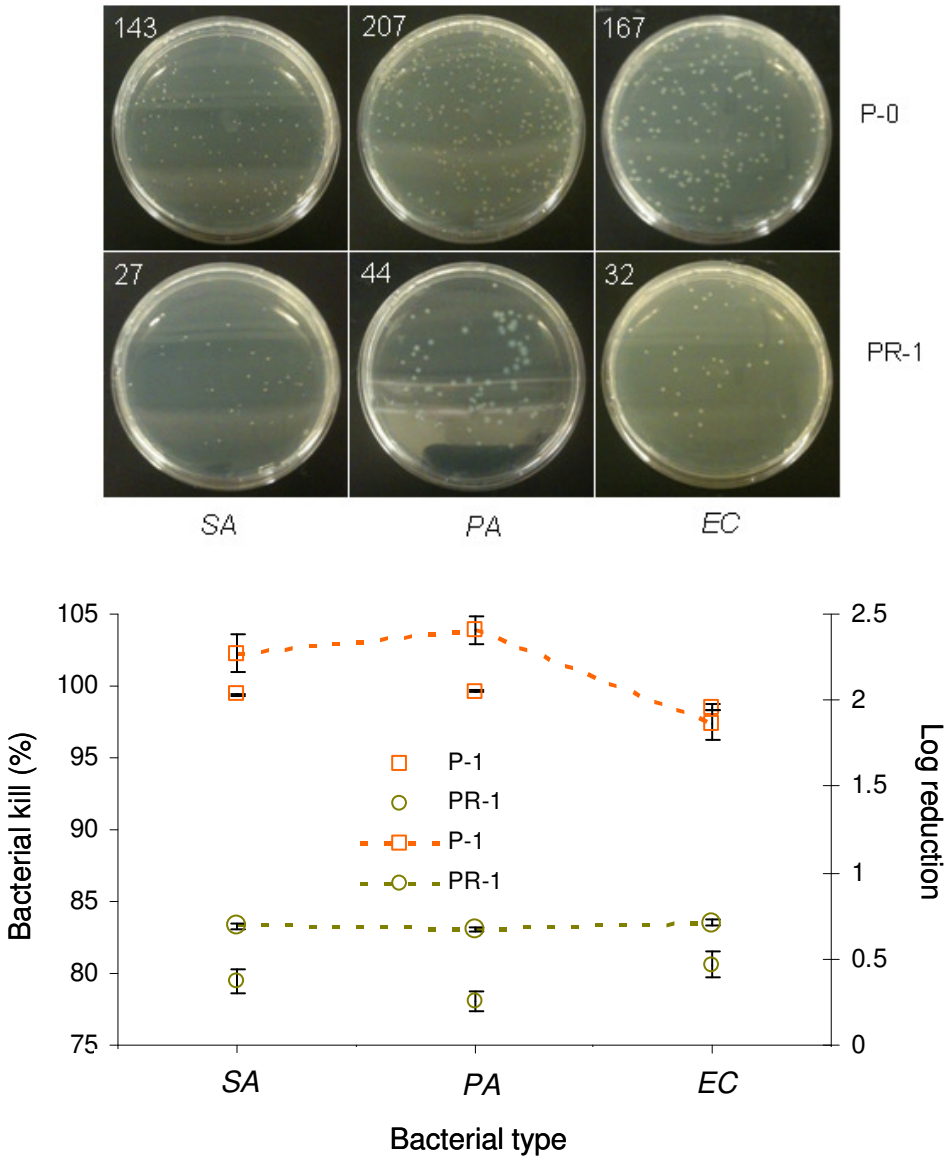

Figure 6.5. (Top)-Biocidal test results with a control and the filled PDMS coating (1% modified), showing the remnant number of cfu. (Bottom)-Comparison of biocidal activity (% kill and log reduction in bacterial cfu) between an unfilled and filled PDMS sample modified with 1 wt% of the QAM.

An investigation of the antimicrobial activity of thin films prepared by layer by layer (LBL) technology demonstrated their effectiveness against the tested bacterial strains at a pH of 3.0, affecting > 95% kill.[201] Although an optimum combination of the polycation and polyanion confers excellent biocidal activity to the films, a decreased effectiveness to < 50% at neutral pH is a cause of concern. Furthermore, these ultrathin films of ~ 10 nm thickness would have poor mechanical strength; hence translation to practical applications would be difficult. The presence of a quaternary charge in the surface modifier that is the subject of investigation eliminates pH dependence of charge concentration.

Kill kinetic assay was performed in order to determine the dependence of biocidal activity on residence time. It was observed that a representative P-1 coating affected > 99% kill on strains of *SA*, *PA* and *EC* in the first 15 min (Figure 6.4). The P-1 coatings show remarkable biocidal activity as compared to the quaternised silanes which reach a 99% kill for a time > 45 min.[209] Remnant number of bacterial CFUs after the kill kinetic assay are shown in figure S6.3.

Antimicrobial tests were also performed on the filled PDMS sample modified with 1 wt% of the QAM. It was observed that the biocidal activity of the 1 wt% modified PDMS sample decreased on adding fillers (10 wt% FSN) (Figure S6.2). The percent kill ranges from 78% (*PA*) to 81% (*EC*), which is ~20% less than the unfilled sample and there was a decrease in the log reduction by a factor of 3 (Figure 6.5). Surface modification of silica nanoparticles by condensation reactions with different alkoxy bearing compounds is a common practice.[210,211] A past study has shown surface modification of silica nanoparticles by condensation reaction between the hydroxyl groups on the nanoparticle surface and the methoxy groups in benzyl alcohol.[212] Following this route, it can be hypothesized that a similar kind of condensation reaction occurs between the hydroxyl moieties at the surface of silica nanoparticles and the

methoxy functional groups present in the QAM. This leads to FSN surface modification and subsequent internalization of the quaternary charge, rendering the surface with a lesser concentration of cationic charge. A diminution in biocidal activity and a decrease in the streaming potential of the modified coating are observed. Treating silica nanoparticles with hexamethyldisilazane incorporates a trimethylsilyl group at the surface, facilitating good particle dispersion.[213] It has been observed from prior studies that in the process of silylation, a certain fraction of nanoparticle surface remains unmodified.

From the present result it can be postulated that for PR-1 (filled PDMS), a condensation reaction takes place at the surface of the nanoparticle between fractions of remnant hydroxyl groups and the methoxy groups of the modifier. Immobilization of the modifier at the nanoparticle surface leads to internalization and their concentration at the surface of the coating would diminish.

6.4.5. Mechanical property. Polydimethylsiloxane elastomers are well known for their low glass transition temperatures (T_g ~ -120 ºC) and high thermal stability (~ 250 ºC).[28] One characteristic that limits the application of these elastomers is their weak mechanical property[15-17] and they require reinforcement.[18] Some of the most common techniques of reinforcing silicones involve using silica, ceramic and zeolite nanoparticles in making a nanocomposite blend.[24-27] Silica nanoparticle fillers have been the subject of study over the past few decades.[20-23] The basic idea of incorporating nanoparticles in this study is to enhance the mechanical strength of the modified coatings with unhindered antimicrobial activity. It has been observed from past studies that nanocomposites made from unmodified silica nanoparticles have poor mechanical properties due to improper dispersion of the filler in the polymer matrix and partly due to adsorption at the polymer-filler interface.[211,214]

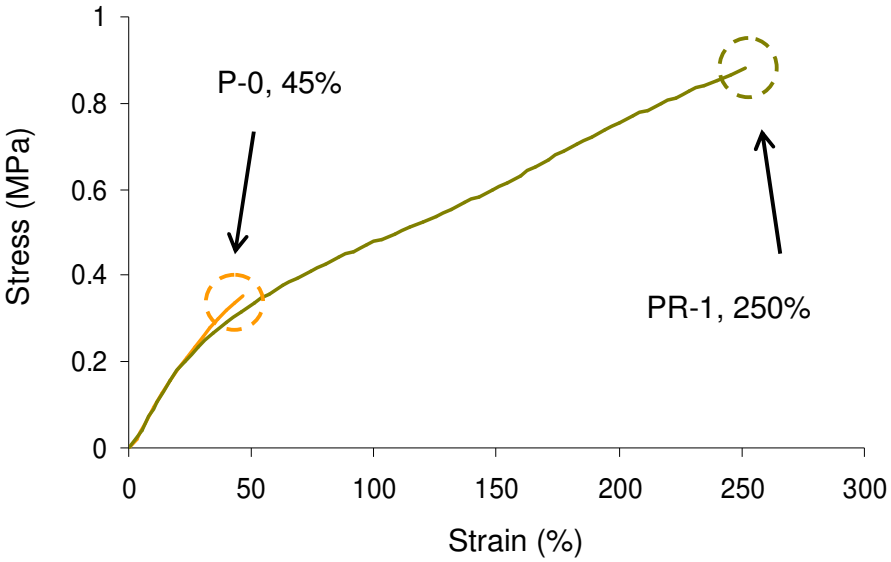

Figure 6.6. Stress vs strain curves for determining the maximum elongation at break for an unfilled and filled PDMS coating modified with 1 wt% of the QAM (P-1).

The above issue can be addressed by surface modification of the filler with a suitable modifier. Hence, fumed silica nanoparticles (FSN) treated with hexamethyldisilazane was used as filler for the present study.[213] Tensile tests were done on an unfilled PDMS sample with 1 wt% of the QAM was (control) and a sample filled with 10 wt% of the treated FSN. The unfilled sample had a tensile behavior similar to a PDMS elastomer, with a maximum elongation of 45% at break. The filled sample underwent 250% elongation before break (Figure 6.6).

6.5. Conclusion.

The present study has shown a new route for synthesizing thermosetting siloxane-based elastomers having antimicrobial activity. Very trace amounts (0.5, 1 and 2 wt%) of a surface modifier has been added to a PDMS matrix, following a condensation reaction to concentrate positive quaternary charges at the coating surface. Streaming potential (SP), an effective engineering technique has been utilized in this study to quantify the surface accessible quaternary charge in the modified coatings. Streaming potential measurements have shown a modifier concentration dependant charge density, with the SP increasing from P-0 (unmodified control) to P-2. Antimicrobial assays have demonstrated remarkable biocidal activity for the P-1 and P-2 coatings against strains of *S. aureus*, *P. aeruginosa* and *E. coli*, achieving >99% kill in 30 min. Kinetics of kill was investigated for the P-1 coatings, where they were observed to affect >99% kill in the first 15 min. Weak mechanical property of PDMS led to reinforcing a representative P-1 coating with 10 wt% of treated fumed silica nanoparticles. An improvement in tensile property was observed with an increase in elongation at break from 45% (P-1) to 250% (PR-1). Adsorption of the modifier at the nanoparticle surface led to internalization and a

decrease in surface potential and biocidal activity. Biocompatibility of PDMS combined with antimicrobial activity would offer immense potential for their use in biomedical applications.

6.6. Supporting Information

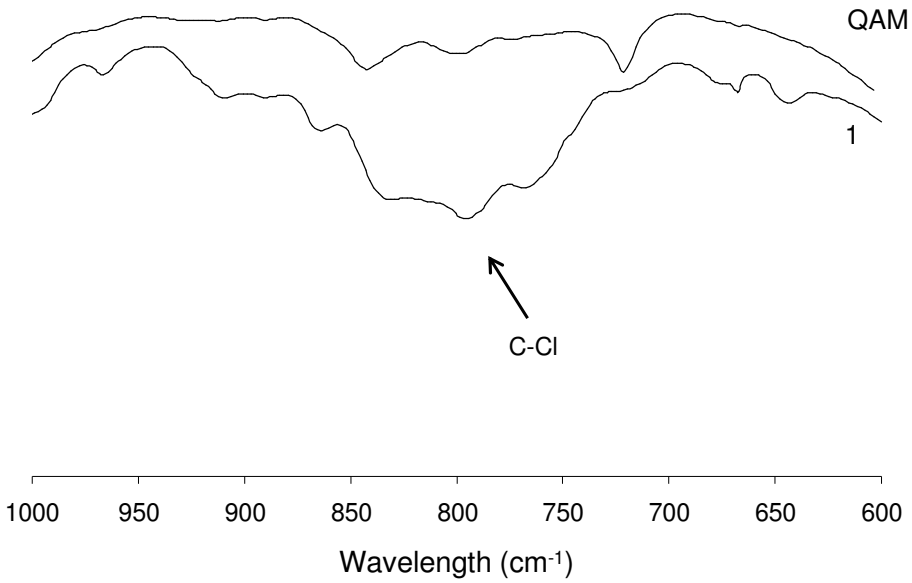

Figure S6.1. FTIR spectra for reactant 1 and the surface modifier (QAM) showing the disappearance of the C-Cl peak, confirming complete substitution.

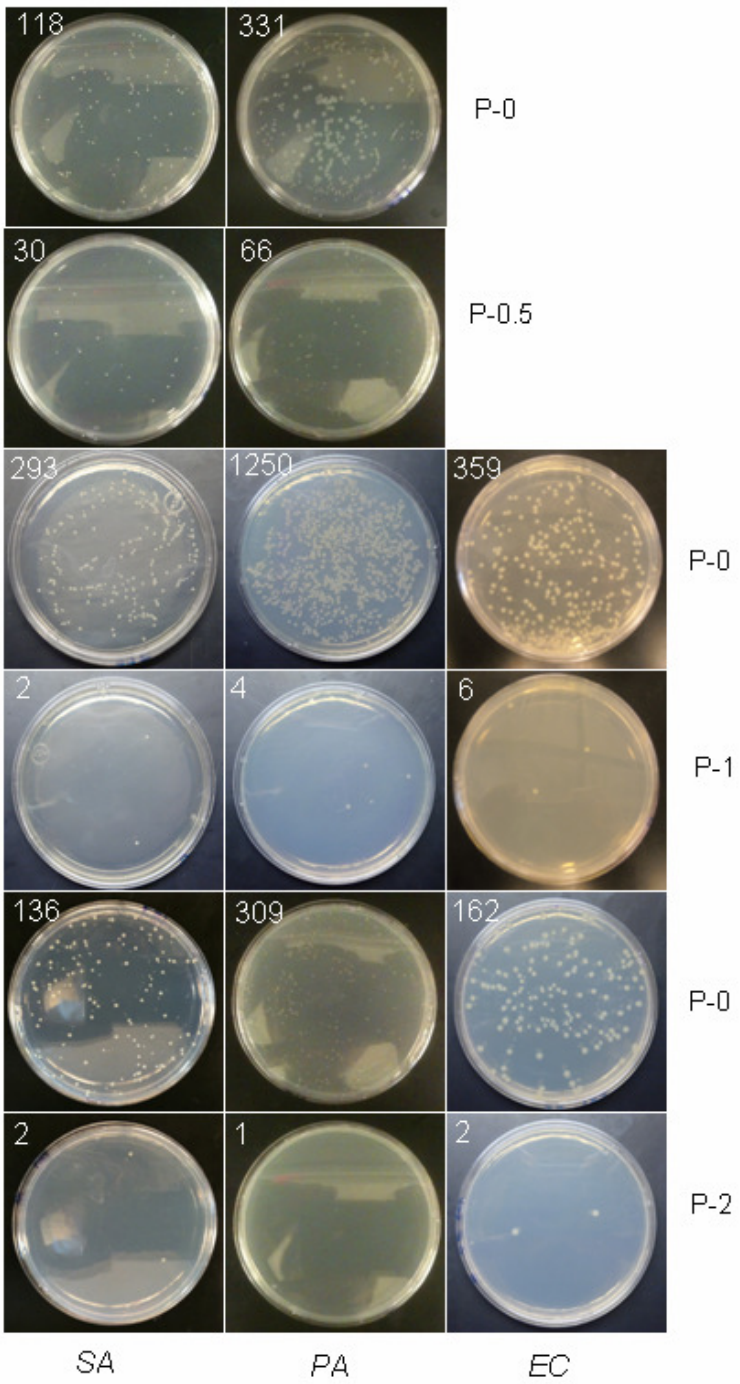

Figure S6.2. Representative biocidal test results showing the number of remnant CFU in the control and in the modified PDMS coatings.

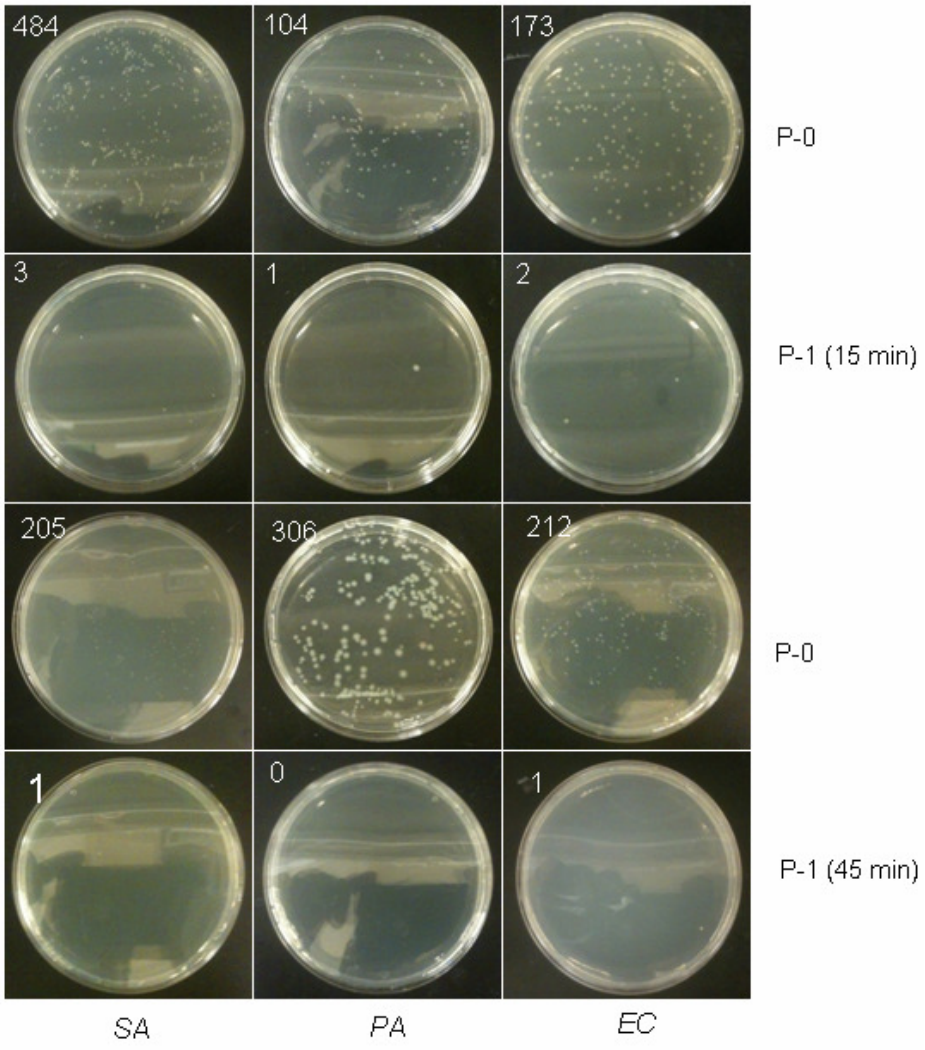

Figure S6.3. Results from the antimicrobial assay with residence time of 15 and 45 min, demonstrating time dependant biocidal activity.

CHAPTER 7

Further Exploration

Interesting surface and bulk morphology of some specialty soft surfaces have been discussed in the preceding chapters. Novel routes for generating elastomeric materials towards targeted applications have been the focus of this study. Although a detailed study on synthesis, characterization and an in depth investigation of the observed / expected properties have been elucidated, yet these studies entail further exploration some of which have been discussed in the subsequent section.

7.1. PDMS nanocomposites. Past studies have shown polydimethylsiloxane to be used as scaffolds for cell adhesion and growth.[215,216] It has also been observed that the surface modulus of scaffolds drive stem cell differentiation.[217,218] The present study on PDMS nanocomposites demonstrate a near surface concentration of untreated fumed silica nanoparticles dependant on the siliceous volume fraction. This phenomenon would translate to a gradient in surface modulus with siliceous domain concentration. Performing growth assays on human dermal cells and investigating the effect of nanoparticle induced surface modulus on stem cell differentiation.

7.2. Reactive triblock copolymers. A new route for reinforcing soft materials as evident from this study is noteworthy. The triblock architecture offers immense scope for alterations in the synthetic chemistry. Methylene bis(cyclohexyl)isocyanate (MDI) is known to have higher crystallinity compared to HMDI. Synthesizing the triblock copolymers using MDI as the diisocyanate is expected to impart better mechanical strength due to stronger hydrogen bonding

between the hard segments. Intuitively, a still lower wt% of the hard segment would impart equivalent or better mechanical strength to the elastomer.

It has been observed that the presence of the fluorous domain initiates phase separation that facilitates hydrogen bonding between the hard segments. A systematic study could be done by increasing the length of the fluorous side chain (number of monomer repeat units being constant) that would lead to interesting morphology, both in the bulk and at the surface.

7.3. Polyurethane hybrid elastomers. A novel concept was elucidated for synthesizing stratified polyurethane, having a soft (low modulus) near surface connected to a tough bulk polyurethane. It has been observed that the fluorous polyoxetane, which acts as a soft segment, dominates the surface of the hybrid elastomers. It would be interesting to observe the change in release characteristic that the hybrid would exhibit on increasing the length of the fluorinated side chain of the polyoxetane.

The specialty polyurethane that was used in this study could be replaced by a commodity base polymer, like an HMDI/BD(30)-PTMO(1000), which would also be cost efficient. The specialty polyurethane used in this study had a soft block miscibility with the polyoxetane soft domain. Incorporating a more polar soft segment polyurethane in the hybrids would give rise to different surface morphology that would impact the fouling release nature of these coatings.

7.4. Antimicrobial silicones. As described in this study, incorporating a difunctional alkylated quaternary ammonium surface modifier has imparted excellent biocidal activity to a conventional polydimethylsiloxane. A 12 carbon atom alkyl chain was used in the surface modifier based on prior results with antimicrobial polyurethanes. A past study has shown good biocidal activity for alkyl chain ranging from C8 to C18. Hence, a systematic study of antimicrobial activity as a function of the alkyl chain length could be performed.

REFERENCES

(1) Ogoshi, T.; Itoh, H.; Kim, K. M.; Chujo, Y. *Macromolecules* **2002**, *35*, 334-338.

(2) Gilman, J. W.; Kashiwagi, T.; Lichtenhan, J. D. *Sampe Journal* **1997**, *33*, 40-46.

(3) Cudzilo, S.; Kicinski, W. *Propellants Explosives Pyrotechnics* **2009**, *34*, 155-160.

(4) Novak, B. M. *Advanced Materials* **1993**, *5*, 422-433.

(5) Sumfleth, J.; Adroher, X. C.; Schulte, K. *Journal of Materials Science* **2009**, *44*, 3241-3247.

(6) Ogoshi, T.; Chujo, Y. *Macromolecules* **2003**, *36*, 654-660.

(7) Donaldson, K.; Aitken, R.; Tran, L.; Stone, V.; Duffin, R.; Forrest, G.; Alexander, A. *Toxicological Sciences* **2006**, *92*, 5-22.

(8) Holder, E.; Tessler, N.; Rogach, A. L. *Journal of Materials Chemistry* **2008**, *18*, 1064-1078.

(9) Mao, Y. B.; Park, T. J.; Wong, S. S. *Chemical Communications* **2005**, 5721-5735.

(10) Kojima, Y.; Usuki, A.; Kawasumi, M.; Okada, A.; Fukushima, Y.; Kurauchi, T.; Kamigaito, O. *Journal of Materials Research* **1993**, *8*, 1185-1189.

(11) Giannelis, E. P.; Krishnamoorti, R.; Manias, E. In *Polymers in Confined Environments* 1999; Vol. 138, p 107-147.

(12) Giannelis, E. P.; Zhu, J.; Park, B.; Seo, K. H.; (USA). Application: US US, 2005, p 4 pp.

(13) Lu, J. X.; Wong, C. P. *Ieee Transactions on Dielectrics and Electrical Insulation* **2008**, *15*, 1322-1328.

(14) Ravirajan, P.; Peiro, A. M.; Nazeeruddin, M. K.; Graetzel, M.; Bradley, D. D. C.; Durrant, J. R.; Nelson, J. *Journal of Physical Chemistry B* **2006**, *110*, 7635-7639.

(15) Bokobza, L.; Wiley-V C H Verlag Gmbh: 2001, p 243-260.

(16) Bokobza, L.; Rapoport, O. *Journal of Applied Polymer Science* **2002**, *85*, 2301-2316.

(17) *Siloxane Polymers*; Clarson, S. J.; Semylen, J. A., Eds.; Prentice Hall: New Jersey, 1993.

(18) Thomas, D. K.; Moore, B. B. *Polymer* **1972**, *13*, 109-&.

(19) Tarno, L. J.; Dow Corning Corp.: U. S., 1968.

(20) Burnside, S. D.; Giannelis, E. P. *Chemistry of Materials* **1995**, *7*, 1597-1600.

(21) Garrido, L.; Mark, J. E.; Sun, C. C.; Ackerman, J. L.; Chang, C. *Macromolecules* **1991**, *24*, 4067-4072.

(22) Stevenson, I.; David, L.; Gauthier, C.; Arambourg, L.; Davenas, J.; Vigier, G. *Polymer* **2001**, *42*, 9287-9292.

(23) Winberg, P.; Eldrup, M.; Maurer, F. H. J. *Polymer* **2004**, *45*, 8253-8264.

(24) Wen, J.; Mark, J. E. *Journal of Materials Science* **1994**, *29*, 499-503.

(25) Mark, J. E. *Current Opinion in Solid State & Materials Science* **1999**, *4*, 565-570.

(26) Sun, C. C.; Mark, J. E. *Polymer* **1989**, *30*, 104-106.

(27) Warrick, E. L.; Pierce, O. R.; Polmanteer, K. E.; Saam, J. C. *Rubber Chemistry and Technology* **1979**, *52*, 437-525.

(28) Okamoto, T.; Nakamura, S.; Inst Pure Applied Physics: 2008, p 521-526.

(29) Hillborg, H.; Gedde, U. W. *Ieee Transactions on Dielectrics and Electrical Insulation* **1999**, *6*, 703-717.

(30) Unger, M. A.; Chou, H. P.; Thorsen, T.; Scherer, A.; Quake, S. R. *Science* **2000**, *288*, 113-116.

(31) Botter, W.; Soares, R. F.; Galembeck, F. *Journal of Adhesion Science and Technology* **1992**, *6*, 791-805.

(32) Prasad, B. R.; Brook, M. A.; Smith, T.; Zhao, S. G. I.; Chen, Y.; Sheardown, H.; D'Souza, R.; Rochev, Y. *Colloids and Surfaces B-Biointerfaces* **2010**, *78*, 237-242.

(33) Johann, R. M.; Baiotto, C.; Renaud, P. *Biomedical Microdevices* **2007**, *9*, 475-485.

(34) Bullock, S.; Johnston, E. E.; Willson, T.; Gatenholm, P.; Wynne, K. J. *Journal of Colloid and Interface Science* **1999**, *210*, 18-36.

(35) Berglin, M.; Wynne, K. J.; Gatenholm, P. *Journal of Colloid and Interface Science* **2003**, *257*, 383-391.

(36) Cihlar, J. *Colloids and Surfaces a-Physicochemical and Engineering Aspects* **1993**, *70*, 253-268.

(37) Wynne, K. J.; Ho, T.; Johnston, E. E.; Myers, S. A. *Applied Organometallic Chemistry* **1998**, *12*, 763-770.

(38) Inagi, S.; Ogoshi, T.; Miyake, J.; Bertolucci, M.; Fujiwara, T.; Galli, G.; Chiellini, E.; Chujo, Y.; Wynne, K. J. *Chemistry of Materials* **2007**, *19*, 2141-2143.

(39) Ogoshi, T.; Fujiwara, T.; Bertolucci, M.; Galli, G.; Chiellini, E.; Chujo, Y.; Wynne, K. J. *Journal of the American Chemical Society* **2004**, *126*, 12284-12285.

(40) Magonov, S. N.; Elings, V.; Whangbo, M. H. *Surface Science* **1997**, *375*, L385-L391.

(41) Johnston, E.; Bullock, S.; Uilk, J.; Gatenholm, P.; Wynne, K. J. *Macromolecules* **1999**, *32*, 8173-8182.

(42) Garrett, J. T.; Siedlecki, C. A.; Runt, J. *Macromolecules* **2001**, *34*, 7066-7070.

(43) Makal, U.; Fujiwara, T.; Cooke, R. S.; Wynne, K. J. *Langmuir* **2005**, *21*, 10749 -10755.

(44) Agnihotri, A.; Garrett, J. T.; Runt, J.; Siedlecki, C. A. *Journal of Biomaterials Science-Polymer Edition* **2006**, *17*, 227-238.

(45) Kurt, P.; Wood, L.; Ohman, D. E.; Wynne, K. J. *Langmuir* **2007**, *23*, 4719-4723.

(46) Garcia, R.; San Paulo, A. *Physical Review B* **1999**, *60*, 4961-4967.

(47) Stark, R. W.; Schitter, G.; Stemmer, A. *Physical Review B* **2003**, *68*.

(48) Round, A. N.; Miles, M. J. *Nanotechnology* **2004**, *15*, S176-S183.

(49) Uilk, J. M.; Mera, A. E.; Fox, R. B.; Wynne, K. J. *Macromolecules* **2003**, *36*, 3689-3694.

(50) Zhang, W.; Zheng, Y.; Orsini, L.; Morelli, A.; Galli, G.; Chiellini, E.; Carpenter, E. E.; Wynne, K. J. *Langmuir* **2010**, *26*, 5848-5855.

(51) Chanda, M. *Advanced Polymer Chemistry*; Marcel Dekker: New York, 2000.

(52) Opris, D. M.; Molberg, M.; Walder, C.; Ko, Y. S.; Fischer, B.; Nueesch, F. A. *Advanced Functional Materials* **2011**, *21*, 3531-3539.

(53) Thanawala, S. K.; Chaudhury, M. K. *Langmuir* **2000**, *16*, 1256-1260.

(54) Wynne, K. J.; Lambert, J. M. In *Encyclopedia of Biomaterials and Biomedical Engineering*; Wnek, G. W., Bowlin, G. B., Eds.; Marcel Dekker: New York, 2004; Vol. 1, p 1348-1362.

(55) Yilgor, I.; Eynur, T.; Bilgin, S.; Yilgor, E.; Wilkes, G. L. *Polymer* **2011**, *52*, 266-274.

(56) Yilgor, E.; Isik, M.; Yilgor, I. *Macromolecules* **2010**, *43*, 8588-8593.

(57) Yilgor, I.; Eynur, T.; Yilgor, E.; Wilkes, G. L. *Polymer* **2009**, *50*, 4432-4437.

(58) Yilgor, E.; Eynur, T.; Kosak, C.; Bilgin, S.; Yilgor, I.; Malay, O.; Menceloglu, Y.; Wilkes, G. L. *Polymer* **2011**, *52*, 4189-4198.

(59) Owen, M. J. *Ind. Eng. Chem. Prod. Res. Dev.* **1980**, *19*, 97-103.

(60) Kobayashi, H.; Owen, M. J. *Trends in Polymer Science* **1995**, *3*, 330-335.

(61) Furukawa, Y.; Shin-ya, S.; Saito, M.; Narui, S.; Miyake, H. *Polymers for Advanced Technologies* **2002**, *13*, 60-65.

(62) Razzano, J. S.; Momentive Performance Materials Inc.: U. S. Patent 7361722, 2008.

(63) Koshar, R. J.; Minnesota Mining and Manufacturing Company, St. Paul, Minn.: U.S., 1986.

(64) Merkel, T. J.; Herlihy, K. P.; Nunes, J.; Orgel, R. M.; Rolland, J. P.; DeSimone, J. M. *Langmuir* **2010**, *26*, 13086-13096.

(65) Bertolucci, M.; Galli, G.; Chiellini, E.; Wynne, K. J. *Macromolecules* **2004**, *37*, 3666 - 3672.

(66) Harada, K.; Koizumi, A.; Saito, N.; Inoue, K.; Yoshinaga, T.; Date, C.; Fujii, S.; Hachiya, N.; Hirosawa, I.; Koda, S.; Kusaka, Y.; Murata, K.; Omae, K.; Shimbo, S.; Takenaka, K.; Takeshita, T.; Todoriki, H.; Wada, Y.; Watanabe, T.; Ikeda, M. *Chemosphere* **2007**, *66*, 293-301.

(67) Guo, J.; Resnick, P.; Efimenko, K.; Genzer, J.; DeSimone, J. M. *Industrial & Engineering Chemistry Research* **2008**, *47*, 502-508.

(68) Zhang, W.; Henke, D.; Presnall, D.; Chakrabarty, S.; Wang, C.; Wynne, K. J. *Macromol. Chem. Phys.* **2012**, DOI: 10.1002/macp.201200053.

(69) Wilhelmy, L. *Ann. Phys. Chem. Leipzig* **1863**, *119*, 177.

(70) Varadaraj, R.; Bock, J.; Valint, P.; Zushma, S.; Brons, N. *Journal of Physical Chemistry* **1991**, *95*, 1679-1681.

(71) Kim, Y. S.; Lee, J. S.; Ji, Q.; McGrath, J. E. *Polymer* **2002**, *43*, 7161-7170.

(72) Yilgor, E.; Yurtsever, E.; Yilgor, I. *Polymer* **2002**, *43*, 6561-6568.

(73) Ong, M. D.; Volksen, W.; Dubois, G.; Lee, V.; Brock, P. J.; Deline, V. R.; Miller, R. D.; Dauskardt, R. H. *Advanced Materials* **2008**, *20*, 3159-3164.

(74) Volksen, W.; Magbitang, T. P.; Miller, R. D.; Purushothaman, S.; Cohen, S. A.; Nakagawa, H.; Nobe, Y.; Kokubo, T.; Dubois, G. J. M. *Journal of the Electrochemical Society* **2011**, *158*, G155-G161.

(75) Volksen, W.; Miller, R. D.; Dubois, G. *Chemical Reviews* **2010**, *110*, 56-110.

(76) Saegusa, T.; Chujo, Y. *Journal of Macromolecular Science-Chemistry* **1990**, *A27*, 1603-1612.

(77) Chujo, Y.; Ihara, E.; Kure, S.; Saegusa, T. *Macromolecules* **1993**, *26*, 5681-5686.

(78) Uilk, J.; Bullock, S.; Johnston, E.; Myers, S. A.; Merwin, L. H.; Wynne, K. J. *Macromolecules* **2000**, *33*, 8791-8801.

(79) Burgmann, S.; Grosse, S.; Schroder, W.; Roggenkamp, J.; Jansen, S.; Graf, F.; Busen, M. *Experiments in Fluids* **2009**, *47*, 865-881.

(80) Smith, B. C. In *Fundamentals of Fourier transform infrared spectroscopy*; Taylor and Francis group, LLC: Boca Raton, FL, 2009, p 132-134.

(81) Sato, Y.; Ootsubo, M.; Yamamoto, G.; Van Lier, G.; Terrones, M.; Hashiguchi, S.; Kimura, H.; Okubo, A.; Motomiya, K.; Jeyadevan, B.; Hashida, T.; Tohji, K. *Acs Nano* **2008**, *2*, 348-356.

(82) Shimomura, M.; Okumoto, H.; Kaito, A.; Ueno, K.; Shen, J. S.; Ito, K. *Macromolecules* **1998**, *31*, 7483-7487.

(83) Seymour, R. W.; Estes, G. M.; Cooper, S. L. *Macromolecules* **1970**, *3*, 579-583.

(84) Coleman, M. M.; Lee, K. H.; Skrovanek, D. J.; Painter, P. C. *Macromolecules* **1986**, *19*, 2149-2157.

(85) Coleman, M. M.; Skrovanek, D. J.; Hu, J. B.; Painter, P. C. *Macromolecules* **1988**, *21*, 59-65.

(86) MarcosFernandez, A.; Lozano, A. E.; Gonzalez, L.; Rodriguez, A. *Macromolecules* **1997**, *30*, 3584-3592.

(87) Sheth, J. P.; Aneja, A.; Wilkes, G. L.; Yilgor, E.; Atilla, G. E.; Yilgor, I.; Beyer, F. L. *Polymer* **2004**, *45*, 6919-6932.

(88) Tyagi, D.; Yilgor, I.; McGrath, J. E.; Wilkes, G. L. *Polymer* **1984**, *25*, 1807-1816.

(89) Uemura, S.; Takayanagi, M. *Journal of Applied Polymer Science* **1966**, *10*, 113-125.

(90) Sperling, L. H. *Introduction to Physical Polymer Science*; 4th ed.; Wiley Interscience: Hoboken, NJ, 2006.

(91) Feng, H. Q.; Feng, Z. L.; Yuan, H. Z.; Shen, L. F. *Macromolecules* **1994**, *27*, 7830-7834.

(92) Chen, Z.; Gong, K. *Journal of Applied Polymer Science* **2002**, *84*, 1499-1503.

(93) Wang, L. F.; Ji, Q.; Glass, T. E.; Ward, T. C.; McGrath, J. E.; Muggli, M.; Burns, G.; Sorathia, U. *Polymer* **2000**, *41*, 5083-5093.

(94) Sperling, L. H. In *Applied Polymer Science*; Craver, C., Carraher, C. J., Eds.; Elsevier Science: New York, 2000, p 343-354.

(95) Liu, R. Y. F.; Jin, Y.; Hiltner, A.; Baer, E. *Macromolecular Rapid Communications* **2003**, *24*, 943-948.

(96) Liu, R. Y. F.; Ranade, A. P.; Wang, H. P.; Bernal-Lara, T. E.; Hiltner, A.; Baer, E. *Macromolecules* **2005**, *38*, 10721-10727.

(97) Lai, C.; Ayyer, R.; Hiltner, A.; Baer, E. *Polymer* **2010**, *51*, 1820-1829.

(98) Hu, Z. K.; Chen, L.; Betts, D. E.; Pandya, A.; Hillmyer, M. A.; DeSimone, J. M. *Journal of the American Chemical Society* **2008**, *130*, 14244-14252.

(99) Zhang, W.; Fujiwara, T.; Taskent, H.; Zheng, Y.; Brunson, K.; Gamble, L.; Wynne, K. J. *Macromol. Chem. Phys.* **2012**, in press.

(100) Makal, U.; Uilk, J.; Kurt, P.; Cooke, R. S.; Wynne, K. J. *Polymer* **2005**, *46*, 2522-2530.

(101) Yebra, D. M.; Kiil, S.; Dam-Johansen, K. *Progress in Organic Coatings* **2004**, *50*, 75-104.

(102) Stafslien, S.; Daniels, J.; Mayo, B.; Christianson, D.; Chisholm, B.; Ekin, A.; Webster, D.; Swain, G. *Biofouling* **2007**, *23*, 45-54.

(103) Townsin, R. L. *Biofouling* **2003**, *19*, 9-15.

(104) Brady, R. F. *Progress in Organic Coatings* **1999**, *35*, 31-35.

(105) Rascio, V. J. D. *Corrosion Reviews* **2000**, *18*, 133-154.

(106) Abbott, A.; Abel, P. D.; Arnold, D. W.; Milne, A. *Science of the Total Environment* **2000**, *258*, 5-19.

(107) Cooney, J. J.; Tang, R. J. *Biofilms* **1999**, *310*, 637-644.

(108) Reise, K.; Gollasch, S.; Wolff, W. J. *Helgolaender Meeresuntersuchungen* **1998**, *52*, 219-234.

(109) Alzieu, C. *Ecotoxicology* **2000**, *9*, 71-76.

(110) Katranitsas, A.; Castritsi-Catharios, J.; Persoone, G. *Marine Pollution Bulletin* **2003**, *46*, 1491-1494.

(111) Cleary, J. J.; Stebbing, A. R. D. *Marine Pollution Bulletin* **1985**, *16*, 350-355.

(112) Champ, M. A. *Science of the Total Environment* **2000**, *258*, 21-71.

(113) Kannan, K.; Senthilkumar, K.; Loganathan, B. G.; Takahashi, S.; Odell, D. K.; Tanabe, S. *Environmental Science & Technology* **1997**, *31*, 296-301.

(114) Milne, A.; USPTO, Ed.; The International Paint Co., Ltd. (London, EN): US, 1977.

(115) Baier, R. E.; Shafrin, E. G.; Zisman, W. A. *Science* **1968**, *162*, 1360-&.

(116) Finlay, J. A.; Callow, M. E.; Ista, L. K.; Lopez, G. P.; Callow, J. A. *Integrative and Comparative Biology* **2002**, *42*, 1116-1122.

(117) Brady, R. F.; Singer, I. L. *Biofouling* **2000**, *15*, 73-81.

(118) Singer, I. L.; Kohl, J. G.; Patterson, M. *Biofouling* **2000**, *16*, 301-309.

(119) Newby, B. M. Z.; Chaudhury, M. K.; Brown, H. R. *Science* **1995**, *269*, 1407-1409.

(120) Kohl, J. G.; Singer, I. L. *Progress in Organic Coatings* **1999**, *36*, 15-20.

(121) Thomas, J.; Choi, S. B.; Fjeldheim, R.; Boudjouk, P. *Biofouling* **2004**, *20*, 227-236.

(122) Schmidt, D. L.; Coburn, C. E.; Dekoven, B. M.; Potter, G. E.; Meyers, G. F.; Fischer, D. A. *Nature* **1994**, *368*, 39-41.

(123) Kendall, K. *J. Physics D Applied Physics* **1971**, *4*, 1186-1195.

(124) Ghatak, A.; Mahadevan, L.; Chaudhury, M. K. *Langmuir* **2005**, *21*, 1277-1281.

(125) Ghatak, A.; Chaudhury, M. K.; Shenoy, V.; Sharma, A. *Physical Review Letters* **2000**, *85*, 4329-4332.

(126) Yang, F. Q.; Li, J. C. M. *Langmuir* **2001**, *17*, 6524-6529.

(127) Creton, C.; Lakrout, H. *Journal of Polymer Science Part B-Polymer Physics* **2000**, *38*, 965-979.

(128) Crosby, A. J.; Shull, K. R.; Lakrout, H.; Creton, C. *Journal of Applied Physics* **2000**, *88*, 2956-2966.

(129) Ghatak, A.; Mahadevan, L.; Chung, J. Y.; Chaudhury, M. K.; Shenoy, V. *Proceedings of the Royal Society of London Series a-Mathematical Physical and Engineering Sciences* **2004**, *460*, 2725-2735.

(130) Webber, R. E.; Shull, K. R.; Roos, A.; Creton, C. *Physical Review E* **2003**, *68*, 11.

(131) Chaudhury, M. K.; Kim, K. H. *European Physical Journal E* **2007**, *23*, 175-183.

(132) Wynne, K. J.; Swain, G. W.; Fox, R. B.; Bullock, S.; Uilk, J. *Biofouling* **2000**, *16*, 277-288.

(133) Park, D.; Weinman, C. J.; Finlay, J. A.; Fletcher, B. R.; Paik, M. Y.; Sundaram, H. S.; Dimitriou, M. D.; Sohn, K. E.; Callow, M. E.; Callow, J. A.; Handlin, D. L.; Willis, C. L.; Fischer, D. A.; Kramer, E. J.; Ober, C. K. *Langmuir* **2010**, *26*, 9772-9781.

(134) Swain, G. *J. Protective Coatings and Linings* **1999**, *16*, 26-33.

(135) Swain, G. W.; Schultz, M. P. *Biofouling* **1996**, *10*, 187-197.

(136) Darrigran, G.; Damborenea, C.; Greco, N. *Ambio* **2007**, *36*, 575-579.

(137) Aldridge, D. C.; Salazar, M.; Serna, A.; Cock, J. *Aquaculture* **2008**, *281*, 34-42.

(138) Evans, S. M.; Leksono, T.; McKinnell, P. D. *Marine Pollution Bulletin* **1995**, *30*, 14-21

(139) Finnie, A.; Williams, D. N. In *Biofouling*; Durr, S., Thomason, J. C., Eds.; Wiley-Blackwell: Chichester, U.K, 2010, p 185-201.

(140) Wu, S. C.; Lee, C. M. *Bioresource Technology* **2011**, *102*, 5375-5380.

(141) Le-Clech, P. *Applied Microbiology and Biotechnology* **2010**, *88*, 1253-1260.

(142) *Biofouling*; Durr, S.; Thomason, J. C., Eds.; Wiley-Blackwell: Chinchester, UK, 2010.

(143) Tribou, M.; Swain, G. *Biofouling* **2010**, *26*, 47-56.

(144) Kumar, A.; Gupta, R. K. *Fundamentals of Polymer Engineering*; Marcel Dekker: New York, 2003.

(145) Tsibouklis, J.; Stone, M.; Thorpe, A. A.; Graham, P.; Peters, V.; Heerlien, R.; Smith, J. R.; Green, K. L.; Nevell, T. G. *Biomaterials* **1999**, *20*, 1229-1235.

(146) Thorpe, A. A.; Peters, V.; Smith, J. R.; Nevell, T. G.; Tsibouklis, J. *Journal of Fluorine Chemistry* **2000**, *104*, 37-45.

(147) Williams, D. N.; Lines, R.; International Coatings, Ltd., Ausimont SpA: 2001; Vol. A1287056B1.

(148) Evans, E. R.; General Electric Company, Waterford, N.Y.: US Patent Appl 4,997,289, 1990.

(149) Evans, E. R.; General Electric Company, Waterford, N.Y.: US Patent Appl 5,079,291, 1992.

(150) Gosh, N. E.; Razzano, J. S.; Wand, A.; Momentive Performance Materials Inc., Albany, NY: US Patent Appl 7,671,161 B2, 2010.

(151) Yarbrough, J. C.; Rolland, J. P.; DeSimone, J. M.; Callow, M. E.; Finlay, J. A.; Callow, J. A. *Macromolecules* **2006**, *39*, 2521-2528.

(152) Adachi, K.; Achimuthu, A. K.; Chujo, Y. *Macromolecules* **2004**, *37*, 9793-9797.

(153) Kurt, P.; Wynne, K. J. *Macromolecules* **2007**, *40*, 9537-9543.

(154) Shin, J.; Matsushima, H.; Chan, J. W.; Hoyle, C. E. *Macromolecules* **2009**, *42*, 3294-3301.

(155) Fujiwara, T.; Wynne, K. J. *Macromolecules* **2004**, *37*, 8491-8494.

(156) Ewart, T.; Tarnopolsky, M.; Baker, S.; Raha, S.; Wong, Y.-Y.; Ciebiera, K. *Proc. SPIE* **2009**, *7380*, 73806E/1-73806E/12.

(157) Spelman, D. W. *Medical Journal of Australia* **2002**, *176*, 286-291.

(158) Klevens, R. M.; Edwards, J. R.; Richards, C. L.; Horan, T. C.; Gaynes, R. P.; Pollock, D. A.; Cardo, D. M. *Public Health Reports* **2007**, *122*, 160-166.

(159) Safdar, N.; Maki, D. G. *Intensive Care Medicine* **2004**, *30*, 62-67.

(160) Schwartz, D. J.; Chen, S. L.; Hultgren, S. J.; Seed, P. C. *Infection and Immunity* **2011**, *79*, 4250-4259.

(161) O'Brien, R.; Pocock, N.; Torella, F. *Surgeon-Journal of the Royal Colleges of Surgeons of Edinburgh and Ireland* **2011**, *9*, 245-248.

(162) Crocker, I. C.; Liu, W. K.; Byrne, P. O.; Elliott, T. S. J. *Journal of Hospital Infection* **1992**, *22*, 7-17.

(163) Cachot, J. T.; Gimenez, J. C. S.; Vecina, S. T.; Basseda, R. M.; Jarque, J. M. G. *Medicina Clinica* **1990**, *95*, 568-571.

(164) Richards, M. J.; Edwards, J. R.; Culver, D. H.; Gaynes, R. P. *Pediatrics* **1999**, *103*, e39.

(165) Dornbusch, K.; Olssonliljequist, B.; Nord, C. E. *Journal of Antimicrobial Chemotherapy* **1980**, *6*, 207-216.

(166) Legakis, N. J.; Kafetzis, D. A.; Papadatos, C. J.; Papavassiliou, J. T. *Chemotherapy* **1980**, *26*, 334-343.

(167) Szydlowska, T. *Zentralblatt Fur Bakteriologie Mikrobiologie Und Hygiene Series a-Medical Microbiology Infectious Diseases Virology Parasitology* **1977**, *239*, 270-274.

(168) Reynolds, A. V.; Hamiltonmiller, J. M. T.; Brumfitt, W. *Journal of Infectious Diseases* **1976**, *134*, S291-S296.

(169) Trinh, T. T.; Chan, P. A.; Edwards, O.; Hollenbeck, B.; Huang, B.; Burdick, N.; Jefferson, J. A.; Mermel, L. A. *Infection Control and Hospital Epidemiology* **2011**, *32*, 579-583.

(170) Mostofsky, E.; Lipsitch, M.; Regev-Yochay, G. *Journal of Antimicrobial Chemotherapy* **2011**, *66*, 2199-2214.

(171) Lehir, M.; Boulottolle, M.; Remiot, B.; Bourlioux, P. *Medecine Et Maladies Infectieuses* **1991**, *21*, 7-11.

(172) Steed, M. E.; Vidaillac, C.; Rose, W. E.; Winterfield, P.; Kaatz, G. W.; Rybak, M. J. *Antimicrobial Agents and Chemotherapy* **2011**, *55*, 4748-4754.

(173) Entenza, J. M.; Veloso, T. R.; Vouillamoz, J.; Giddey, M.; Majcherczyk, P.; Moreillon, P. *Antimicrobial Agents and Chemotherapy* **2011**, *55*, 3977-3984.

(174) Rey-Jurado, E.; Tudo, G.; Borrell, S.; Alcaide, F.; Coll, P.; Espanol, M.; Martin-Casabona, N.; Mick, V.; Montemayor, M.; Moure, R.; Salvado, M.; Vicente, E.; Gonzalez-Martin, J. *Journal of Antimicrobial Chemotherapy* **2011**, *66*, 2277-2280.

(175) Lai, C. C.; Tan, C. K.; Huang, Y. T.; Liao, C. H.; Hsueh, P. R. *Journal of Antimicrobial Chemotherapy* **2011**, *66*, 2437-2438.

(176) Zasloff, M. *Nature* **2002**, *415*, 389-395.

(177) Zasloff, M. *Proc. Natl. Acad. Sci. U. S. A* **1987**, *84*, 5449-53.

(178) Lee, S.; Park, N. G.; Kato, T.; Aoyagi, H.; Kato, T. *Chemistry Letters* **1989**, 599-602.

(179) Mika, J. T.; Moiset, G.; Cirac, A. D.; Feliu, L.; Bardaji, E.; Planas, M.; Sengupta, D.; Marrink, S. J.; Poolman, B. *Biochimica Et Biophysica Acta-Biomembranes* **2011**, *1808*, 2197-2205.

(180) Gesell, J.; Zasloff, M.; Opella, S. J. *Journal of biomolecular NMR* **1997**, *9*, 127-35.

(181) Zasloff, M.; Martin, B.; Chen, H. C. *Proceedings of the National Academy of Sciences of the United States of America* **1988**, *85*, 910-913.

(182) Lohner, K.; Prossnigg, F. *Biochimica Et Biophysica Acta-Biomembranes* **2009**, *1788*, 1656-1666.

(183) Wade, D.; Merrifield, R. B.; Boman, H. G. *Acs Symposium Series* **1991**, *444*, 237-248.

(184) Kawano, K.; Yoneya, T.; Miyata, T.; Yoshikawa, K.; Tokunaga, F.; Terada, Y.; Iwanaga, S. In *Peptide Chemistry 1990*; Protein Research Foundation: Osaka, 1991, p 385-388.

(185) Wu, Z.; Ericksen, B.; Tucker, K.; Lubkowski, J.; Lu, W. *Journal of Peptide Research* **2004**, *64*, 118-125.

(186) Pant, R. R.; Fulmer, P. A.; Harney, M. B.; Buckley, J. P.; Wynne, J. H. *Journal of Applied Polymer Science* **2009**, *113*, 2397-2403.

(187) Hugo, W. B. *Journal of Applied Bacteriology* **1967**, *30*, 17-&.

(188) Bradshaw, J. P. *Biodrugs* **2003**, *17*, 233-240.

(189) Kanazawa, A.; Ikeda, T.; Endo, T. *Kobunshi* **1994**, *43*, 237.

(190) Kawabata, N.; Nishiguchi, M. *Appl Environ Microbiol* **1988**, *54*, 2532-5.

(191) Kenawy, E. R.; Mahmoud, Y. A. G. *Macromolecular Bioscience* **2003**, *3*, 107-116.

(192) Kurt, P.; Gamble, L. J.; Wynne, K. J. *Langmuir* **2008**, *24*, 5816-5824.

(193) Lienkamp, K.; Madkour, A. E.; Kumar, K.-N.; Nuesslein, K.; Tew, G. N. *Chem. Eur. J.* **2009**, *15*, 11715-11722.

(194) Tiller, J. C.; Lee, S. B.; Lewis, K.; Klibanov, A. M. *Biotechnology and Bioengineering* **2002**, *79*, 465-471.

(195) Grapski, J. A.; Cooper, S. L. *Biomaterials* **2001**, *22*, 2239-2246.

(196) Kanazawa, A.; Ikeda, T.; Endo, T. *Antimicrob. Agents Ch.*. **1994**, *38*, 945-952.

(197) Greco, R. S.; Trooskin, S. Z.; Donetz, A. P.; Harvey, R. A. *Archives of Surgery* **1985**, *120*, 71-75.

(198) Harvey, R. A.; Alcid, D. V.; Greco, R. S. *Surgery* **1982**, *92*, 504-512.

(199) Harvey, R. A.; Tesoriero, J. V.; Greco, R. S. *American Journal of Surgery* **1984**, *147*, 205-209.

(200) Isquith, A. J.; Abbott, E. A.; Walters, P. A. *Applied Microbiology* **1972**, *24*, 859-863.

(201) Wong, S. Y.; Li, Q.; Veselinovic, J.; Kim, B. S.; Klibanov, A. M.; Hammond, P. T. *Biomaterials*, *31*, 4079-4087.

(202) Sauvet, G.; Dupond, S.; Kazmierski, K.; Chojnowski, J. *Journal of Applied Polymer Science* **2000**, *75*, 1005-1012.

(203) Walters, P. A.; Abbott, E. A.; Isquith, A. J. *Applied Microbiology* **1973**, *25*, 253-256.

(204) Gupta, M. L.; Brunson, K.; Chakravorty, A.; Kurt, P.; Alvarez, J. C.; Luna-Vera, F.; Wynne, K. J. *Langmuir* **2010**, *26*, 9032-9039.

(205) Moglianetti, M.; Campbell, R. A.; Nylander, T.; Varga, I.; Mohanty, B.; Claesson, P. M.; Makuska, R.; Titmuss, S. *Soft Matter* **2009**, *5*, 3646-3656.

(206) Xie, H.; Saito, T.; Hickner, M. A. *Langmuir* **2011**, *27*, 4721-4727.

(207) Cohen, R. R.; Radke, C. J. *Journal of Colloid and Interface Science* **1991**, *141*, 338-347.

(208) Makal, U.; Wood, L.; Ohman, D. E.; Wynne, K. J. *Biomaterials* **2006**, *27*, 1316-1326.

(209) Isquith, A. J.; McCollum, C. J. *Applied and Environmental Microbiology* **1978**, *36*, 700-704.

(210) Fuji, M.; Ueno, S.; Takei, T.; Watanabe, T.; Chikazawa, M. *Colloid and Polymer Science* **2000**, *278*, 30-36.

(211) Fuji, M.; Takei, T.; Watanabe, T.; Chikazawa, M. *Colloids and Surfaces a-Physicochemical and Engineering Aspects* **1999**, *154*, 13-24.

(212) Arce, V. B.; Bertolotti, S. G.; Oliveira, F. J. V. E.; Airoldi, C.; Arques, A.; Santos-Juanes, L.; Gonzales, M. C.; Cobos, C. J.; Allegretti, P. E.; Martire, D. O. *Photochem. Photobiol. Sci.* **2012**, *11*, 1032-1040.

(213) Slavov, S. V.; Sanger, A. R.; Chuang, K. T. *Journal of Physical Chemistry B* **2000**, *104*, 983-989.

(214) Lee, M. W.; Hu, X.; Yue, C. Y.; Li, L.; Tam, K. C. *Composites Science and Technology* **2003**, *63*, 339-346.

(215) Mata, A.; Kim, E. J.; Boehm, C. A.; Fleischman, A. J.; Muschler, G. F.; Roy, S. *Biomaterials* **2009**, *30*, 4610-4617.

(216) Wipff, P. J.; Majd, H.; Acharya, C.; Buscemi, L.; Meister, J. J.; Hinz, B. *Biomaterials* **2009**, *30*, 1781-1789.

(217) Saha, K.; Keung, A. J.; Irwin, E. F.; Li, Y.; Little, L.; Schaffer, D. V.; Healy, K. E. *Biophysical Journal* **2008**, *95*, 4426-4438.

(218) Kelly, D. J.; Prendergast, P. J. *Journal of Biomechanics* **2005**, *38*, 1413-1422.

VITA

Souvik Chakrabarty was born on May 18, 1985 in West Bengal, India. He graduated from the Assembly of God Church School (Kolkata), India, in 2003. He received his Bachelor of Science in Chemical Engineering (Honors) from Jadavpur University, India in 2007.

Publications

1. **Chakrabarty S**, King A , Kurt P , Zhang W, Ohman DE, Wood LF, Lovelace C, Rao R and Wynne KJ. "Highly Effective, Water Soluble, Hemocompatible 1,3-Propylene Oxide-Based Antimicrobials: Poly[(3,3-Quaternary/PEG)-Copolyoxetanes]". *Biomacromolecules* **2011** 12(3) 757-69.
2. **Chakrabarty S**, Zhang XJ, Bharti P, Chujo Y, Miyake J, Wynne KJ, Yadavalli VK. "Processing dependence of surface morphology in condensation cured PDMS nanocomposites". *POLYMER* **2010** 51(24) 5756-5763.
3. Zhang W., Henke D., Presnall D., **Chakrabarty S**., Wang C and Wynne KJ. "Liquid-Liquid Extraction of 3FOx and 5FOx Polyoxetane Diols: Impact on Polyurethane Mechanical Properties, Surface Morphology and Wetting Behavior" *Accepted in Macromolecular Chemistry and Physics.*

To be submitted

1. **Chakrabarty S**, Zhang W, Wynne KJ. "Abhesive Coatings: Hybrids of Siliceous Networks and a Linear Polyurethane, both employing a Poly(3-trifluoroethoxy-methyl-3-methyl-oxetane) Soft Block".

2. **Chakrabarty S.** and Wynne KJ. "Condensation Cured Polydimethylsiloxane-Fluorous Polyoxetane Triblock Copolymers: Tough, Transparent, Phase Separated Elastomers".
3. **Chakrabarty S.,** Zhang W. and Wynne KJ. "Condensation cured triblock copolymers as effective *foul-release* coatings."
4. King A, **Chakrabarty S**, Ohman DE, Wood LF, Abraham S, Rao R and Wynne KJ. "PEG/quaternary copolyoxetanes: antimicrobial effectiveness, hemolytic and cytotoxic activity in response to alkyl side chain length".

Patent applications

1. Wynne KJ, **Chakrabarty S.** "Antimicrobial Silicone". Provisional patent application, October 2011.
2. Wynne KJ, Kurt P, **Chakrabarty S**, King A, Ohman DE, Rao R. "Antimicrobial Copolyoxetanes". Provisional patent application, August 2010.
3. **Chakrabarty S**, Zhang W, Wynne KJ. "Abhesive Coatings: Hybrids of Siliceous Networks and a Linear Polyurethane, both employing a Poly(3-trifluoroethoxy-methyl-3-methyl-oxetane) Soft Block.'. Provisional patent application, July 2011.

Conference proceedings/preprints/posters

1. **Chakrabarty S**, Wynne KJ. "Hybrid Compositions via Fluorous Soft Blocks". 63rd SERMACS, Richmond, VA. Oct 26-29, 2011.
2. **Chakrabarty S**, Wynne KJ. "Strange Soft Surfaces via Fluorous Copolyoxetane Soft Blocks". 242nd ACS National Meeting and Exposition, Denver, CO. Aug 26-Sept 2, 2011.

3. Kurt P, **Chakrabarty S**, King A, Ohman DE, Wood LF, Wynne KJ. "P[AB] Copolyoxetanes : A Novel Class of Biocide". 240th ACS National Meeting and Exposition, Boston, MA. Aug 22-26, 2010.
4. **Chakrabarty S**, Bharti P, Zhang XJ, Yadavalli VK, Wynne KJ. "Surface Characterization of Silicone Nanocomposites with Varying Processing Conditions". Poster Presentation, *Nanohybrids 2009 - Future trends in Organic/Inorganic hybrid nanocomposites materials*, Himeji, Japan.

Honors and Awards

1. Received a prestigious Graduate Travel Award for poster presentation at - 'Nanohybrids 2009 – Future trends in Organic/Inorganic hybrid nanocomposites materials' at Himeji, Japan.
2. Member of The Honor Society of 'Phi Kappa Phi' 2009-present.
3. Member of the Golden Key Honor Society 2009-present.
4. Awarded with Graduate student scholarship from the School of Engineering, VCU by PhiKappaPhi in 2010.
5. Awarded with the VCU Graduate School Thesis Dissertation Assistantship 2011-12.